# Scaleup of Electrochemical-Metal-Refining Process

by

Prashant Soral

B.Tech., Indian Institute of Technology, Bombay (1995)

Submitted to the Department of Materials Science and Engineering
in partial fulfillment of the requirements for the degree of

Master of Science in Materials Science and Engineering

at the

MASSACHUSETTS INSTITUTE OF TECHNOLOGY

February 1998



Author .....
Department of Materials Science and Engineering
January 16, 1998

Certified by .....
Uday B. Pal
John Chipman Associate Professor of Chemical Processing of Materials
Thesis Supervisor

Accepted by .....
Linn W. Hobbs
John F. Elliot Professor of Materials
Chairman, Departmental Committee on Graduate Students

# Scaleup of Electrochemical-Metal-Refining Process

by

Prashant Soral

Submitted to the Department of Materials Science and Engineering
on January 16, 1998, in partial fulfillment of the
requirements for the degree of
Master of Science in Materials Science and Engineering

## Abstract

Laboratory-scale galvanic deoxidation technology developed by earlier workers has been investigated with the aim of developing a prototype pilot-scale deoxidation unit. An order of magnitude enhancement in the deoxidation-process kinetics has been attained. Each deoxidation cell consists of a one-end closed yttria-stabilized zirconia (YSZ) tube coated with Ni-YSZ cermet on the inner walls. The YSZ tube is immersed in the melt and an oxygen chemical-potential gradient across the YSZ electrolyte is used to deoxidize the melt by short-circuiting it with the cermet.

Through laboratory experimentation, the nature of anode/electrolyte interface adhesion was identified to be an important factor in obtaining enhanced deoxidation kinetics. The kinetics of oxygen removal from the melt was increased by developing a slurry-coating process that was used to fabricate porous, electronically conducting and adherent cermet layers. The deoxidation process model was modified to include multiple deoxidation cells, that were required for pilot-scale trials, and to analyze the effect of electrolyte/electrode adhesion on deoxidation kinetics.

A pilot-scale refining unit consisting of 53 cells was manufactured and field evaluation of galvanic deoxidation of copper was conducted at Reading Tube Corporation/Cambridge Lee Industries, Reading, PA. Based on the results of the field trial, efforts have been devoted towards the development of large-scale anode-supported deoxidation structures for industrial implementation. Finally, process-component lifetimes have been studied by investigating the thermal cycling, corrosion behavior of the electrolyte and long-term stability of the porous cermet structure.

Thesis Supervisor: Uday B. Pal
Title: John Chipman Associate Professor of Chemical Processing of Materials

# Acknowledgements

Above all, I would like to thank my parents, Aditya and Nisha Soral, for the constant support and encouragement they have provided in all my endeavors. Achieving my goals would have been impossible without their help.

I would like to express my sincere gratitude towards my advisor, Prof. Uday B. Pal, for the direction and guidance he has provided during my years at MIT.

I take this opportunity to thank Dr. Harold R. Larson, not only for all the help he has provided during the course of this research, but also for the practical advice I have received from him. I also acknowledge Prof. Alex McLean's valuable input during my thesis presentation.

I would like to express my appreciation towards Brad Schroeder of Reading Tube Corporation/Cambridge Lee Industries, without whose support, experimentation at Reading would not have been possible. Ronald Mizia of Lockheed Martin Idaho Technologies was extremely helpful in coordinating the research efforts at MIT and Reading Tube. He has taken keen interest in advancing the project towards commercial implementation.

I am thankful to my officemates, David Woolley, Stephen Britten, Ashish Agarwal, and Dr. Sridhar Seetharaman for making my stay at MIT all the more exciting and enjoyable. Special thanks are due to David for helping me through my Doctoral General Exam.

Finally, I would like to acknowledge the financial support received from the University Research Consortium of the Idaho National Engineering and Environmental Laboratory.

# Contents

# List of Figures

# List of Tables

# Chapter 1

# Introduction

Control of undesirable elements, such as dissolved hydrogen, sulfur and oxygen, in liquid metals and alloys is critical to obtaining superior physical and mechanical properties of the final product. Over the past few decades, this has resulted in a search for new metal-refining techniques capable of reducing the concentration of impurities to extremely low levels. Currently, the two most popular refining techniques are vacuum degassing and addition of reagents to form stable compounds with the undesirable elements[1]. Vacuum degassing is capital intensive, limited by the vacuum pressure that can be created over the melt, and can lead to the loss of desirable elements. In the case of chemical refining, some of the reagent metals can be expensive, and the compounds of the undesirable elements may remain as inclusions in the metal. In addition, the reagent may go into solution in the melt, which may deteriorate the properties. There exists a need for a commercially-viable, energy efficient, and environmentally sound molten-metal refining technique which overcomes the above-mentioned disadvantages.

Since the pioneering work of Kiukolla and Wagner[2] on solid-oxide electrolytes, stabilized zirconia has received attention with regard to its application in both thermodynamic and kinetic studies of high-temperature metallurgical systems[3]. A large number of workers have demonstrated the feasibility of using oxygen-ion conduction in stabilized zirconia to extract oxygen from molten metals[1, 3, 4, 5, 6, 7, 8]. Electrochemical deoxidation of molten metals involves the diffusion of oxygen through the solid-oxide electrolyte (stabilized zirco-

nia) out of the melt and can be divided into two categories: galvanic and electrolytic. In the electrolytic process, an external potential is used to pump oxygen through the electrolyte. In the galvanic process, the electrolyte is used to separate the oxygen-containing melt from a reducing atmosphere and the oxygen-chemical-potential gradient acts as the driving force for the migration of oxygen ions across the zirconia membrane[9].

Due to application of an external potential, the electrolytic process would rely on the combustion of fossil fuels to produce electrical energy and therefore have an intrinsic efficiency limitation imposed by the Carnot cycle[10]. In addition, hydrocarbons, $NO_x/SO_x$ gases, and carbon monoxide, released into the atmosphere during incomplete combustion of fossil fuels, are thought to adversely affect both public health and the environment. On the other hand, the galvanic technique operates on the same principle as a fuel cell (an energy conversion device that produces electricity and heat by electrochemical combination of a fuel and an oxidant). Because a fuel cell converts the chemical energy of the fuel directly to electrical energy (and heat), its efficiency is not subject to the Carnot limitation[11], making the galvanic technique more energy efficient than electrolytic deoxidation.

Yuan et. al. [8] and Hasham et. al. [1] have developed a novel solid-state refining device, based on the galvanic technique, and have utilized the device for deoxidizing molten copper and steel, respectively. Their refining device consists of a one-end-closed yttria-stabilized zirconia (YSZ) tube, which is immersed in a bath of molten metal. An electronically conducting, porous cermet electrode is deposited on the inner walls of the tube and the tube interior is flushed with a reducing gas. The melt is deoxidized by short-circuiting the cermet electrode with the melt. The main advantage of oxygen removal by the electrochemical technique described above, lies in the fact that the deoxidized metals are free of oxide inclusions which are invariably present when the melts are deoxidized by chemical reagents[1, 4]. In addition, the deoxidation technique is environmentally benign as it does not generate any harmful by-products in the form of dust, gas, or slag[1].

Yuan et. al. [8] have conducted a detailed analysis of the galvanic deoxidation process,

and have identified the key factors that need to be considered during designing of an industrial deoxidation system. Based on the model, they have proposed a scale-up structure for the solid-electrolyte cell, that could be used for either a batch or continuous deoxidation process. It consists of a series of stabilized-zirconia plates with stabilized-zirconia plugs that close alternate openings between the plates. The walls of the annular solid-electrolyte structure encapsulated by the plug would be coated with a cermet electrode, that would be exposed to a reducing gas. For deoxidation, the structure would be immersed in the melt, the melt would rise in between the open-ended zirconia plates, and the cermet electrode would be short-circuited with the melt.

The present work was undertaken in order to develop a prototype pilot-scale unit for the electrochemical deoxidation of molten metals. The refining unit was designed on the basis of the scale-up structures proposed by earlier workers[6, 8]. The deoxidation kinetics obtained by using single solid-electrolyte cells that constitute the pilot-scale unit was investigated and improved (an order of magnitude enhancement) by developing a modified cermet fabrication process. Field trials were conducted at a continuous copper casting facility (Reading Tube Corporation - RTC/Cambridge Lee Industries, Reading, PA) to evaluate the performance of the prototype structure. A preliminary investigation of the process component lifetimes at high temperature and of the thermal cycling behavior of the electrolyte has also been conducted. Based on the results of the present study, thermally shock resistant, anode-supported deoxidation cell structures are being developed for industrial implementation.

In order to briefly introduce the technology and present the state-of-the-art, Chapter 2 first provides a survey of earlier studies on electrochemical deoxidation. This is followed by a description of the phenomenology of the process, wherein, the process is analyzed in terms of five elementary steps. A computational process model developed by Yuan et. al. [9] has been discussed next. The chapter also describes the modifications made to the model, in order to include multi-cell structures and the effect of electrolyte/electrode adhesion on process kinetics. Chapter 2 concludes with an analysis of the results obtained on modeling a typical deoxidation experiment conducted by Yuan et. al.

Chapter 3 describes experiments conducted to measure the ionic and electronic conductivity properties of YSZ electrolyte tubes that were used in the present study. Characterization of the conductivity properties is required to model the deoxidation experiments. In Chapter 4, detailed information on the setup and procedure for laboratory-scale deoxidation experiments is provided. Results of preliminary deoxidation experiments that were conducted using the cermet coating technique developed by Chou et. al. [12] have been presented. Based on an analysis of the preliminary experiments, Chapter 4 identifies the need to develop a slurry-coating process to fabricate adherent cermet electrodes.

Chapter 5 starts with a review of studies conducted to investigate the relation between the performance characteristics of a cermet electrode and its fabrication method. An improved slurry coating technique that was developed on the basis of the literature review has been detailed next. Adherent Ni-YSZ cermet electrodes fabricated using the modified technique have been characterized using scanning electron microscopy, energy-dispersive X-ray analysis and mercury porosimetry. Finally, the chapter demonstrates the enhanced deoxidation kinetics obtained in laboratory experiments that were conducted using YSZ tubes coated with the improved cermets.

The deoxidation kinetics obtained with the improved coating technique was found suitable for pilot-scale trials. Chapter 6 provides detailed information on the deoxidation setup used for field trials at RTC and presents results obtained from the field trial. Commercial viability of the process will require extended application of the deoxidation cells at high temperature. The chapter also describes preliminary experiments conducted and the methodology to study process component lifetimes at high temperature.

Finally, the study has been used to direct efforts towards the development of manufacturing processes for deoxidation cell structures suited to industrial implementation.

# Chapter 2

# Electrochemical Deoxidation Employing Solid-Oxide Electrolytes

## 2.1 Literature Review

Korousic et. al. [13] in 1968 were among the first few to demonstrate the feasibility of using oxygen-ion conduction in stabilized zirconia to extract oxygen from molten metals. They immersed a one-end closed magnesia-stabilized zirconia tube (3.5 mm thick) containing molten copper into a copper melt contained in a crucible. Molybdenum rods were inserted into the two copper melts, and an external potential was applied to drive oxygen from the copper melt outside the zirconia tube, to the melt inside. In a typical deoxidation experiment, the oxygen content in the copper melt outside the zirconia tube, as determined by chemical analyses, was reduced from $\approx$70 ppm to $\approx$10 ppm in 25 minutes. The maximum applied potential was 3.22V, for which they obtained a current density of 124 $mA/cm^2$.

Fischer et. al. [4] similarly studied electrolytic deoxidation of liquid Fe, Co, Ni, and Cu melts at 1600°C. A one-end closed, stabilized-zirconia tube was immersed into the melt, and either a noble metal-gas electrode or a liquid-metal with a graphite contact rod was used as the anode. A metal lead wire inserted into the mechanically-stirred metal bath served as

the cathode. 450g of liquid iron and steel, initially containing ≈0.05 wt.% O, were deoxidized down to 0.002-0.003 wt.% O in ≈100 minutes (with a current density of 150 $mA/cm^2$).

Oberg et. al. [5] deoxidized induction-stirred melts of copper contained in calcia-stabilized zirconia crucibles (2.5 mm thick). Dissolved oxygen was electrochemically pumped from the melt, through the solid electrolyte, into air. This was accomplished by applying an external potential between the copper melt that served as the cathode and a porous platinum anode, coated on the external wall of the crucible. For a typical deoxidation experiment at 1150°C and an applied voltage of 3V, they were able to achieve a current density of 93 $mA/cm^2$ with an ionic resistance of 0.318Ω. The oxygen concentration of the melt (830g) was reduced from 300 ppm down to less than 10 ppm in 8 minutes.

Oberg et. al. [5] pointed out that applied potentials would not lead to decomposition of zirconia, so long as oxygen was available to the electrolyte. However, in case of high deoxidation rates and/or low oxygen concentrations in the melt, adequate supply of oxygen to the electrolyte may no longer be possible, leading to extremely low melt/electrolyte interface oxygen concentrations. It is well known that at low oxygen concentrations, stabilized zirconia exhibits significant n-type electronic conduction. Only the passage of oxygen ions and, therefore, the ionic current is effective in carrying out the deoxidation. Under such circumstances, application of an external potential leads to reduced current efficiencies[7] and can, in extreme cases, bring about electrolyte dissociation[5]. Odle et. al. [7] extended the study conducted by Oberg et. al. [5] and elaborated on the characteristics and mechanism of electrochemical deoxidation. They measured melt/electrolyte interface oxygen concentrations to determine the fraction of the ionic current effective in deoxidizing the melt in the presence of electronic currents and concluded that electronic currents are insignificant at high oxygen concentrations (> 300ppm). The oxygen concentration of a copper melt (1133g) was reduced from 600ppm to 10ppm in 30 minutes (applied voltage 1V, current density 80 $mA/cm^2$, electrolyte thickness 4.3 mm, ionic resistance 0.12Ω).

In addition to low oxygen concentrations, the electronic conductivity of stabilized-

zirconia increases exponentially with temperature. This further limits the application of stabilized-zirconia electrolytes in electrolytic deoxidation that is carried out at high temperatures (e.g. at steel-making temperatures). Etsell[14] and Iwase[15] reported that the current efficiency during electrolytic deoxidation of liquid iron was less than 70% at concentrations of oxygen below 300 ppm.

Iwase et. al. [3] realized the disadvantages of electrolytic deoxidation and instead used the electronic conductivity of stabilized-zirconia electrolytes to galvanically deoxidize liquid iron. In their study, a 2mm thick, one-end closed calcia-stabilized-zirconia (CSZ) tube was inserted into liquid iron (1823K) contained in an alumina crucible. The inside of the zirconia tube was flushed with a $CO/CO_2$ gas mixture. The resulting oxygen-chemical-potential gradient led to the migration of oxygen ions from the melt to the reducing gas mixture. The oxygen removal was possible because the residual electronic conductivity of CSZ allowed the compensating electrons to migrate in the opposite direction across the electrolyte. The initial oxygen content (580 ppm) decreased to 300 ppm after 200 minutes of galvanic deoxidation.

Hasham et. al. [1] and Yuan et. al. [8] have pointed out that the exponential decrease in the electronic conductivity of stabilized zirconia with temperature would render Iwase's method unsuitable for deoxidation of metals such as copper, which is carried out at lower temperatures (at 1200°C). Furthermore, the absence of a metallic anode in Iwase's experimental setup impedes the reaction kinetics at the anode[9]. Their solution to the problem consists of providing an alternate path for the compensating electrons to migrate, in order to maintain electroneutrality. The refining device consists of a one-end-closed YSZ tube, whose interior is flushed with a reducing gas (forming gas or $H_2$) and the tube is immersed in a bath of molten metal. In the deoxidation experiments described by Hasham et. al. [1], the inside wall of the YSZ electrolyte tubes was coated with a layer of an electronically-conducting Mo-YSZ porous cermet electrode, and steel melts were deoxidized by externally short-circuiting the melt with the cermet electrode. Yuan et. al. [8] similarly employed Ni-YSZ cermet anodes to deoxidize copper melts and obtained current densities on the order

of 10 $mA/cm^2$ for an electrolyte thickness of 1.6 mm.

## 2.2 Process Mechanism

### 2.2.1 Overview

Several authors have elaborated on the characteristics and mechanism of electrochemical deoxidation[1, 3, 5, 7, 8]. As illustrated in Fig. 2-1, the steps involved in the deoxidation process include the following:

1. Diffusion of oxygen atoms from the bulk of the melt to the melt/electrolyte interface.
2. Electrode reaction at the melt/electrolyte interface:

$$\underline{O} + 2e^- \rightarrow O^{2-} \tag{2.1}$$

3. Transport of oxygen ions through the solid-oxide electrolyte to the electrolyte/reducing gas interface.
4. Electrode reaction at the electrolyte/reducing gas interface:

$$O^{2-} \rightarrow 2e^- + \frac{1}{2}O_2(g) \tag{2.2}$$

5. Diffusion of oxygen molecules through the porous electrode into the bulk of the reducing gas.

In the list above, the electrode reactions have been represented in a phenomenological manner and actually consist of a series of steps. At the melt/electrolyte interface, the electron-transfer reaction is believed to involve the adsorption of dissolved oxygen on the electrolyte surface, which is followed by an electrochemical reduction reaction at the electrolyte[5]. Step 2 can therefore be represented as follows:

$$\underline{O} \rightarrow O_{ads}$$

$$O_{ads} + 2e^{'} + V_{\ddot{O}} \rightarrow O_O^x$$

where, $\underline{O}$ represents dissolved oxygen in the melt, $O_{ads}$ is an adsorbed oxygen atom on the electrolyte surface, $V_{\ddot{O}}$ is a doubly-ionized oxygen vacancy (in the Kröger-Vink notation), and $O_O^x$ is an oxygen atom on a normal lattice site in the zirconia lattice.

In the present study, Ni-YSZ cermet electrodes were used as anodes in a $H_2$ atmosphere. Similar Ni-YSZ cermet systems are widely used as fuel electrodes in solid-oxide fuel cells (SOFC's)[16]. Recently, several studies have been conducted in order to elucidate the reaction mechanism at the cermet anode of SOFC's in $H_2$-$H_2O$ atmospheres. The results of these studies can be used to discuss possible reaction paths for step 4 and lead to conclusions that the electrode reaction takes place through the triple-phase boundary (TPB) of $H_2$-$H_2O$/Ni/YSZ and that the reaction site of the rate-determining reaction process is on the Ni surface in the vicinity of the TPB[17, 18].

Jiang[17] proposed a reaction model for $H_2$ oxidation in the presence of water vapor, produced *in situ* by the oxidation reaction. The interaction of $H_2O$ with the Ni surface results in the dissociation of the molecule. Hydrogen gas is released and the Ni surface is covered with a layer of $O_{ads}$ atoms. Possible reaction steps could include the following:

Dissociative adsorption of $H_2$:

$$H_2(g) = 2H_{ads,YSZ}(on\ YSZ\ surface)$$

$$H_2(g) = 2H_{ads,Ni}(on\ O_{ads}\ covered\ Ni\ surface)$$

$$\left\{ \begin{array}{c} H_{ads,YSZ} \\ H_{ads,Ni} \end{array} \right\} \rightarrow H_{ads,rs}$$

where, the third step represents the migration of adsorbed hydrogen atoms to the reaction site (rs), which could possibly be the TPB.

Charge transfer reaction:

$$O_O^x = O_{ads,YSZ}^{2-} + V_{\ddot{O}}$$

$$O_{ads,YSZ}^{2-} \rightarrow O_{ads,rs}^{2-}$$

$$O_{ads,rs}^{2-} + H_{ads,rs} = H_2O_{gas} + 2e^-$$

In order to elucidate the reaction mechanism at the anode of SOFC's in $H_2 - H_2O$ atmospheres, Mizusaki et. al. [19] employed Ni stripe pattern electrodes on the surface of YSZ. They showed that the rate-determining reaction process can be considered to take place on the Ni surface and assumed $O_{ads}$ and $H_2O_{ads}$ as the adsorbed species on the Ni surface. The rate-determining reaction was expressed as:

$$H_2(g) + O_{ads} \rightarrow H_2O_{ads} \tag{2.3}$$

and, the following equilibrium was assumed to hold between the gas phase and the surface:

$$H_2O + V_{ads} = H_2O_{ads} \tag{2.4}$$

where, $V_{ads}$ denotes a vacant adsorption site on the Ni surface. Since eq. 2.4 holds, $H_2O_{ads}$ formed by eq. 2.3 easily desorbs and, with a combination of eqs. 2.3 and 2.4, $O_{ads}$ is removed from the Ni surface.

During electrochemical deoxidation, only two steps of the indicated reaction sequence are likely to be significant in controlling the overall rate, namely oxygen diffusion in the melt (step 1) and/or transport of oxygen in the electrolyte (step 3)[1, 5, 8]. At operating temperatures above 1273K and relatively small current densities (0.5-250 mA/cm$^2$), the electrode reactions and gas-phase diffusion in SOFC's are known to be very rapid and therefore, not rate controlling[8, 20]. Taking these facts into consideration, Yuan et. al. [8] have provided a detailed analysis of the galvanic deoxidation process. The next section briefly discusses the theoretical aspects of the deoxidation analysis.

### 2.2.2 Deoxidation Analysis

A galvanic deoxidation process involving a solid electrolyte such as stabilized zirconia (which exhibits mixed electronic and ionic conduction), and an external load can be represented by an equivalent electric circuit, as shown in Fig. 2-2. Yuan et. al. [8] have derived a general expression for the ionic current through a solid-oxide electrolyte, under the influence of an oxygen-chemical-potential gradient and an external load. Their analysis is based on irreversible thermodynamics and assumes that the electrodes are reversible. For a solid-oxide electrolyte that is predominantly an oxygen-ion conductor, ionic transport through the electrolyte is described by the following equation:

$$i_{ion} = Faj_{O^{2-}} = \frac{RT}{4Fr_{total}} \ln \frac{P^i_{O_2}}{P^r_{O_2}} + \frac{RTaR_{ex}}{r_{total}Fd}\{\sigma^\circ_e (P^r_{O_2})^{-1/4} - \sigma^\circ_e (P^i_{O_2})^{-1/4}\} \qquad (2.5)$$

where, $i_{ion}$ is the ionic current through one electrolyte cell, F is the Faraday constant, a is the electrolyte/melt interfacial area, $j_{O^{2-}}$ is the flux of oxygen ions through the electrolyte, R is the gas constant (= 8.314), T is the melt temperature, $r_{total} = R_{ex} + r_{ion}$, $R_{ex}$ is the external lead resistance, $r_{ion}$ is the ionic resistance of a single electrolyte cell, $P^i_{O_2}$ and $P^r_{O_2}$ are the oxygen partial pressures at the melt/electrolyte interface and in the reducing gas, respectively, d is the thickness of the electrolyte, and $\sigma^\circ_e$ is a parameter that describes the electronic conductivity of the electrolyte.

In eq. 2.5, Yuan et. al. [8] have assumed that $R_{ex}$, $r_{ion}$ and the electronic resistance of the electrolyte, $r_{el}$, completely describe the resistive paths involved in the equivalent circuit and that, in stabilized zirconia, the variation of electronic conductivity ($\sigma_e$) with oxygen partial pressure ($P_{O_2}$) can be represented by $\sigma_e = \sigma^\circ_e P^{-1/4}_{O_2}$ . However, in the case that an imperfect interface exists between the cermet anode and the YSZ electrolyte, an additional "contact" resistance, $r_{con}$ will have to be incorporated in the analysis. In addition, Yuan et. al. have analyzed the process for a single deoxidation cell, whereas, in the present study, several solid-electrolyte cells were employed in the deoxidation process. When the "contact" resistance, $r_{con}$ is included and multiple electrolyte cells are considered,

the equivalent circuit is modified as shown in Fig. 2-3 and the ionic current through each electrolyte cell, $i_{ion}$, can be represented as follows:

$$i_{ion} = Faj_{O^{2-}} = \frac{RT}{4Fr_{tot}} \ln \frac{P^i_{O_2}}{P^r_{O_2}} + \frac{RTanR_{ex}}{r_{tot}Fd}\{\sigma^\circ_e(P^r_{O_2})^{-1/4} - \sigma^\circ_e(P^i_{O_2})^{-1/4}\} \tag{2.6}$$

where, $r_{tot} = nR_{ex} + r_{ion} + r_{con}$, and n is the number of one-end closed tubes used in the refining unit.

Transport of oxygen to the melt/electrolyte interface can be modeled using the film theory[21]. A thin unmixed film or boundary layer is assumed to exist in the melt next to the melt/electrolyte interface. This film is continuously exposed to the completely mixed bulk melt, and is supposed to offer all the resistance to the transfer of oxygen atoms from the bulk to the interface. In the present study, the melt was induction stirred, and therefore, the assumption stated above is believed to be satisfied. The entire concentration change from $C_b$ to $C_i$ is assumed to take place within the boundary layer in a steady-state manner, and the mass-transfer coefficient, $\alpha$, is defined by

$$J_O = \alpha(C_b - C_i)$$

where, $J_O$ represents the flux of oxygen atoms to the electrolyte surface and $C_b$, $C_i$ are the oxygen concentrations (in ppm) in the bulk of the melt and at the melt/electrolyte interface, respectively.

Assuming that there is no accumulation of oxygen ions at the metal/electrolyte interface, the ionic current can be represented in terms of the oxygen flux in the melt:

$$i_{ion} = \frac{2FJ_O a\rho_{melt}}{M_O \times 10^6} = \frac{2\alpha Fa(C_b - C_i)\rho_{melt}}{M_O \times 10^6} \tag{2.7}$$

where, $M_O$ is the atomic mass of oxygen and $\rho_{melt}$ is the density of the melt. If the melt is assumed to be homogeneous prior to deoxidation ($C_0$ = initial oxygen concentration in the melt (in ppm) at t=0), mass balance considerations can be used to show that after

galvanic deoxidation for time t, the bulk oxygen concentration can be represented as follows:

$$C_b = C_0 - \int_0^t \frac{i_{ion} M_O \times 10^6}{2F m_{melt}} d\zeta \tag{2.8}$$

where, $m_{melt} = \frac{M_{melt}}{n}$ is the mass of the melt ($M_{melt}$) per cell.

### Negligible Electronic Conductivity

When electronic conductivity is small, either due to small $\sigma_e^\circ$ or high $P_{O_2}$, eq. 2.6 can be simplified as

$$i_{ion} = \frac{RT}{4Fr_{tot}} \ln \frac{P^i_{O_2}}{P^r_{O_2}} \tag{2.9}$$

Using Sievert's law, the oxygen concentrations can be represented in terms of the oxygen partial pressures by the following equations:

$$C_i = K_s (P^i_{O_2})^{1/2} \tag{2.10}$$

$$C_r = K_s (P^r_{O_2})^{1/2} \tag{2.11}$$

$C_r$ represents the oxygen concentration in the melt that would be in equilibrium with the reducing gas. Sievert's constant, $K_s$ is the equilibrium constant for the reaction

$$\frac{1}{2} O_2(g) = \underline{O}(melt) \tag{2.12}$$

In the present study, the deoxidation experiments were conducted on copper melts, and $K_s$ was calculated by utilizing the free energy data (for eq. 2.12) provided by Oberg et. al. [22]. Eqs. 2.10 and 2.11 can be used to express eq. 2.9 in the following form:

$$C_i = C_r \exp\{\frac{2F i_{ion} r_{tot}}{RT}\} \tag{2.13}$$

Substituting for $C_i$ from eq. 2.13 and for $C_b$ from eq. 2.8 into eq. 2.7 and rearranging gives:

$$C_r \exp\{\frac{2Fi_{ion}r_{tot}}{RT}\} + \frac{i_{ion}M_O \times 10^6}{2\alpha aF\rho_{melt}} = C_0 - \int_0^t \frac{i_{ion}M_O \times 10^6}{2Fm_{melt}} d\zeta \tag{2.14}$$

During deoxidation, oxygen from the melt passes through the electrolyte into the reducing gas (hydrogen) and reacts to form water vapor. The oxygen partial pressure in the reducing gas is consequently fixed by the $H_2/H_2O$ equilibrium. Taking into account the number of moles of oxygen atoms present in the reducing gas under open-circuit condition and the number of moles of oxygen atoms pumped into the reducing gas during deoxidation, Yuan et. al. [8] have shown that $C_r$ can be calculated as follows:

$$C_r = \frac{K_s}{K_p P_{H_2}}\{P^r_{H_2O}(OC) + \frac{30 i_{ion}\tilde{R}T_{rm}}{vF}\} \tag{2.15}$$

or,

$$C_r = k_1 + k_2 i_{ion} \tag{2.16}$$

where,

$$k_1 = \frac{K_s}{K_p P_{H_2}} P^r_{H_2O}(OC)$$

$$k_2 = \frac{K_s}{K_p P_{H_2}} \frac{30\tilde{R}T_{rm}}{vF}$$

$P_{H_2}$ is the partial pressure of hydrogen in the reducing gas (which is approximately 1 atm in the present study), $P^r_{H_2O}(OC)$ is the partial pressure of water vapor in the reducing gas under open-circuit condition, $\tilde{R}$ is the gas constant (in units of $\frac{atm-liter}{mol-K}$), $T_{rm}$ is the room temperature in K and $v$ is the flow rate of the reducing gas through each cell of the refining device in l/min. $K_p$ is the equilibrium constant for the reaction

$$H_2(g) + \frac{1}{2}O_2(g) = H_2O(g) \tag{2.17}$$

and can be calculated using the thermodynamic data provided by Kubaschewski et. al. [23]. Substituting eq. 2.16 in eq. 2.14 and differentiating with respect to time leads to the following expression for the variation of ionic current through the electrolyte:

$$\frac{di_{ion}}{dt} = \frac{-\frac{i_{ion} M_O \times 10^6}{2F m_{melt}}}{\frac{2C_r F r_{tot}}{RT} \exp(\frac{2F i_{ion} r_{tot}}{RT}) + \frac{M_O \times 10^6}{2\alpha a F \rho_{melt}} + k_2 \exp(\frac{2F i_{ion} r_{tot}}{RT})} \tag{2.18}$$

When $r_{el}$ is large (low electronic conductivity), the electronic current flowing through each deoxidation cell ($i_{el}$) is negligible, and it can be shown that $I_{ex} = n i_{ion}$ (see Fig. 2-3). Under such conditions, the deoxidation process can be modeled with eq. 2.18, by using the external short-circuit current, $I_{ex}$, at any time t, and relevant experimental parameters. Eq. 2.8 can then be used to model the decrease in the oxygen concentration of the melt with time.

### Appreciable Electronic Conductivity

Electronic conductivity of stabilized zirconia increases exponentially with increasing temperature and decreasing oxygen partial pressure. Under such conditions the electronic conductivity can no longer be ignored and the oxygen-ion flux through the electrolyte needs to be expressed by eq. 2.6 instead of eq. 2.9. Substituting eqs. 2.10 and 2.11 in eq. 2.6 gives:

$$i_{ion} = \frac{RT}{2F r_{tot}} \ln \frac{C_i}{C_r} + \frac{n R_{ex}}{r_{tot}} \frac{RTa}{Fd} \{\sigma_e^\circ (\frac{C_r}{K_s})^{-\frac{1}{2}} - \sigma_e^\circ (\frac{C_i}{K_s})^{-\frac{1}{2}}\} \tag{2.19}$$

Substituting eq. 2.8 in eq. 2.7 to eliminate $C_b$ and differentiating gives:

$$\frac{di_{ion}}{dt} = -\alpha a \rho_{melt} \{\frac{i_{ion}}{m_{melt}} + \frac{2F}{M_O \times 10^6} \frac{dC_i}{dt}\} \tag{2.20}$$

Using eq. 2.16 to eliminate $C_r$ and differentiating eq 2.19 gives:

$$\{1 + \frac{RT}{2F r_{tot}} \frac{k_2}{k_1 + k_2 i_{ion}} + \frac{n R_{ex}}{r_{tot}} \frac{RT \sigma_e^\circ a K_s^{\frac{1}{2}}}{2Fd} \frac{k_2}{(k_1 + k_2 i_{ion})^{\frac{3}{2}}}\} \frac{di_{ion}}{dt} =$$

$$\{\frac{RT}{2F r_{tot}} \frac{1}{C_i} + \frac{n R_{ex}}{r_{tot}} \frac{RT \sigma_e^\circ a K_s^{\frac{1}{2}}}{2Fd} \frac{1}{C_i^{\frac{3}{2}}}\} \frac{dC_i}{dt} \tag{2.21}$$

With $C_b$ set equal to the initial oxygen concentration in the melt (determined through sampling), eqs. 2.19 and 2.7 can be solved to obtain the ionic current, $i_{ion}(0)$, and the oxygen

concentration at the melt/electrolyte interface, $C_i(0)$, at time $t = 0$. These initial conditions are used to obtain $i_{ion}(t)$ by solving eqs. 2.20 and 2.21, which form a system of first-order differential equations in two variables ($i_{ion}(t)$ and $C_i(t)$). The following relationship between $i_{ion}$ and $I_{ex}$[8] can now be used to model the variation of external current with time.

$$I_{ex} = \frac{RT}{4FR_{ex}} \ln \frac{P^i_{O_2}}{P^r_{O_2}} - \frac{i_{ion}(r_{ion} + r_{con})}{R_{ex}}$$

**Parameters Required for Modeling**

As indicated above, values of several parameters need to be known in order to model the deoxidation process. These parameters can be divided into three different types, depending upon the manner in which they are acquired:

1. Experimental parameters: These are purely experimental variables and include the mass of the melt ($M_{melt}$), the partial pressure of $H_2$ in the reducing gas ($P_{H_2}$), the volumetric flow rate of the reducing gas in l/min ($v$), the temperature at which deoxidation is carried out (T), the melt/electrolyte interfacial area (a), the outer and inner diameter of the electrolyte tube, the density of the melt ($\rho_{melt}$) and the external resistance, $R_{ex}$ (measured using a micro-ohmmeter - Cambridge Technology Inc. Model 510A).

2. Literature data: Theoretical constants include the atomic mass of oxygen ($M_O$), the Faraday constant (F), and the gas constant ($\tilde{R}$ and R). In addition, this group includes $K_s$ and $K_p$ which, as described previously, can be calculated using the following thermodynamic data:

$$K_s = \exp(\frac{90374 - 22.175T}{RT}) \tag{2.22}$$

$$K_p = \frac{P_{H_2O}}{P_{H_2} P^{\frac{1}{2}}_{O_2}} = \exp(\frac{246438 - 54.39T}{RT}) \tag{2.23}$$

3. Calculated parameters: These parameters are calculated directly from experimental results. The first parameter in this category is the partial pressure of water vapor in

the reducing gas, under open-circuit condition, $P^r_{H_2O}(OC)$. If electronic conductivity is neglected, the measured open-circuit potential can be represented by the Nernst equation

$$E_{OC} = \frac{RT}{4F} \ln \frac{P^i_{O_2}(OC)}{P^r_{O_2}(OC)} = \frac{RT}{4F} \ln \frac{(\frac{C_i(OC)}{K_s})^2}{P^r_{O_2}(OC)} \tag{2.24}$$

and $C_i(OC)$ can be approximated to be equal to the bulk oxygen concentration. Before short circuiting the melt with the anode, a measurement of $E_{OC}$ and $C_0$ therefore enables one to calculate $P^r_{O_2}(OC)$. Eq. 2.23 is then used to calculate $P^r_{H_2O}(OC)$.

The measured external current during deoxidation is used to calculate the mass-transfer coefficient of oxygen in the melt, $\alpha$. During the final stages of the deoxidation process, when the external short-circuit current is small, it is possible to show that the following relation holds[1]:

$$\ln I_{ex} - \ln\{I_{ex}(0)\} = -\frac{\alpha a \rho_{melt}}{m_{melt}} t \tag{2.25}$$

A linear regression of $\ln I_{ex}$ vs. t towards the end of deoxidation therefore yields $\alpha$.

Finally, the electronic conductivity parameter, $\sigma^\circ_e$ and the ionic conductivity, $\sigma_{ion}$, were determined using coulometric titration and four-probe DC techniques, respectively. Chapter 3 describes relevant experimental details. $\sigma_{ion}$ is subsequently used to calculate $r_{ion}$.

The description above indicates that all parameters required for modeling the deoxidation process are known, except for $r_{con}$. $r_{con}$ is a variable which is iteratively adjusted such that the variation of external current, calculated using the model, matches the experimental one. This method is used to estimate the cermet/electrolyte interface contact resistance.

### 2.2.3 Modeling Results

Based on model calculations for their experiments, Yuan et. al. [8] conclude that the deoxidation process can be divided into two stages. The modeled ionic current, external current, and concentration vs. time curves for a typical deoxidation experiment conducted by Yuan

et. al. are shown in Fig. 2-4. In the range of high concentrations (Zone I), the removal of oxygen is controlled by the electronic and ionic resistances of the electrolyte as well as $R_{ex}$. In this zone, as shown in Fig. 2-4, the bulk oxygen concentration decreases linearly with time. In the lower oxygen concentration range (Zone II), when the interfacial oxygen concentration is close to zero, transport of oxygen from the bulk to the melt/electrolyte interface becomes the rate-controlling step and the external current is characterized by an exponential decay (see Fig. 2-4).

Similar results have been obtained by previous workers. For deoxidation of liquid iron with liquid metal/graphite anodes, Fischer et. al. [4] concluded that oxygen-ion transport through the solid electrolyte was the rate-controlling step at oxygen concentrations between 470 and 160 ppm, and that oxygen diffusion to the melt/electrolyte interface was rate controlling below 160 ppm. During electrolytic deoxidation of induction-stirred copper melts, Oberg et. al. [5] determined that Zone I was operative at oxygen concentrations greater than 90 ppm, and Zone II below 45 ppm. In the experiments conducted by Iwase et. al. [3], the transport of oxygen in liquid iron was determined to be the rate-controlling step in the range of 580 to 300 ppm O.

Yuan et. al. [8] have identified the mass-transfer coefficient, $\alpha$ and the external resistance, $R_{ex}$, as key factors in the enhancement of deoxidation kinetics. Hasham et. al. [1] point out that the melt must have sufficient stirring intensity (provided by induction stirring), and that the total system resistance must be minimized in order to delay the start of Zone II. In order to facilitate comparison of the deoxidation studies that have been conducted to date, Table 2.1 briefly lists the experimental details for the several studies reported here, and also summarizes the results obtained.

In the present study, deoxidation of copper melts was carried out on a lab-scale and field trials were conducted using solid-electrolyte cells similar to those employed by Yuan et. al. [8]. The emphasis of the present study was on the enhancement of deoxidation kinetics and the rate-limiting factors were identified through numerical modeling and lab experimenta-

tion. The process can be divided into electrolyte-controlled and mass-transfer controlled regimes as reported by Yuan et. al. , and the achievable current density was increased from 40 to 230 $mA/cm^2$, by improving cermet/electrolyte adhesion. The next chapter describes experiments conducted in order to characterize electrolyte properties required for process modeling.

# Chapter 3

# Electrical Properties of YSZ

Process modeling plays an integral role in identifying factors limiting deoxidation kinetics and, therefore, in efforts directed towards improving the commercial feasibility of the electrochemical refining technique. As described in section 2.2.2, the ionic and electronic conductivity properties of the YSZ electrolyte tubes need to be characterized in order to model the deoxidation kinetics. The present chapter describes the experimental setup and procedures used to determine the conductivity parameters and presents the results obtained.

YSZ is fabricated by commercial manufacturers and university laboratories in a variety of ways, including hot isostatic pressing, tape casting, electrochemical vapor deposition, slip casting etc. The oxygen-ion-conducting properties of stabilized-zirconia materials depend on the fabrication technique, dopant concentration, and phase assemblage[24, 25]. In order to understand the conductivity behavior in zirconia-based electrolytes, a knowledge of the phase assemblage is essential. Pure $ZrO_2$ exists in three different crystal structures: monoclinic (m), tetragonal (t), and cubic (c)[26]. At room temperature, m-zirconia is the stable form. During heating, $m - ZrO_2 \rightarrow t - ZrO_2$ and $t - ZrO_2 \rightarrow c - ZrO_2$ phase transformations occur at 1170 and 2370°C respectively. The cubic phase is stable upto the melting point (2680°C) of zirconia. Several metal oxides (MO and $M_2O_3$) stabilize the high-temperature cubic and tetragonal structures at lower temperature by forming solid solutions with $ZrO_2$. If the stabilizer or dopant content is not sufficient to fully stabilize the cubic structure, then the material may consist of a mixture of the cubic and monoclinic

(or tetragonal) phases and is called partially-stabilized zirconia (PSZ).

In addition to stabilizing zirconia, the addition of di- or trivalent oxides creates a large concentration of oxygen vacancies by charge compensation according to the following equation (written for $Y_2O_3$ stabilization using Kröger-Vink notation):

$$Y_2O_3 \rightarrow 2Y'_{Zr} + V_{\ddot{O}} + 3O^x_O$$

The high oxygen-vacancy concentration gives rise to high oxygen-ion mobility and oxygen-ion conduction takes place in stabilized zirconia by movement of oxygen ions via vacancies[16]. In general, the ionic conductivity of stabilized zirconia is independent of oxygen partial pressure over several orders of magnitude. In the present study, zirconia stabilized with 5.1 mol% yttria was used as the electrolyte. Fig. 3-1 shows a phase diagram of the $ZrO_2 - Y_2O_3$ system[16]. A Rigaku IU300 DMAX-B wide-angle diffractometer was used to analyze the phase assemblage in the electrolyte. Fig. 3-2 shows a typical XRD pattern obtained. Intensities in the angular regions 27 to 32°, 33 to 38°, and 71 to 77° ($2\theta$) were used (planes of the form {111}, {200}, {400} respectively) to distinguish the polymorphs[27]. The major phases were found to be cubic and tetragonal. The electrolyte composition was determined through electron micro-probe analysis (EPMA) and a JEOL 300 scanning electron microscope was used for the purpose. The scanning electron micrograph used to analyze the composition of the electrolyte is shown in Fig. 3-3. The presence of a glass phase ($Al_2O_3/CaO/SiO_2$) between the YSZ grains should be noted. The glass phase is used by the manufacturer as a binder for the starting material powders. The results of EPMA analysis are provided in Table 3.1. The PSZ material was selected as the electrolyte because it possesses better thermal shock resistance than fully-stabilized zirconia[26]. The commonly accepted toughening mechanism for materials with the tetragonal phase is the stress-induced transformation of the tetragonal phase to monoclinic zirconia[25]. Microcracking has also been identified as an important toughening mechanism in $ZrO_2$-based materials[26].

## 3.1 Ionic Conductivity Measurement

The ionic conductivity of the electrolyte was measured by the four-point-probe method. The principle of the four-point technique is shown in Fig. 3-4. Four Pt wires (0.02" dia, Engelhard Clal) were attached to a flat-bottom YSZ tube ($ZDY-4_l$, 3/8" OD, 1/4" ID, 12" long, Coors Ceramics Company) with Pt paste (Engelhard Pt ink 6926) as shown in Fig. 3-4. The Pt leads ran to the specimen through insulating alumina tubes. On applying a constant current, $i$, through the two outer contacts, a voltage drop, $\Delta$U, across the two inner contacts was recorded. Solartron Instruments SI1287 potentiostat was used for the purpose. A straight line was obtained when the voltage drops were plotted versus applied current values. For the geometry given in Fig. 3-4, the ionic conductivity, $\sigma_{ion}$, of the electrolyte was calculated through the following expression:

$$\frac{1}{\sigma_{ion}} = \frac{i}{\Delta U} \times \frac{\pi}{4} \frac{d_o^2 - d_i^2}{l}$$

where, $d_o$ is the outer diameter of the YSZ tube, $d_i$ the inner diameter and $l$ is the distance between the inner contacts. Measurements were carried out between 1200 and 1650°C , at intervals of 50°C. The variation of ionic conductivity with temperature can be represented by the semi-empirical equation[28]:

$$\sigma_{ion} = \frac{C_i}{T} \exp(\frac{-E_i}{kT})$$

where, $E_i$ is the activation energy and $C_i$, a pre-exponential constant. Data for the variation of $\sigma_{ion}$ with temperature (in air) is shown in Fig. 3-5. The $\ln \sigma_{ion} T$ vs. 1/T plot shows two straight lines, one in the low-temperature range (1200 - 1440°C) and the second in the high-temperature range (1440 - 1650°C). In anticipation of the fact that the conductivity is entirely ionic for the experimental conditions, the results for $E_i$ and $C_i$ are listed in Table 3.2. The break in the Arrhenius diagram at 1440°C is assumed to be due to phase changes in the binder present between YSZ grains. In order to verify the conclusion, similar measurements were carried out for YSZ tubes of the same composition, fabricated without the binder (ZDY-9 flat-bottom YSZ tubes, Coors Ceramics Company). The break in the Arrhenius diagram was not present for ZDY-9 tubes (see Fig. 3-5) and the ionic

conductivity was slightly higher as compared to ZDY-4 tubes.

From the experimental results, the ionic conductivity of the YSZ electrolyte tubes used in the present study ($ZDY-4_s$ round-bottom YSZ tubes, 0.528″ OD, 0.05″ thick, 8″ long, Coors Ceramics Company) is calculated to be 0.196 S/cm at 1200°C. Scaife et. al. [29] reported a value of 0.22 S/cm for 5.8 m/o YSZ. The ionic conductivity-temperature data for various $Y_2O_3$-$ZrO_2$ compositions as determined by Strickler et. al. [30] are shown in Fig. 3-6. The measured ionic conductivity for the ZDY-4 electrolyte tubes agrees with literature data.

## 3.2 Electronic Conductivity Measurement

Zirconia-based solid electrolytes exhibit electronic conductivity at high temperature and/or under reducing conditions. The characterization of this electronic conductivity is a necessity in any assessment of zirconia-based electrochemical devices. Under low oxygen pressures (as encountered in the hydrogen atmosphere used in the present study), the electronic conductivity is viewed as arising from the following reaction (in Kröger Vink notation)[31]:

$$O_O^x = \frac{1}{2}O_2 + V_{\ddot{O}} + 2e'$$

For heavily doped materials, the oxide-ion vacancy concentration remains constant, and the electronic conductivity at a given temperature will vary with oxygen pressure according to the following relation:

$$\sigma_e = \sigma_e^\circ P_{O_2}^{-1/4}$$

Schmalzried[32] has treated the cell-potential relationships for solid-electrolyte cells in which the electrolyte shows mixed ionic and electronic conductivity. The open-circuit potential for a zirconia-based oxygen concentration cell with oxygen pressures of $P'_{O_2}$ and $P''_{O_2}$ at the anode and cathode, respectively, ($P''_{O_2} > P'_{O_2}$) is given by:

$$E = \frac{RT}{F} \ln \frac{P_\theta^{1/4} + P_{O_2}''^{1/4}}{P_\theta^{1/4} + P_{O_2}'^{1/4}} \tag{3.1}$$

where, $P_\theta$ is the oxygen pressure at which the electronic conductivity becomes equal to the ionic conductivity.

A coulometric-titration technique as described by Swinkels[33] has been used to determine the value of $P_\theta$. Once $P_\theta$ has been determined, the electronic conductivity can be characterized using the following relationship:

$$\sigma_e^\circ = \sigma_{ion} P_\theta^{1/4}$$

An oxygen-concentration cell was made from the electrolyte tube ($ZDY - 4_l$), with a Pt-air electrode on one side and a liquid metal (Ag) electrode on the other side (see Fig. 3-7)[34]. The liquid Ag electrode is the working electrode (the electrode at which the half-cell reaction of interest occurs) and the Pt-air electrode acts as the counter electrode. The counter electrode was prepared by wrapping Pt gauze (45 mesh, Engelhard Clal) around the tube. A Pt/Pt-10%Rh thermocouple was used to serve as conducting lead for establishing electrical contact with the counter electrode. 1.5g of pure silver was melted in the zirconia tube under a stream of Ar (AIRCO grade 5, 10.2 std. ml/min) and contact to liquid silver was made via molybdenum wires (0.5 mm dia, Johnson Matthey).

As in aqueous electrochemistry, experiments were conducted using a three-electrode system, the third electrode being a reference electrode. The reference electrode was constructed by wrapping Pt wire (0.005″ dia) ≈4 mm above the counter electrode. Pt paste was used to improve electrical contact between the YSZ sample and the counter, reference electrodes. In this arrangement, a Solartron SI1287 potentiostat was used to apply a DC external current between the working and counter electrodes. However, activation (kinetic) and concentration (diffusive) polarization[35] can exist at both the working and counter electrodes and may influence the realized potential at electrode/electrolyte interfaces. The reference electrode remains unpolarized because the current is driven through the counter electrode and

a negligible current passes through the reference. If the potential was measured between the counter and working electrodes, the extraneous influences of the kinetic and diffusive limitations at the counter electrode would be incorporated in the measurement. The potentiostat, therefore, measured the potential between the reference and working electrode to determine the applied potential across the working electrode/electrolyte interface for a given value of external current[36]. Ohmic loss arising due to Mo lead wire resistance, at the working electrode, was eliminated by attaching another reference electrode (a second Mo wire) to the working electrode.

The assembled cell was heated in a resistance furnace, with an air atmosphere outside the YSZ tube. After oxygen was removed electrochemically from liquid silver to the Pt-air counter electrode, the open-circuit potential, $E_{OC}$, was measured between the reference and the working electrode, by interrupting the external current. When the oxygen partial pressure at the liquid Ag/electrolyte interface, $P'_{O_2}$, is sufficiently lowered to satisfy the condition,

$$P'_{O_2} \ll P_\theta \ll P''_{O_2}$$

eq. 3.1 can be simplified to,

$$E_{OC} = \frac{RT}{4F} \ln \frac{P''_{O_2}}{P_\theta} \tag{3.2}$$

$E_{OC}$ was obtained by interrupting the current and measuring the cell potential using a digital real-time oscilloscope (Tetronix TDS 360). Fig. 3-8 shows a typical cell-potential vs. time plot obtained during a measurement of $E_{OC}$. The instantaneous drop in potential, on interrupting the external current, corresponds to ohmic losses that occur because of resistance to the flow of ions in the electrolyte and resistance to flow of electrons through the electrode materials. In the present study, the open-circuit potential recorded after this instantaneous drop has occurred is used to calculate $P_\theta$.

The Pt/Pt-10%Rh thermocouple was used to measure the temperature of the YSZ sam-

ple and the measured potentials were corrected for the thermoelectromotive force between Pt and Mo by using Iwase et. al. 's[37] results:

$$E_t(\oplus Pt - Mo\ominus)/mV = 22.1 - 0.04T$$

Patterson[38] has shown that the parameter $P_\theta$ can be represented as,

$$\log P_\theta(atm) = A + \frac{B}{T}$$

The experimental results for ZDY-4 tubes are compared with literature data[29, 34, 39, 40] in Fig. 3-9. At 1200°C, $P_\theta$ is calculated to be $3 \times 10^{-24}$ atm and the electronic conductivity can be expressed as, $\sigma_e = 2.6 \times 10^{-7} P_{O_2}^{-1/4}$. Electronic conductivity for the YSZ tubes in the present study lies within the scatter in literature data.

# Chapter 4

# Preliminary Deoxidation Experiments

## 4.1 Experimental Setup and Procedures

The electrochemical deoxidation cell used in the present study consisted of a one-end closed YSZ tube ($ZDY-4_s$), with a porous layer of Ni-YSZ cermet deposited along the inner wall of the zirconia tube. For the initial deoxidation experiments conducted in the laboratory, the cermet was fabricated using the process described by Chou et. al. [12]. The fabrication method essentially involves a slurry-coating process and is briefly described in Fig. 4-1. A Ni tube (1/4″ OD, seamless Ni-200 tubing, Tubesales), with Ni gauze (40 mesh, Johnson Matthey) spirals welded to it, was inserted into the cermet-coated YSZ tube and served as the current collector at the cermet anode. Ni gauze spirals were used to ensure electrical contact with the cermet, while still allowing the reducing gas to flow through the annular space between the Ni rod and the cermet. Fig. 4-2 shows the electrochemical cell after assembly.

The pilot-scale trials aimed at assessing the performance of the galvanic deoxidation process developed by Yuan et. al. [8]. The trials were conducted at Reading Tube Corporation (RTC)/Cambridge Lee Industries, Reading, PA. The casting rate of copper at the plant was typically around 20 t/hr and in order to achieve a significant deoxidation rate,

it was determined that several cells of the type described above would be required (the plant trials have been described in detail in Chapter 6). A fixture was designed to hold the deoxidation cells in place and to ensure distribution of reducing gas ($H_2$) to each of the YSZ tubes. The fixture was fabricated using 306 stainless steel and consisted of two sections. The holding section had the same number of holes as the number of YSZ tubes to be used during deoxidation. The deoxidation cells were attached to the fixture by welding the Ni tubes projecting out of the YSZ tubes, to the holding section. After the required deoxidation cells were attached, a sealing plate was welded to the top of the holding section. The clearance between the holding section and the sealing plate served as a plenum for distribution of $H_2$ to the deoxidation cells (see fig. 4-3).

For the laboratory experiments, a similar fixture design was used to hold a single YSZ tube. Besides a reducing gas inlet, the sealing plate for the laboratory fixture had openings for a thermocouple (K-type, positioned in a one-end closed alumina protection tube) that was used to monitor the melt temperature, and for a feed tube that was used for adding high-oxygen copper to the melt and for sampling. The fixture was placed on a hangdown assembly (see Fig. 4-4) and a cable/winch arrangement was used to raise and lower the fixture. When the YSZ tube was lowered into the melt, a 446 stainless steel rod, welded vertically to the base plate of the hangdown assembly, dipped into the melt, making the base plate act as the cathode lead. Another 446 rod, welded to the holding section of the fixture served as the anode lead. A 1/4″-thick mica sheet was used to electrically insulate the holding section of the fixture from the base plate of the hangdown assembly. Copper wires were used to connect the cathode and the anode leads to the terminals of a double-pole, double-throw switch. The switch is open in position A and throwing it in position B leads to short circuit between the melt and the cermet anode.

Deoxidation experiments were conducted in an induction furnace (model W53/10-50 Ajax Magnethermic Corporation). An alumina tube partially filled with alumina beads was placed within the coils of the induction furnace. A quartz crucible ($3\frac{7}{8}''$ OD at top, $3\frac{1}{2}''$ OD at bottom, 1/4″ thick, 6″ height, Corning Inc.) containing a section of copper

billets cast at RTC was placed on top of the alumina beads. The alumina tube and beads protected the coils of the induction furnace, in case of crucible failure. Ceramic wool was wrapped around the alumina tube to prevent heat loss. In order to minimize temperature gradients within the molten metal, a 1/4″-thick mild-steel sheet was placed on top of the crucible. The mild-steel radiation shield had openings for the YSZ tube, feed tube, thermocouple, an Ar inlet tube and the 446 rod welded to the base plate. Ar (AIRCO grade 5) was blown over the melt at a rate of 3 l/min to prevent melt oxidation. In order to prevent heat loss and to maintain an inert atmosphere over the melt, a ceramic-fiber board (ASPA2 alumina/silica paper, 1/4″-thick, Zircar Products Inc.) was placed on top of the alumina tube, followed by a machinable glass-ceramic block (MACOR, Ceramic Products Inc.) and finally, a second ceramic board on top of the MACOR block.

The fixture was lowered to bring the bottom of the YSZ tube in contact with the top of the copper block. The charge was then heated to 1200°C at a rate not exceeding 4°C/min. Bringing the YSZ tube in contact with the charge prevented the tip of the YSZ tube from thermal shock and subsequent cracking, when immersed into the melt. In addition, thermal shock was prevented by designing the reducing gas inlet in the manner shown in Fig. 4-2. The peripheral slits avoided direct impingement of relatively cold reducing gas onto the bottom of the YSZ tube.

After the charge was molten, the hangdown assembly was lowered to immerse the deoxidation cell in the melt, with the switch in position A (open-circuit). Pin tubes were used to draw a copper sample, which was analyzed for initial oxygen concentration by LECO combustion analysis. The open-circuit potential was corrected for the thermoelectric potential between the 446 stainless steel cathode lead and Ni anode lead. A separate experiment was conducted to study the thermoelectric characteristics of the 446 stainless steel/Ni couple. The results of the experiment are shown in Fig. 4-5. A linear regression between 1100°C and 1200°C resulted in the following expression for the thermoelectric potential ($E_{Ni/446}$):

$$E_{Ni/446}/V = -3.7 \times 10^{-5}T + 0.01$$

where, the temperature is in °C and Ni is positive.

In order to deoxidize the melt, a short-circuit between the cermet anode and the melt cathode was established by throwing the switch into position B. A Hall probe (PR30, LEM/HEME) was used to measure the external current during deoxidation. A data-acquisition system (2635A Hydra Data Bucket, Fluke Corporation), that filtered electrical noise generated by the induction furnace, was used to record all experimental data. A second copper sample was drawn after deoxidation and analyzed for the final oxygen content.

## 4.2 Experimental Results

The results of a typical deoxidation experiment conducted in the manner described above are shown in Fig. 4-6. 4kg of copper was deoxidized and a mass transfer coefficient of 0.004 cm/s was obtained by carrying out a linear regression analysis between $\ln I_{ex}$ and time in Zone II (see Fig. 4-7). Fig. 4-8 compares the modeled and experimental variation of external current and bulk oxygen concentration. Division of the deoxidation process into an electrolyte-controlled and a mass-transfer-controlled regime can be seen clearly, and the agreement between the modeled and experimental variation in bulk oxygen concentration is excellent. The bulk oxygen concentration was reduced from 443 ppm to 19 ppm in ≈280 minutes. Table 4.1 lists the modeling parameters.

The total resistance, $r_{tot}$, is an order of magnitude lower when compared to $r_{total}$ for the deoxidation experiments conducted by Yuan et. al. [8] and Hasham et. al. [1] $(3 - 4\Omega)$. Yuan et. al. and Hasham et. al. used thin wires dipping in the melt and sintered to the anode to establish the short-circuit. The external resistance was therefore the most significant component in $r_{total}$. In the present study, the external resistance was lowered (to $\approx$ $10m\Omega$) by using thick rods as current collectors and higher gauge copper wires to complete the external circuit. From Table 4.1, it is evident that $r_{con}$ controls deoxidation kinetics in Zone I.

Field trials at RTC aimed at removing ≈20 ppm O from a stream of copper being continuously cast at a rate of ≈10 t/hr. The dissolved oxygen content in copper was expected to be ≈500 ppm, and therefore, transport of oxygen ions through the electrolyte would be rate controlling. If each deoxidation cell in the refining device is assumed to operate at a constant current density of 40 mA/$cm^2$ (based on the results of preliminary deoxidation experiments), the number of cells (n) that would be required can be estimated as follows:

$$\Delta C = \frac{n i_{ex} M_O \times 10^6}{2F\phi} \tag{4.1}$$

where, $\Delta C$ represents ppm O removed and, $\phi$ is the casting rate in g/sec. This calculation yields that ≈400 cells would be needed to achieve the desired amount of deoxidation (with 6″ of submergence). In an industrial environment such as at RTC, utilizing such a large number of tubes was found to be infeasible. Preliminary field visits to RTC were used to establish that the pilot-scale refining unit should consist of approximately 50 deoxidation cells. The submergence depth in the copper stream was expected to be 6″.

Having identified the contact resistance as the most significant component in $r_{tot}$, an investigation of the cermet/electrolyte interface was conducted in an effort to improve the deoxidation kinetics. Fig. 4-9 shows a scanning electron micrograph of a typical cermet prepared using the method described by Chou et. al. [12]. The imperfect adherence between the YSZ-electrolyte surface and the cermet anode layer is evident from the figure, and could possibly lead to the high contact resistance observed in the present study.

Eq. 4.1 can be used to calculate that a current density of approximately 250 $mA/cm^2$ would be required for deoxidation at RTC, if 50 cells were used to remove 20ppm oxygen, at a casting rate of 10 t/hr. The process model predicts that in order to achieve the required deoxidation kinetics with the present electrolyte tubes, the contact resistance, $r_{con}$, should be of the same order as $r_{ion}$ ($\approx 0.1\Omega$).

The cermet fabrication process was modified in order to obtain adherent cermet an-

ode layers and therefore decrease the contact resistance. The next chapter describes the procedure developed for depositing the cermet. The results obtained from deoxidation experiments that were conducted using the improved cermet have also been discussed.

# Chapter 5

# Enhanced Deoxidation Kinetics

As identified in Chapter 4, the deoxidation kinetics required for the field trials necessitates a decrease in the contact resistance, and therefore, an improvement in the cermet electrode/electrolyte adhesion. Studies by earlier workers[41] have shown that the characteristics of slurry-coated cermet electrodes on YSZ are highly dependent on the preparation method. The present chapter, therefore, first presents a brief review of reports on the relation between performance characteristics of Ni/YSZ cermet electrodes and their fabrication methods. This is followed by a description of the slurry-coating technique developed to deposit adherent cermet electrodes for use in the field trials. The Ni/YSZ cermets have been characterized and results of laboratory experiments conducted to demonstrate the enhancement in deoxidation kinetics have been presented.

## 5.1 Literature Review on Cermet Fabrication

A porous cermet of Ni/YSZ is the most commonly used anode material in solid-oxide fuel cells, that have recently attracted much attention as efficient power generators. The anode material must be stable in the reducing environment of the fuel and must have sufficient electronic conductivity at the operating temperature. The thermal expansion of the anode must match that of other cell components to avoid delamination during fabrication and operation. The anode must adhere well and must also have sufficient, stable porosity to allow gas diffusion to the reaction sites. In addition to these requirements, other desirable

properties for the anode are fabricability and low cost. The cermet anode employed in the galvanic deoxidation process must possess identical properties.

A variety of preparation methods have been used for making Ni/YSZ cermet anodes. These methods include conventional ceramic forming techniques (tape casting, calendering), coating techniques (screen printing, slurry coating), and deposition techniques (plasma spraying, electrochemical vapor deposition). The nature of the design and assembly of the deoxidation cell in the present study permits the use of deposition techniques and slurry coating for anode fabrication. Of the available techniques, slurry coating is less expensive and was, therefore, used to form the Ni/YSZ anode layers.

There have been several reports on the relation between the performance characteristics of a Ni/YSZ cermet electrode and its fabrication method. Murakami et. al. [42] examined the relationship between the particle size of YSZ, the YSZ/Ni ratio and anode performance by slurry coating mixtures of YSZ powder (mean diameter within 0.5 to 40$\mu$m) and Ni powder (mean diameter 2.5$\mu$m). They conclude that, in general, greater than 50 wt% YSZ is required to build a continuous $ZrO_2$ network in the Ni/YSZ cermet. The continuous network of YSZ particles serves to support the Ni particles and prevents changes in dimensions and microstructure of the Ni/YSZ anode over long periods of time[16]. They also infer that an increase in the effective electrode/electrolyte reaction area as the YSZ particle size is decreased, leads to a reduction in the interface resistance and therefore, improved cell performance.

Dees et. al. [43] determined the conductivity of porous Ni/YSZ cermets at 1000°C as a function of Ni content (between 15 and 50 v/o of total solids), for two different zirconia particle sizes (23 and 47 $m^2$/g). Thin strips of Ni/YSZ cermets were fabricated by tape casting a dispersion of NiO (Baker reagent grade - 3.5 $m^2$/g) and YSZ powders. NiO was reduced to metallic Ni by a reducing gas mixture of $H_2/H_2O$ at 1000°C, which led to an increase in the porosity of the samples. In accordance with the percolation theory, they observed that the cermets were electronically conducting at Ni contents greater than 30

v/o of total solids. Below this level, a greater than three order of magnitude decrease in conductivity was observed, corresponding to a change in mechanism from electronic conduction through the Ni phase to ionic conduction through the zirconia phase. Considerable improvement in the electronic conduction of the cermet (Ni content greater than 30 v/o) was made by increasing the YSZ particle size. The increase was attributed to improved Ni particle-to-particle contact, resulting from the Ni phase being able to cover more completely the surface of the YSZ particles.

Kawada et. al. [41] studied the polarization characteristics of Ni/YSZ cermet electrodes (at 1000°C in $H_2$-$H_2O$ atms.) in order to search for an adequate fabrication condition. Standard material powders of Ni/YSZ cermet anodes were prepared by mixing NiO and YSZ powders in a ball mill. These material powders were, at first, heated at 1400-1800K (pre-calcination temperature, $T_{pc}$) for 5h and crushed, painted with i-propanol on YSZ electrolyte pellets. This was followed by sintering at 1400-1800K (sintering temperature, $T_s$) for 5h. Resulting thickness of the electrode layers was about $100\mu m$. Reduction of NiO was done by fuel gas. In accordance with the results presented by Dees et. al. [43], they observed a drastic change in interface conductivity around 30 v/o Ni and conclude that Ni content is required to be more than 30 v/o. Precalcination of electrode material powders at 1673K was found to be effective in preventing Ni from sintering and in avoiding any resulting degradation of electrode performance. When $T_{pc}$ is lower, YSZ powders shrink during sintering and this leads to a loose microstructure around NiO particles. Finally, they conclude that the electrode powders should be sintered on the electrolyte at a temperature above 1600K. They suggest that a high sintering temperature leads to a smaller electrode ohmic resistance due to the following reasons:

- It may be effective in promoting good nickel-to-nickel contact and in forming continuous electronic paths in the electrode layer.
- In addition, YSZ particles in the electrode sintered at a higher temperature make a rigid sintered framework and the reaction zone is supposed to extend into the electrode layer, and is not restricted to the electrode/electrolyte interface.

Setoguchi et. al. [44] examined the anodic properties of several metal/YSZ cermet sys-

tems. Electrode materials were mixed with turpentine oil and coated on YSZ electrolyte by firing at 1000°C for 1h. The YSZ powder (TZ-8Y, TOSOH Corp.) was heated at 1300°C for 10h before mixing with NiO. The mixture was then heated at 1400°C for 1h. Anodic overvoltage of metal/YSZ interface was related with metal-oxygen bonding strength and was found to be the smallest for Ni/YSZ anode.

Chou et. al. [12] have described the deposition and characterization of Ni-YSZ cermet electrodes that are adhering, have high stable porosity and low sheet resistance. Briefly, the process reported consists of slurry coating and sintering a layer of Ni and YSZ on the inner wall of one-end closed YSZ tubes, followed by pressure infiltrating YSZ and resintering. The process was reproducible and could consistently deposit cermet electrodes having porosity within a narrow range (30 to 37%), and sheet resistance between 0.0064 to 0.019 $\Omega/cm^2$ depending on the thickness (150 to 30 $\mu$m). These electrodes were also stable at high temperatures (1273K - 1473K). Galvanic deoxidation cells employing such cermet anodes were operated for more than 100 hours at 1200°C and could also undergo at least ten thermal cycles between 1200°C and room temperature.

Iwata[45] has reported on the relationship between anode degradation and Ni sintering in the Ni/YSZ anode. Mercury porosimetry revealed that pore distribution peaks in the radius range of 10 to 200 nm that were present in the Ni-YSZ anode substrate before testing, completely disappeared after 1015h at 1000°C. Electron microprobe observations showed that the diameter of Ni particles in the anode substrate was 0.1 to 1$\mu$m before running, whereas it increased upto 10$\mu$m after 1015h. Based on these results, the author concludes that as Ni sintering progresses, anode degradation is caused by a decrease of the contact area at the electrolyte/anode interface and a decrease in the specific surface area of Ni particles.

A study of the literature reveals that a key factor in the preparation of Ni/YSZ anodes is to tailor and control electrode morphology, because the characteristics and stability of the anode microstructure significantly affect electrode performance. The next section de-

scribes the deposition technique developed to produce adherent, stable and electronically conducting Ni/YSZ cermet electrodes for use in the present galvanic deoxidation process.

## 5.2 Fabrication and Characterization of Ni/YSZ Cermet Anodes

### 5.2.1 Fabrication

The slurry-coating process developed is schematically depicted in Fig. 5-1. Standard powders for fabrication of Ni/YSZ cermet anodes were prepared by ball milling nickel oxide and YSZ powders in a jar mill. Baker reagent grade nickelous oxide (average particle diameter - 3$\mu$m) and $ZrO_2$ - 13.16 w/o $Y_2O_3$ powders (TOSOH TZ-8Y, mean particle diameter - 0.2$\mu$m) were used as the starting materials. YSZ powder was first precalcined at 1300°C for 5 hours in air, crushed in a mortar and sieved through a US #325 sieve. Precalcined YSZ powder was then ball milled with an appropriate amount of NiO powder (such that after reduction of NiO to Ni, the Ni content in the anode layer would be 60 v/o of total solids). Milling was carried out at 50 RPM for 12 hours in a glass jar using YSZ balls as the milling media and a ball-to-powder weight ratio of 20:3. In order to break down powder aggregates that resulted on milling, the powder mixture was crushed and sieved a second time.

A slurry-coating process was used to deposit the electrode. The slurry was prepared by dispersing 7.5g of the powder mixture in 6ml isopropyl alcohol. Prior to the coating process, the YSZ tubes to be used in the deoxidation cells were washed with acetone and deionized water, followed by drying under an infrared lamp. The coating process consists of filling a YSZ tube with 2g of the slurry. The YSZ tube is held vertically, the open end of the tube is blocked and it is vibrated in order to obtain a thin, uniform coating of the slurry on the inner wall. After the slurry has been allowed to dry for approximately 3 days, the tube is heated to 1500°C at 4°C/min, sintered for 5 hours, followed by cooling to room temperature at 4°C/min. NiO was reduced to metallic Ni by heating the tube to 1200°C, under an atmosphere of Ar, followed by sintering at 1200°C for 1h under an atmosphere of forming gas (5%$H_2$ - 95%$N_2$). During the reduction step, it was observed that, instead

of producing a uniform cermet layer, stagnation of reducing gas inside the YSZ tube led to the formation of localized Ni globules. This was prevented by blowing the reducing gas directly into the YSZ tube, thus ensuring a uniform gas flow.

### 5.2.2 Characterization

#### SEM and EDX

A JEOL 6320F SEM and a Philips Electroscan Model 3 Environmental SEM were used to investigate the microstructures and morphologies of the as-prepared cermet anodes. Fig. 5-2 and Fig. 5-3 show typical SEM images for the cermet/electrolyte interface obtained using the slurry-coating method described above. From the figures it is evident that the technique produces anode coatings with uniform thickness ($\approx 20\mu$m - see Fig. 5-2) and an improved cermet/electrolyte adhesion (see Fig. 5-3), when compared with the process described by Chou et. al. [12]. A micrograph of the surface of the Ni/YSZ cermet coating is shown in Fig. 5-4. An important feature that can be observed from Fig. 5-4 is the porosity of the coating (analyzed later using mercury porosimetry) - which would allow easy gas diffusion to the reaction sites. Fig. 5-5 shows the Ni distribution (obtained with EDX) across the thickness of the cermet. The procedure employed is effective in making good nickel-to-nickel contact and therefore leads to the formation of continuous, electronically conducting paths in the electrode layer.

#### Mercury Porosimetry

A Micromeretics Autopore 9220 mercury porosimeter was used to analyze the pore radius distributions for the as-prepared cermet samples. The theory of wetting and capillarity for mercury porosimetry and the experimental method for the determination of the porous properties of a sample have been reviewed by Lowell et. al. [46]. Briefly, the method employed in mercury porosimetry involves the evacuation of all gas from the volume containing the sample. Mercury is then transferred into the sample container while under vacuum. Finally, pressure is applied to force mercury into the voids and the applied pressure and intruded volume are monitored.

Fig. 5-6 is a cumulative pore-volume intrusion curve which shows the summation of volume intruded into the pores ($V$) plotted versus the applied pressure. The surface area, S of all pores filled up to pressure P can be calculated from Fig. 5-6 using the following equation[46]:

$$S = 0.0188 \int_0^V PdV \tag{5.1}$$

where, V is in cubic centimeters and P in psia. By graphical integration, using the cumulative intrusion curve in Fig. 5-6, the surface area of all pores filled by mercury up to 30 psia is 288 $cm^2/g$. Plots of the derivative of the cumulative curves, $\frac{dV}{dP}$ versus radius are useful for the determination of the radius at which the maximum volume intrudes. Fig. 5-7 is a derivative plot calculated from the cumulative curve in Fig. 5-6. The area under the derivative plot can be used to represent pore-size distribution in the as-prepared cermet anodes, in terms of the fraction of pores that lie within specific pore-radius intervals (see Fig. 5-8). The cermets fabricated using the slurry-coating technique developed, have 75% of the pores in the pore-radius range between 10-15$\mu m$.

## 5.3 Laboratory Deoxidation Experiments Using Modified Cermet

The setup and procedure for the experiments is similar to that described for the preliminary ones (see section 4.1). The differences include the following:

- The cermet anode layers are deposited using the modified technique described above.
- The mass of copper deoxidized during an experiment was reduced and smaller quartz crucibles were used ($3\frac{1}{2}''$ OD, $1/4''$ thick, $3\frac{1}{8}''$ height, Corning Inc.).
- During the preliminary experiments it was observed that the Ni gauze spirals damage the cermet during insertion of the Ni current collector rod. In order to prevent this, Ni gauze strips ($1/4''$ wide, $1/16''$ thick) were placed in contact with the cermet before insertion of the Ni rod.

The external current vs. time curves for two deoxidation experiments are shown in Fig. 5-9. Linear regression fits between $\ln I_{ex}$ and time towards the end of the deoxidation experiments are plotted in Fig. 5-10. The calculated mass-transfer coefficients and other experimental/modeling parameters are provided in Tables 5.1 and 5.2. The modeled external current and oxygen concentration curves are in excellent agreement with the experimental ones (see Fig. 5-11).

In the electrolyte-controlled regime, a current density of 230 $mA/cm^2$ was obtained (see Table 5.2), as against 40 $mA/cm^2$ for the preliminary experiments. With the development of adherent cermet layers and the use of protective Ni strips, the contact resistance has been decreased from 0.3$\Omega$ to 0.1$\Omega$ (which, as described in Chapter 4, is the target value predicted using the process model). In addition, the mass-transfer coefficient is an order of magnitude higher, which may be attributed to increased stirring due to the lower mass of the melt.

With the improved kinetics, Eq. 4.1 predicts that 55 tubes (6$''$ submergence) will be required to remove 20 ppm O at a casting rate of 10 t/hr. This number was found to be reasonable for the deoxidation trials at RTC. The deoxidation cells for the field trials were therefore prepared using the modified cermet-fabrication procedure.

# Chapter 6

# Field Evaluation and Cell Longevity

## 6.1 Trial at Reading Tube Corporation

### 6.1.1 Current Melting and Refining Practice

Reading Tube Corporation produces phosphorus deoxidized UNS C12200 copper tubing containing a minimum of 99.9% copper and 0.015-0.04% phosphorus. The production process begins by melting No. 1 grade copper scrap in a 220 t reverberatory furnace. Fire-refining is used to remove the impurity elements in the purchased scrap. The refining technique consists of oxidizing molten copper by blowing air into the bath. The oxygen reacts with the impurity elements that have a higher oxygen affinity than copper. The blowing operation also raises the oxygen content in copper to 0.3-0.6wt.% which is reduced by poling to $\approx$0.05wt.% before the furnace is tapped.

The remaining oxygen is removed during casting, by controlling the addition of phosphorus to the stream of molten copper. The primary variables are flow of copper and the oxygen content, both of which vary significantly during the eight hour casting operation. The oxygen content tends to rise due to absorption from the furnace atmosphere and exposure of the copper stream to air. When the oxygen content rises to an unacceptable level of 0.05-0.06wt.%, the copper bath is poled again. At Reading Tube, excursions to higher

levels occur occasionally. More frequent or extended poling operations cannot be performed due to temperature losses and particulate emissions. In addition, poling becomes ineffective when the metal level in the furnace drops below 40%. Reading Tube Corporation has no method of reducing the oxygen content in the last 3.5 hours of casting.

### 6.1.2 Potential Applications and Benefits

The electrochemical deoxidation technique will enable control of the oxygen content within the desirable range throughout the casting operation. Maintaining the oxygen content within a low narrow range will result in the following benefits:

1. Thin-walled tube market opportunities and improved tube drawing: High oxygen contents in the molten stream require greater amounts of phosphorus addition. The extended time in which phosphates continue to form can lead to the entrapment of brittle and glassy phosphate inclusions in the cast billets. These inclusions cause difficulties in subsequent tube-drawing operations, especially thin-walled tubes. Application of the electrochemical deoxidation technique will eliminate/reduce the entrapment of phosphates. This aspect will result in higher production efficiencies, higher yield and aid RTC in gaining entry into the thin-wall tube market.

2. Improved phosphorus control: Dissolved phosphorus significantly degrades the electrical conductivity of copper[47]. Measuring the electrical conductivity therefore provides a simple and rapid method to estimate the phosphorus content. However, it cannot detect the presence of phosphate inclusions, because phosphorus present as an inclusion has a negligible effect on conductivity.

   To eliminate correlation errors and verify conformance to specification requirements, a direct chemical analysis is required. While a method such as optical emission spectroscopy can provide accurate results of the total phosphorus content, it cannot distinguish between the soluble and insoluble forms of phosphorus in copper. If this method were used instead of conductivity measurements during casting, samples would read

erroneously high and show more variability depending upon the amount of trapped phosphate inclusions. Some amount of phosphate inclusions float to the surface downstream of the sample location. Consequently, this would lead plant personnel to reduce addition of phosphorus to the stream and produce billets with low phosphorus contents.

Increased control over entrapment of phosphates on application of the present technique will allow the use of an optical emission spectrometer for process control and improve the reliability of segregating billets using conductivity. Using the cells to minimize variability in oxygen content will also minimize fluctuations in phosphorus additions.

### 6.1.3 Electrochemical Deoxidation Setup

A schematic of the deoxidation setup used for the pilot-scale deoxidation trials at RTC is shown in Fig. 6-1. 53 deoxidation cells, prepared as described in Section 5.3, were welded to the holding section of the fixture (see Section 4.1). The deoxidation setup was similar to the one used for the laboratory experiments, with the following modifications:

- An Inconel pipe (Schedule 80 Inconel Alloy 600 pipe, Tubesales) welded to the sealing plate served as the hydrogen inlet and was also used to raise and lower the deoxidation unit.

- In the event that some of the YSZ tubes crack during deoxidation, hydrogen distribution to each cell would no longer be uniform, as the reducing gas would preferentially flow through the cracked deoxidation cells. In order to prevent non-uniform hydrogen distribution, 0.25″ diameter Ni plates, with centrally located circular holes (0.002″ diameter), were welded to the top of each Ni rod (see Fig. 4-2). By causing the largest pressure drop in the flow line, the 0.002″ holes act as orifice meters, thus ensuring uniform gas flow to each cell. A rotameter (044-40T 150mm flowmeter, Aalborg Instruments and Controls) was used to regulate the hydrogen flow to 2.5 $l/min$ per deoxidation cell.

- 2/0 welding cable (Middlesex Gases and Technologies) was used to establish the short-circuit between the melt and the cermet. A copper connector (see Fig. 6-1) was used to attach the lead wire to the Inconel rod. Electrical contact with the melt was established by dipping several 446 rods (welded to a 306 block) in the stream.

Fig. 6-2 is a flowsheet for copper production at RTC. Copper from the reverberatory furnace flows, via a launder, into a gas-fired holding hearth to control the melt level in the tundish (the tundish is a rectangular vessel that simultaneously feeds multiple, semi-continuous casting molds). A ceramic insert, as shown in Fig. 6-3, was placed in the launder to create a relatively quiescent melt and prevent the bending of Ni tubes due to the flow of metal. In addition, the insert ensured a minimum submergence depth ($4\frac{5}{8}$") for the deoxidation cells, under variable metal flow conditions. In order to carry out deoxidation, an electric furnace was placed above the insert and the YSZ tubes were preheated in the furnace to 800°C. The preheated cells were lowered into the flowing stream of copper, with the help of a cable/winch mechanism.

### 6.1.4 Diagnostics for the field trial

The external current measured during the pilot-scale deoxidation trial is shown in Fig. 6-4. When the tap slot of the reverberatory furnace was opened, the sudden discharge of copper in the empty launder led to splashing of hot metal on the bottom of the YSZ tubes. Several YSZ tubes cracked due to the extreme thermal shock associated with the splashing. In addition, the YSZ tubes were subjected to thermal shock during preheating, which was carried out at a rate significantly greater than 4°C/min.

For the cracked YSZ tubes, the Ni current collector rods were in direct contact with the melt - providing an alternate path for current to flow between the cermet anodes of the functioning (undamaged) deoxidation cells and the melt cathode. The measured external current was, therefore, not completely representative of the oxygen content removed and the results could not be modeled. Raising the fixture (by $\approx 1''$) enabled a limited elimination of the internal short, thereby increasing the measured external current. The spikes in Fig. 6-4 represent attempts to reduce the internal short, as described above. Approximately 10

YSZ tubes were found to be undamaged at the end of the experiment and the submergence was estimated to be $3 - 4''$. Based on these approximations, the maximum current density observed during the trial was $\approx 200\ mA/cm^2$. The current density obtained compares favorably with that obtained during the laboratory experiments. The results of the trial can be used to conclude that, with an improved engineering design of the deoxidation setup, application of the electrochemical deoxidation technique on an industrial scale is feasible.

As indicated by Odle et. al. [6] and as observed in the field trial, the applicability of the technique depends upon the thermal shock resistance of the electrolyte tubes, which would necessitate a slow, careful heat-up of the tubes prior to immersion. In addition, research on solid-oxide fuel cell technology indicates that the densification of the cermet is one of the factors which limits the life of a SOFC[16]. Extended application at high temperature can lead to deterioration of deoxidation-cell performance and therefore, the kinetics of oxygen removal. The next section describes the results of experiments conducted to study the longevity of the deoxidation cells.

## 6.2 Cell Longevity

A detailed schematic of the experimental setup used to investigate the thermal-cycling life of the YSZ electrolyte tubes is shown in Fig. 6-6. The experimental arrangement consists of a YSZ tube (the inner wall coated with the cermet) sealed to an alumina support tube (3/4″ OD, 9/16″ ID, Vesuvius McDanel) with a ceramic adhesive (Ultra-Temp 516, Aremco Products Inc.).

In industrial application of the deoxidation technology, it is expected that the cells will be kept heated at approximately 1000°C (soak temperature), in order to prevent thermal shock damage between deoxidation cycles and to reduce cycle time. The expected industrial conditions were simulated by conducting the thermal-cycling experiments in a three-zone resistance heating furnace (Lindberg model 54459-V). The top zone of the furnace was heated to the soak temperature (1050°C), while the middle and the bottom zones were maintained at the deoxidation temperature (1200°C). An alumina crucible (40mm OD, 91mm height,

Vesuvius McDanel) containing 350g copper (1-10mm Cu shots, Johnson Matthey) was positioned in the central heating zone, inside an alumina furnace tube. End caps (306 stainless steel, Vesuvius McDanel) were used to seal the top and bottom of the furnace tube. The top seal had openings for a mullite tube (0.125″ OD, 0.094″ ID, Vesuvius McDanel), a 446 rod (1/4″ dia.), the alumina support tube and a thermocouple (B type) positioned in a one-end closed alumina tube. The mullite tube was used as a forming gas ($90\%N_2 - 10\%H_2$) inlet, in order to maintain a reducing atmosphere inside the furnace tube. The 446 rod was used to establish electrical contact with the copper melt and the B-type thermocouple to monitor the melt temperature (maintained constant at 1200°C). A type S thermocouple placed in contact with the closed end of the YSZ tube was used to monitor the temperature of the tip of the YSZ tube during the cycling experiment. In addition, it was used to maintain an inert Ar atmosphere inside the YSZ tube (to prevent oxidation of the cermet) and as an electrical contact with the cermet. The integrity of the YSZ tube being cycled was continuously monitored, by measuring the resistance between the melt and the cermet, during a cycling experiment. Penetration of copper, in the event that the YSZ tube cracked, would lead to a short-circuit between the melt and the cermet.

The alumina support tube was held in a pressure fitting (3/4″ Tube OD Ultra Torr Union Tee, Swagelok), which in turn was supported on a 306 stainless ring. A steel cable attached to the 306 ring was used to raise and lower the YSZ tube at a controlled rate (a Dayton motor/gearbox arrangement was employed for the purpose). An isometric view of the longevity/cycling setup is shown in Fig. 6-5. The top zone of the furnace was heated to 1050°C (at 4°C/min), with the YSZ tube in the raised position. The YSZ tube was lowered into the copper melt at a rate of $\approx 0.002\ inch/min$, kept immersed for 2 hours and raised again. During one thermal cycle, the tip of the YSZ tube was subjected to a temperature history shown in Fig. 6-7. The experimental parameters for the cycling experiments have been listed in Table 6.1.

The tubes have been tested for a maximum of 10 thermal cycles, and were held at 1050°C for 80 hrs (20 hrs immersion time in molten copper). The integrity of the cycled YSZ tube

was investigated by pressurizing it, followed by immersion in soap solution. Measurement of a resistance on the order of 10k$\Omega$ between the 446 rod and the rhodium element of the tip thermocouple, as well as the immersion test were used to conclude that the YSZ tubes did not crack during the present experiments.

The part of the YSZ tube that was immersed in copper was sectioned and the outer surface analyzed for corrosion resistance using EPMA (JEOL 733 SEM). Fig. 6-8 shows a scanning electron micrograph of the electrolyte surface after immersion in copper for 20 hours. EPMA analysis was used to conclude that copper did not penetrate in the YSZ grains or in the intergranular pores.

In order to study the long-term stability of the cermet electrodes, mercury porosimetry was carried out on cermet samples that had been used in the cycling experiments. Fig. 6-9 and Fig. 6-10 show the intrusion curves and pore-radius distributions for the cermets, as a function of time at temperature. As described in Section 5.2.2 the as-prepared cermet had 75% of the pores in the radius range of 10 to 15$\mu$m. After expt. CE2, the pore radius distribution "peaks" disappeared. In addition, pores in the radius range of 15 to 35$\mu$m, that were absent in the as-prepared cermets became prominent after expt. CE2. Table 6.2 shows the specific surface areas of the cermets obtained from mercury porosimetry data of Fig. 6-9. After expt. CE2, the specific surface area of the cermet decreased to a third of that for the as-prepared sample. The decrease in the specific surface area can be attributed to Ni sintering in the Ni-YSZ cermet anode. Figs. 6-11 and 5-5 can be used to compare the morphology and Ni distribution of electrodes before and after expt. CE2. It is important to note that though mercury porosimetry indicates a significant decrease in the specific surface area (288 to 107 $cm^2/g$), any appreciable difference could not be seen in SEM/EDX analysis. This is probably because the difference was not so large as to be observed in the micrographs.

SOFC research indicates that significant structural changes in the cermet anode can cause degradation in deoxidation cell performance[16]. Cermet densification can lead to a

decrease in the three-phase contact area and will limit the useful life of the deoxidation units. Commercial viability of the technology therefore re[illegible] the anode to maintain its dimensions and desired microstructure in long-term operati[illegible] a[illegible] elevated temperature. As reported in section 5.1, a continuous network of YSZ particles in the anode is required to prevent a change in dimensions and microstructure over long periods of time. The formation of a three-dimensional YSZ network strongly depends on fabrication conditions and starting-material characteristics and compositions. The rate of anode sintering is also dependent on the Ni particle-size distribution and increases as the wid[illegible] of Ni particle-size distribution increases and as the Ni content in the anode increases. Mercury porosimetry results on long-term stability of the cermets prepared in the present study, therefore, emphasize the need for an in-depth investigation of electrode processing to characterize and optimize cermet fabrication.

## 6.3 Future Work and Alternate Applications

The field trial conducted at RTC has demonstrated the need to develop cell assembly fixtures more suited to application in an industrial environment. In collaboration with the Idaho National Engineering and Environmental Lab (INEEL), researchers at the State University of New York at Stony Brook have directed significant effort towards the development of a process to economically manufacture deoxidation-cell structures for industrial application. The technique results in a thermally-shock resistant, compositionally-graded cell structure. The cell-manufacturing process starts with plasma spraying a layer of porous Ni (0.06″ thick) on a metallic anode mandrel and ends with plasma deposition of a 0.01″ thick, outer YSZ layer. A schematic of the cell structure is shown in Fig. 6-12. The thin electrolyte in such anode-supported cell structures leads to improved thermal-shock resistance (due to lower thermal stresses within the electrolyte layer) and a decrease in the ionic resistance, $r_{ion}$. Fig. 6-13 shows the deoxidation kinetics predicted for an anode-supported cell (3" OD, 60" submergence), based on modeling results obtained from laboratory experiments (see Table 6.3). With a predicted current density of $\approx 750 mA/cm^2$, it would be possible to deoxidize (3000 to 250 ppm) a 50 ton batch of liquid copper in 1 hour, if 100 anode-supported structures of the kind described were employed for the purpose. The process

can be used to eliminate the poling operation and will lead to a reduction in particulate emissions and soot production during fire-refining. Stricter environmental regulations in the future provide an impetus to designing cell assembly fixtures and conducting an economic analysis to assess the commercial feasibility of the technology in an industrial setting.

At high current densities, anode polarization is expected to become a limiting factor in the performance of the cell structures[20]. In addition, longevity experiments conducted during the present study have shown that Ni sintering can occur and decrease the reaction area at the anode, leading to a concurrent deterioration in cell performance with prolonged cell use. Gubner et. al. [48] have investigated the degradation of SOFC cermet anodes and report that transport of Ni via gaseous species ($NiOH_2$) can lead to loss of Ni in the porous cermet structure and that the effect is enhanced by a high oxygen activity in the fuel. Most studies on the long-term stability and electrochemical performance of cermet anodes employed in SOFC's have been conducted at a lower temperature ($800 - 1000°C$)[17, 18, 19, 41, 42, 43, 45] and, therefore, a need exists to characterize and improve the anodes used in the present deoxidation technique at higher operating temperatures and current densities.

Besides deoxidation of molten metals, the technology described has the potential to be used in electrocatalytic extraction of metals. The extraction device consists of a one-end closed YSZ tube which contains an oxide ore. A working electrode is immersed in the molten ore and a counter electrode is painted outside the tube. A potential step applied between the working and the counter electrode causes the oxide in the ore to dissociate and form the metal. The metal deposited at the working electrode can be grown as a dendrite, which autocatalytically increases the interfacial area of the working electrode and enhances the reduction-process kinetics. The process has been used in the laboratory to efficiently produce iron, ferro-alloys and lithium, from its oxide ores.

Oxygen-separation technology, essentially based on the concept described in the present study, is being used by an alliance of five global companies (including British Petroleum

and Praxair Inc.) to develop a revolutionary technology in which natural gas is converted to synthesis gas (syngas). The process uses a non-porous ceramic membrane (similar to the YSZ electrolyte in the present study) that separates oxygen from air and transports it to a methane/steam stream (see Fig. 6-14). Methane reacts with emerging oxygen and steam to produce synthesis gas. By eliminating the need for a separate oxygen production plant, the technology significantly reduces the energy and capital cost associated with syngas production.

# Chapter 7

# Summary and Conclusion

The technical feasibility of employing solid-electrolyte cells for electrochemical deoxidation of molten metals has been demonstrated by earlier workers on a laboratory scale. Though several scale-up structures have been proposed, field trials have not been conducted to date. In the present work, galvanic deoxidation technology developed by Yuan et. al. [8] has been investigated with the aim of developing a prototype pilot-scale deoxidation unit.

A single deoxidation cell consists of a one-end closed YSZ tube, the inside of which is coated with a porous Ni/YSZ cermet anode and is flushed with a reducing gas. The tube is dipped into the melt to be deoxidized and oxygen is removed by short-circuiting the melt with the cermet anode. The external lead-wire resistance involved in short-circuiting the melt with the anode was decreased to a few m$\Omega$ and through lab experimentation, the nature of anode/electrolyte adhesion was identified to be an important factor in obtaining enhanced deoxidation kinetics. Since industrial deoxidation will require multiple cells, the mathematical process model developed by Yuan et. al. [9] was appropriately modified. In addition, a contact resistance was incorporated in the model, in order to analyze anode/electrolyte interface characteristics. The contact resistance was decreased by developing a slurry-coating technique that was used to produce uniform, electronically conducting, and adherent cermet anode layers.

A pilot-scale deoxidation unit consisting of 53 deoxidation cells was manufactured and

field trials were conducted at Reading Tube Corporation/Cambridge Lee Industries, Reading, PA. These trials indicate that there exists a need to design assembly cell fixtures suited to industrial application. In addition, the deoxidation cells should be protected from thermal shock damage by ensuring a slow heat-up prior to immersion and by keeping the cells heated between deoxidation cycles. The commercial feasibility of the technique will also require enhancement of the deoxidation kinetics and a significant parallel effort at INEEL has been devoted towards the development of thin, anode-supported YSZ structures that are thermally shock resistant and can lead to high current densities, on the order of 750 $mA/cm^2$. The thermal-spraying process being developed to manufacture the large-scale structures will also lead to a reduction in cell-manufacturing cost and time, further improving economic viability.

SOFC research indicates that densification of the cermet due to prolonged exposure to high temperature will limit the useful life of the deoxidation units. Preliminary experiments were conducted to study the sintering behavior of the cermet anodes, thermal-cycling life of the YSZ tubes and the minimum life of the YSZ cells was determined to be 10 cycles (when cycled between 1050 and 1200°C). The YSZ electrolyte did not exhibit corrosion after immersion in copper for 20 hrs. Mercury porosimetry was used to analyze the cycled cermets and shows that the surface area of the porous cermet structure decreases from 288 to $107cm^2/g$ after 100 hours at temperature. Cermet densification and electrode polarization at high operating current densities can lead to a deterioration in deoxidation cell performance. An in-depth investigation of electrode processing and performance is therefore required to characterize and optimize cermet fabrication.

This study has been successful in demonstrating the technical feasibility of employing galvanic deoxidation in an industrial environment. The technology can replace pollution-intensive refining operations such as poling of copper melts and has alternative applications in the electrocatalytic extraction of metals and oxygen separation. There is a strong impetus to conduct an economic analysis to investigate the commercial feasibility of using the technique on an industrial-scale and finally, to develop a large-scale deoxidation unit.

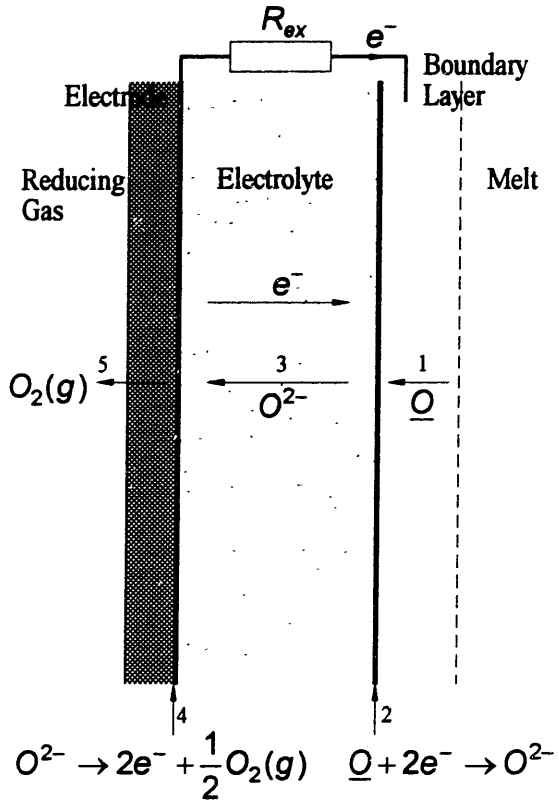


Figure 2-1: Illustration of steps involved in the deoxidation process.

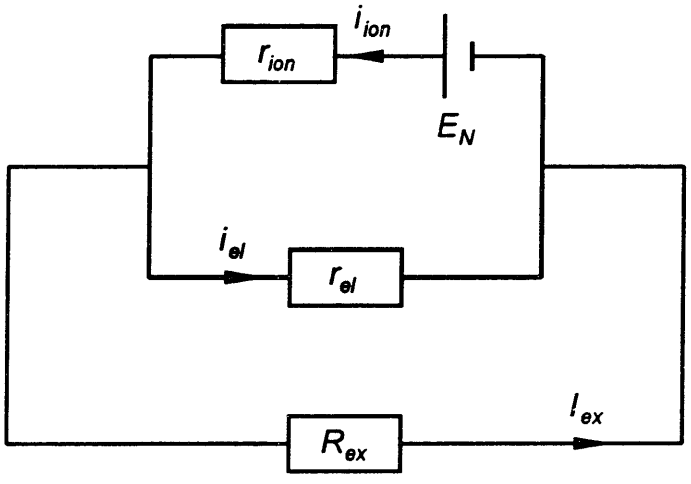


Figure 2-2: Equivalent circuit of a solid-electrolyte cell.

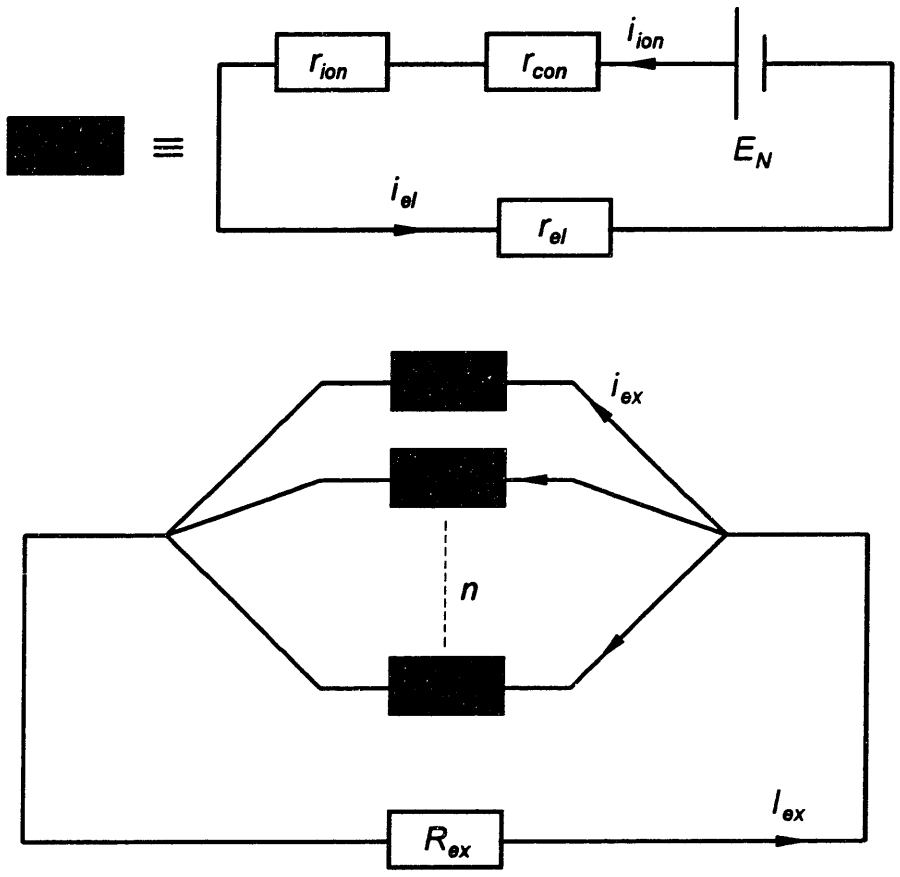


Figure 2-3: Equivalent circuit incorporating a "contact" resistance and multiple deoxidation cells.

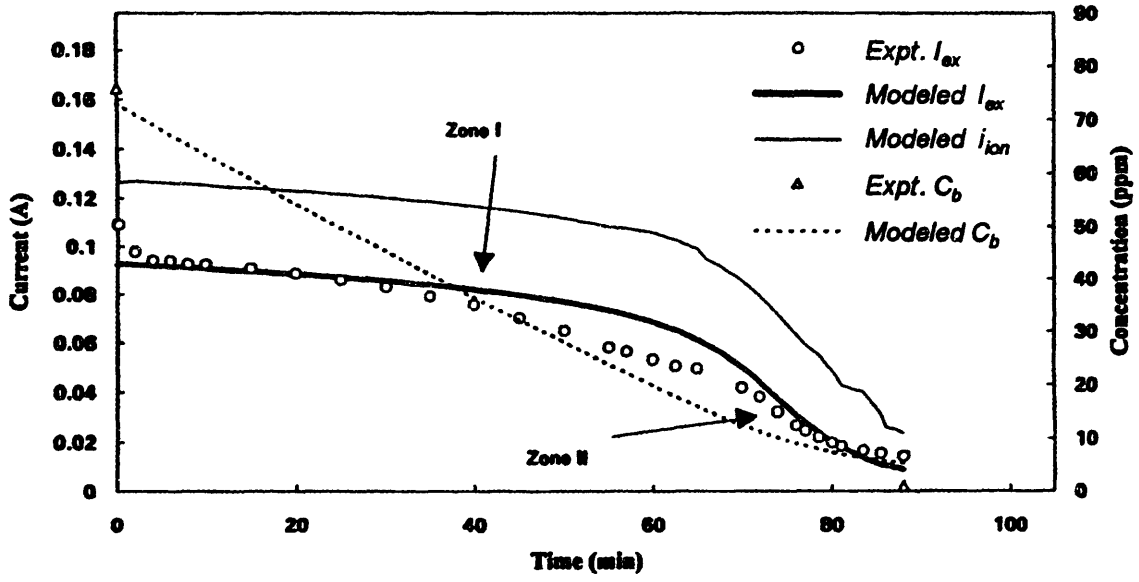


Figure 2-4: Modeled ionic current, experimental/modeled external current, and bulk oxygen concentration vs. time curves for a deoxidation experiment conducted by Yuan et. al. [9].

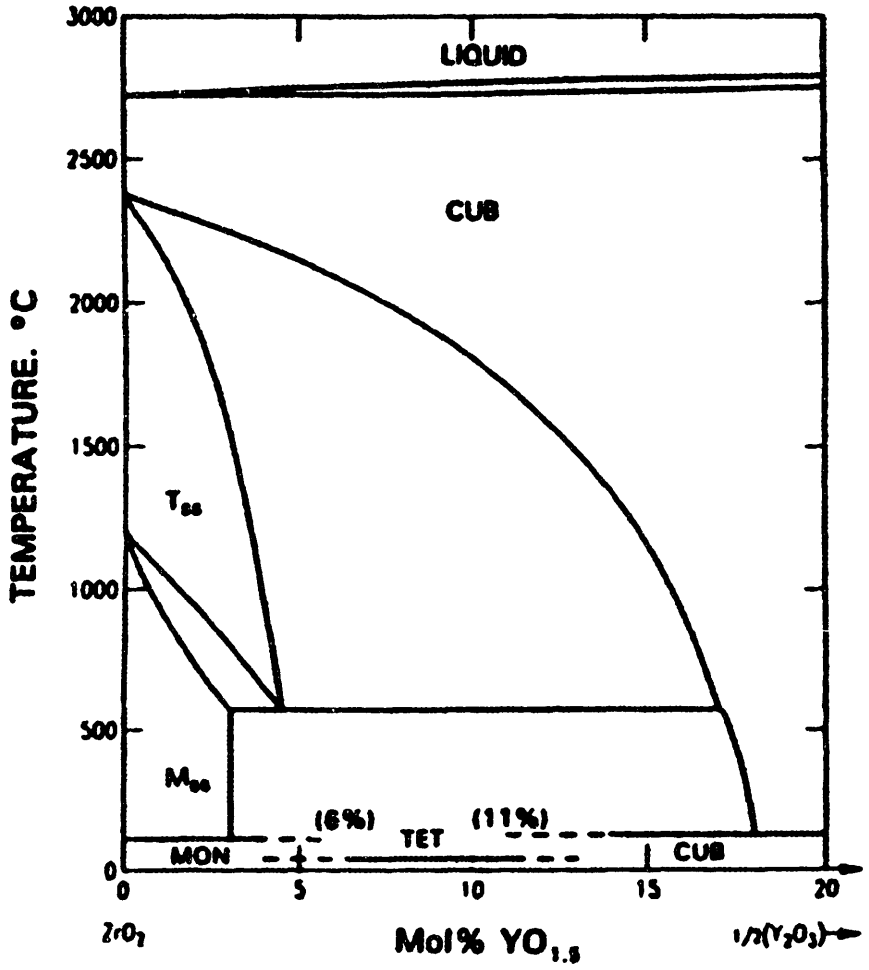


Figure 3-1: Phase diagram of a $ZrO_2$-$Y_2O_3$ system in the low $Y_2O_3$ region.

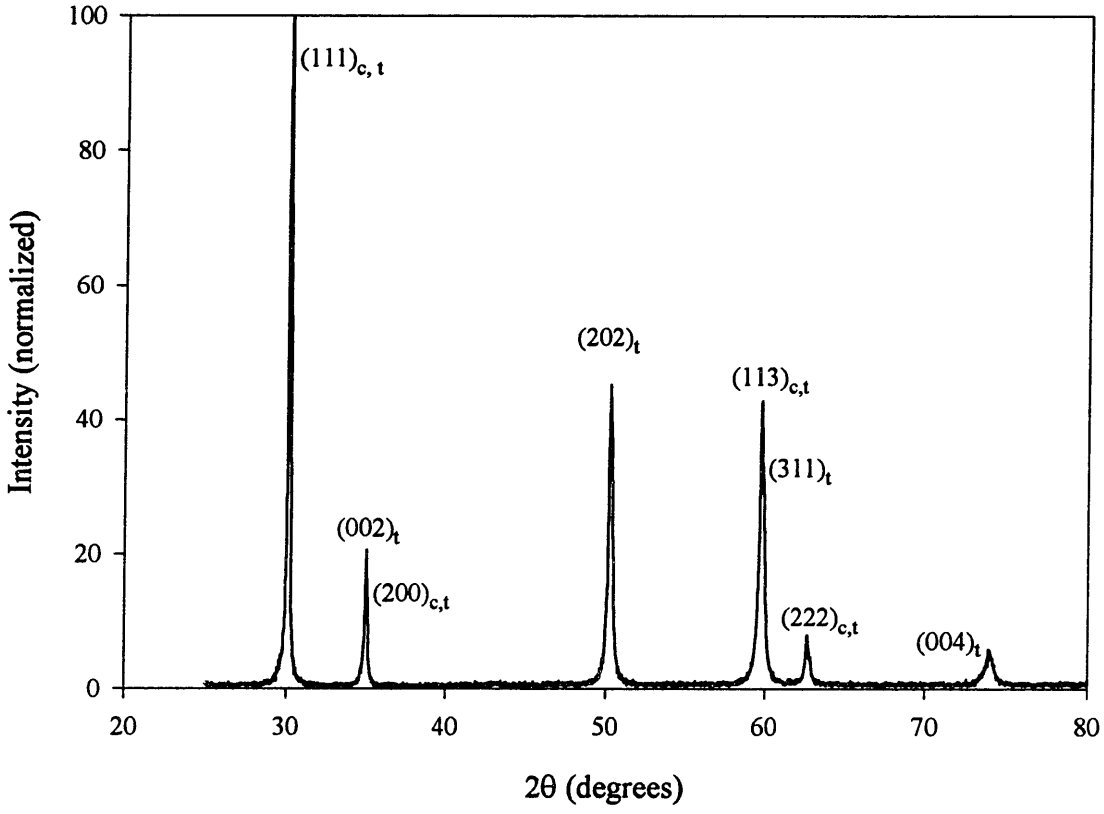


Figure 3-2: X-ray diffraction pattern for the YSZ electrolyte procured from Coors Ceramics Company.

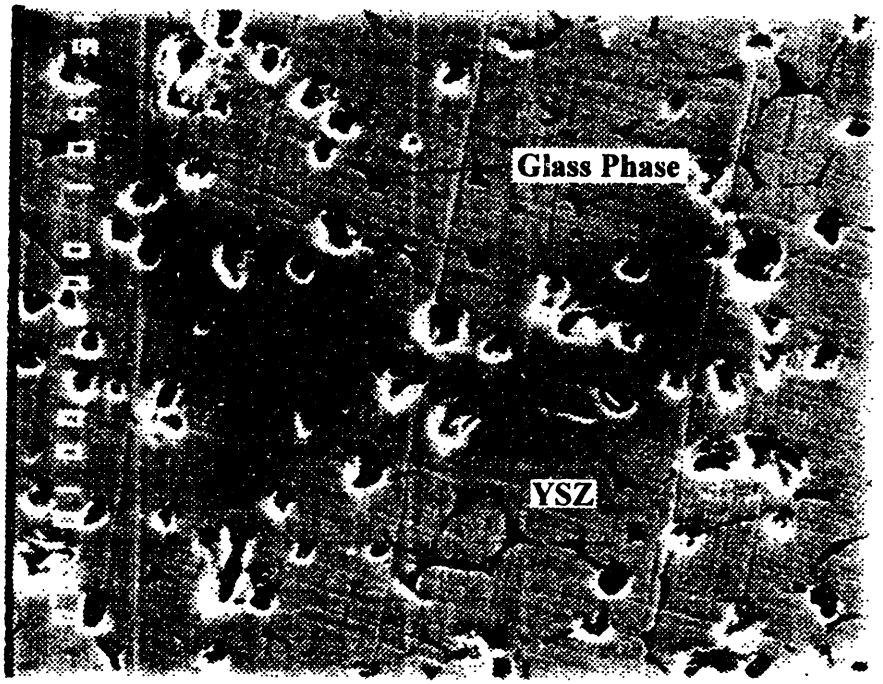


Figure 3-3: Scanning electron micrograph used for EPMA analysis of the electrolyte.

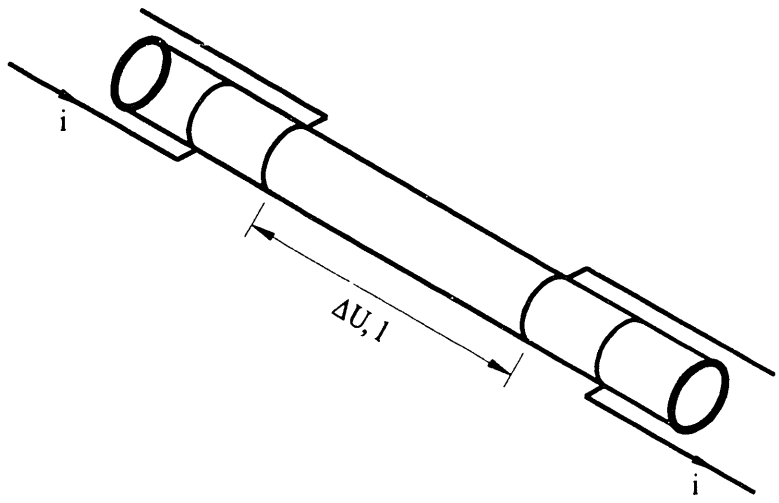


Figure 3-4: Principle of the four-point probe method.

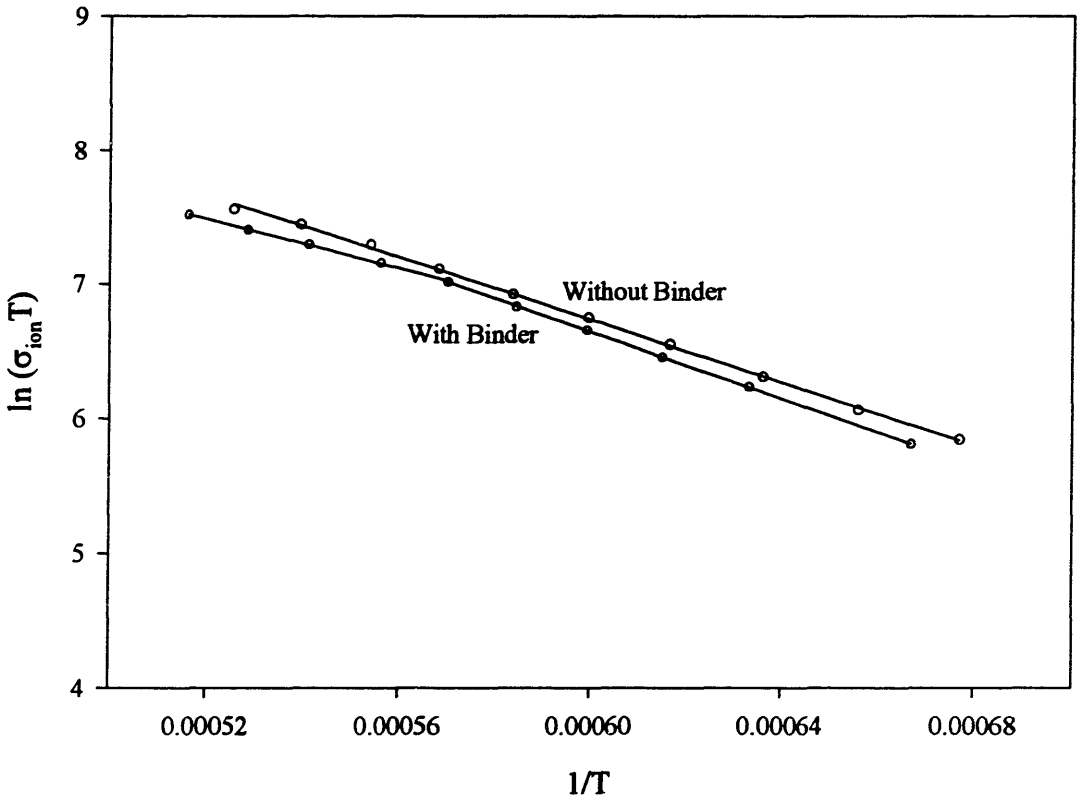


Figure 3-5: Variation of ionic conductivity with reciprocal absolute temperature.

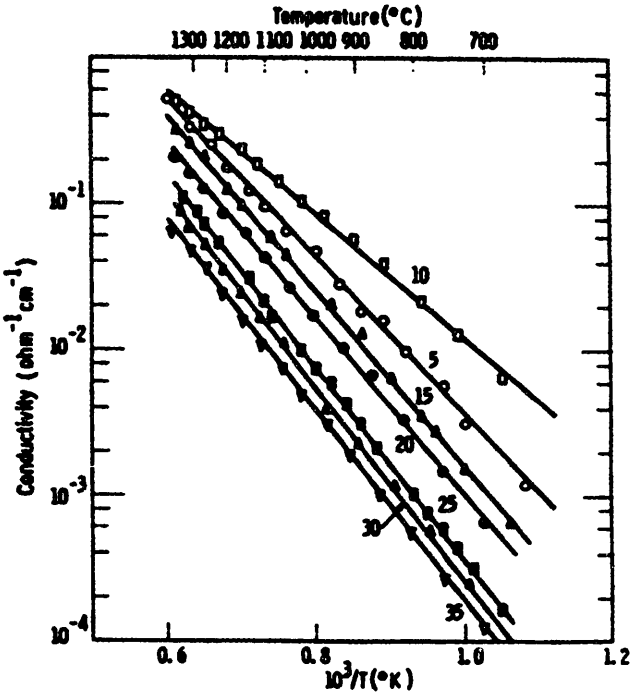


Figure 3-6: Conductivity vs. reciprocal temperature for various compositions in the system $Y_2O_3$-$ZrO_2$. Numbers near the curves denote mole-percent $Y_2O_3$.

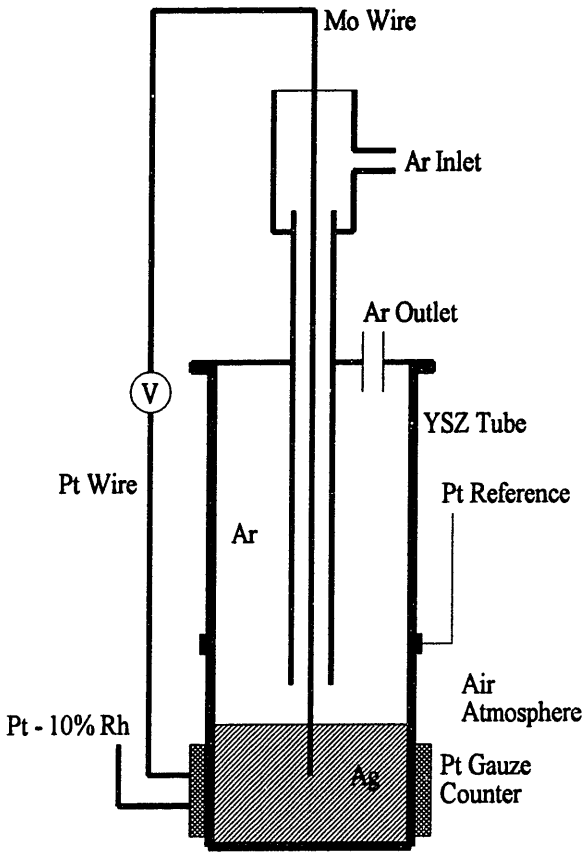


Figure 3-7: Cell geometry for electronic conductivity measurement.

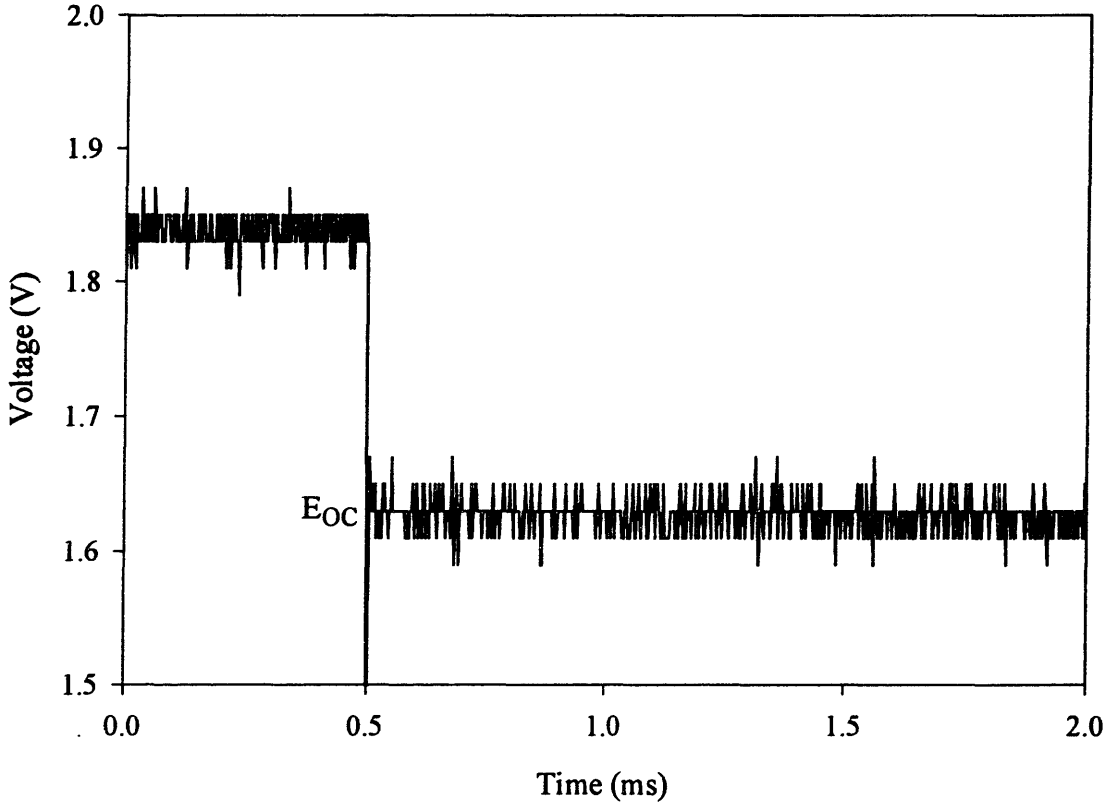


Figure 3-8: Typical cell-potential vs. time plot obtained during measurement of $E_{OC}$.

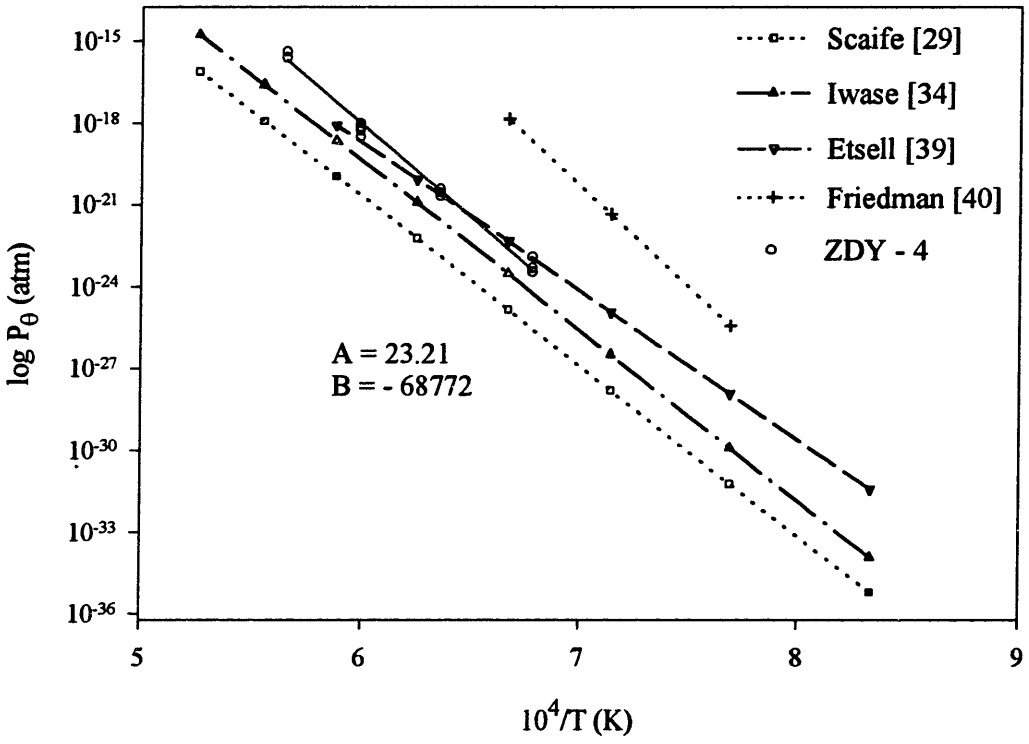


Figure 3-9: Relation between $P_\theta$ and 1/T for ZDY-4 tubes.

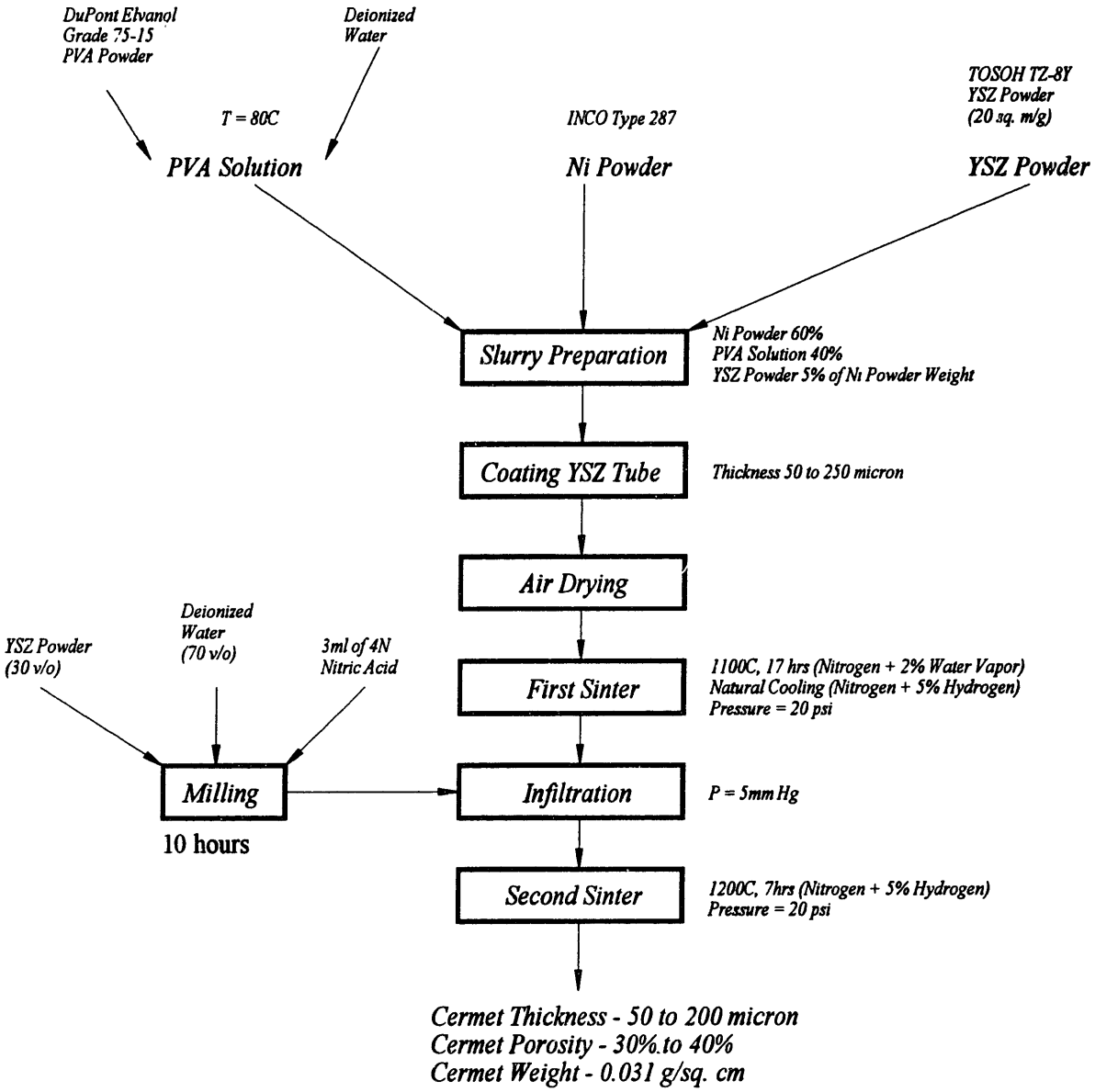


Figure 4-1: Flow chart for the cermet fabrication procedure described by Chou et. al. [12].

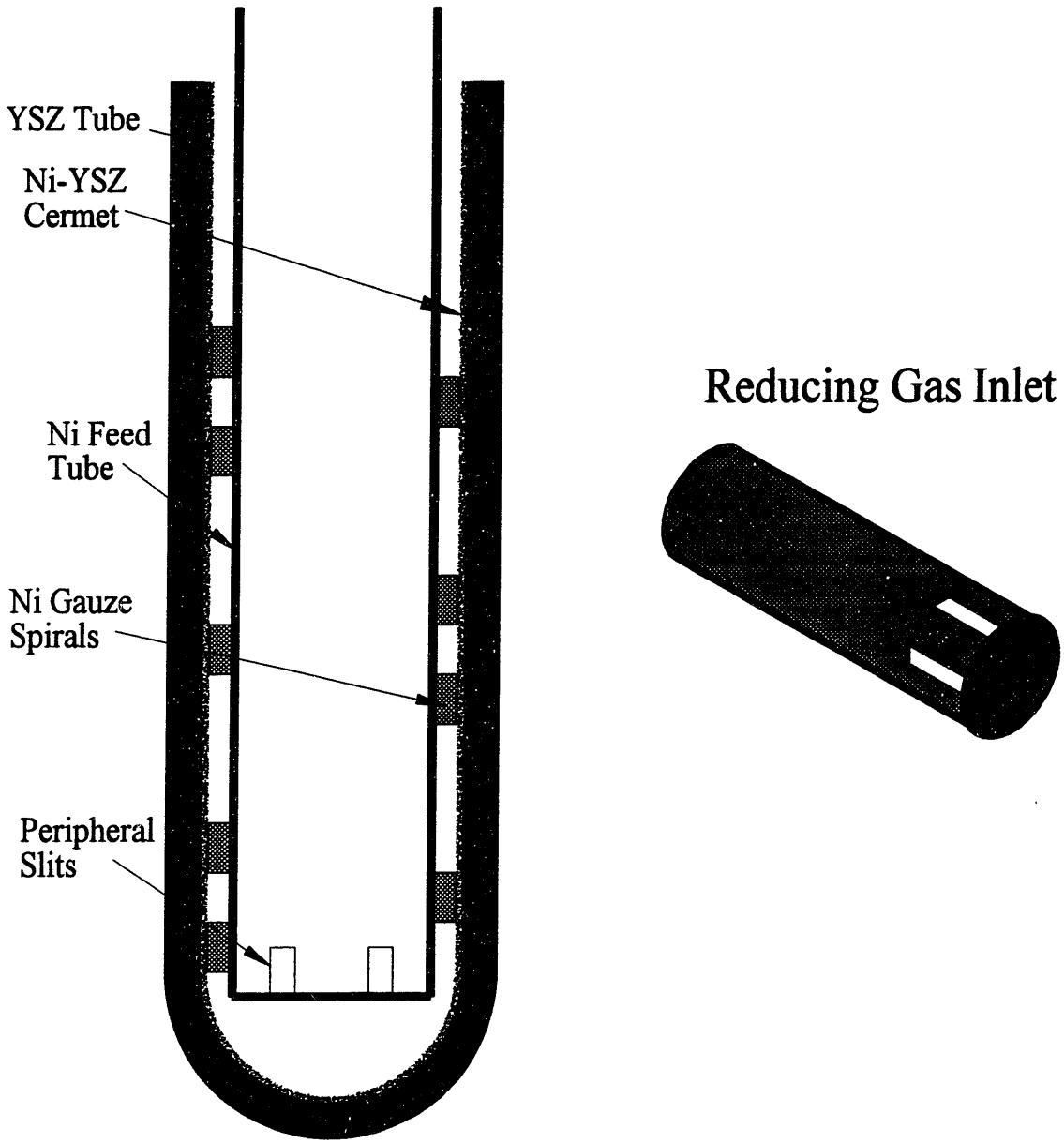


Figure 4-2: Assembled electrochemical deoxidation cell.

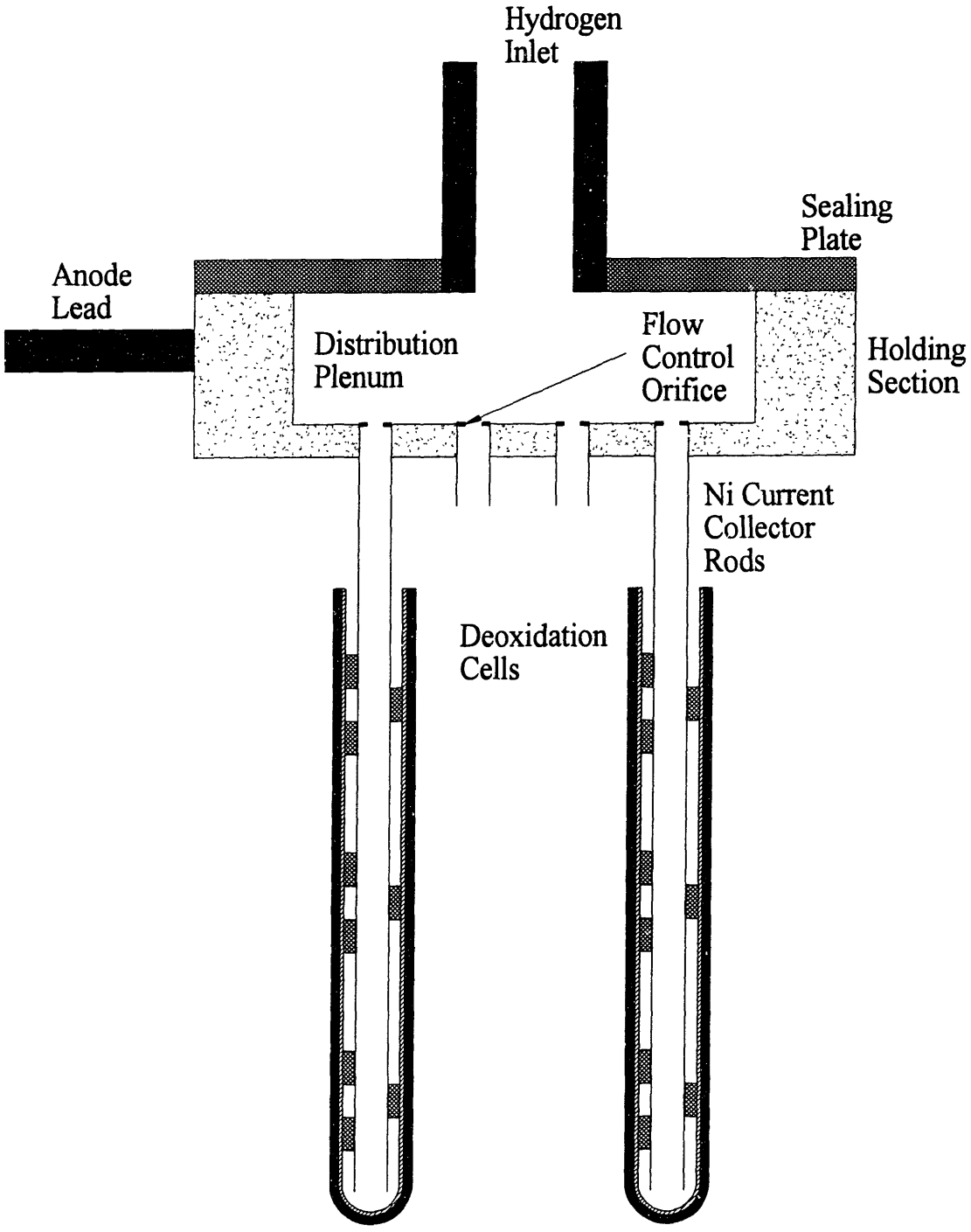


Figure 4-3: Schematic of the stainless steel fixture used for the pilot-scale trials at Reading Tube Corporation.

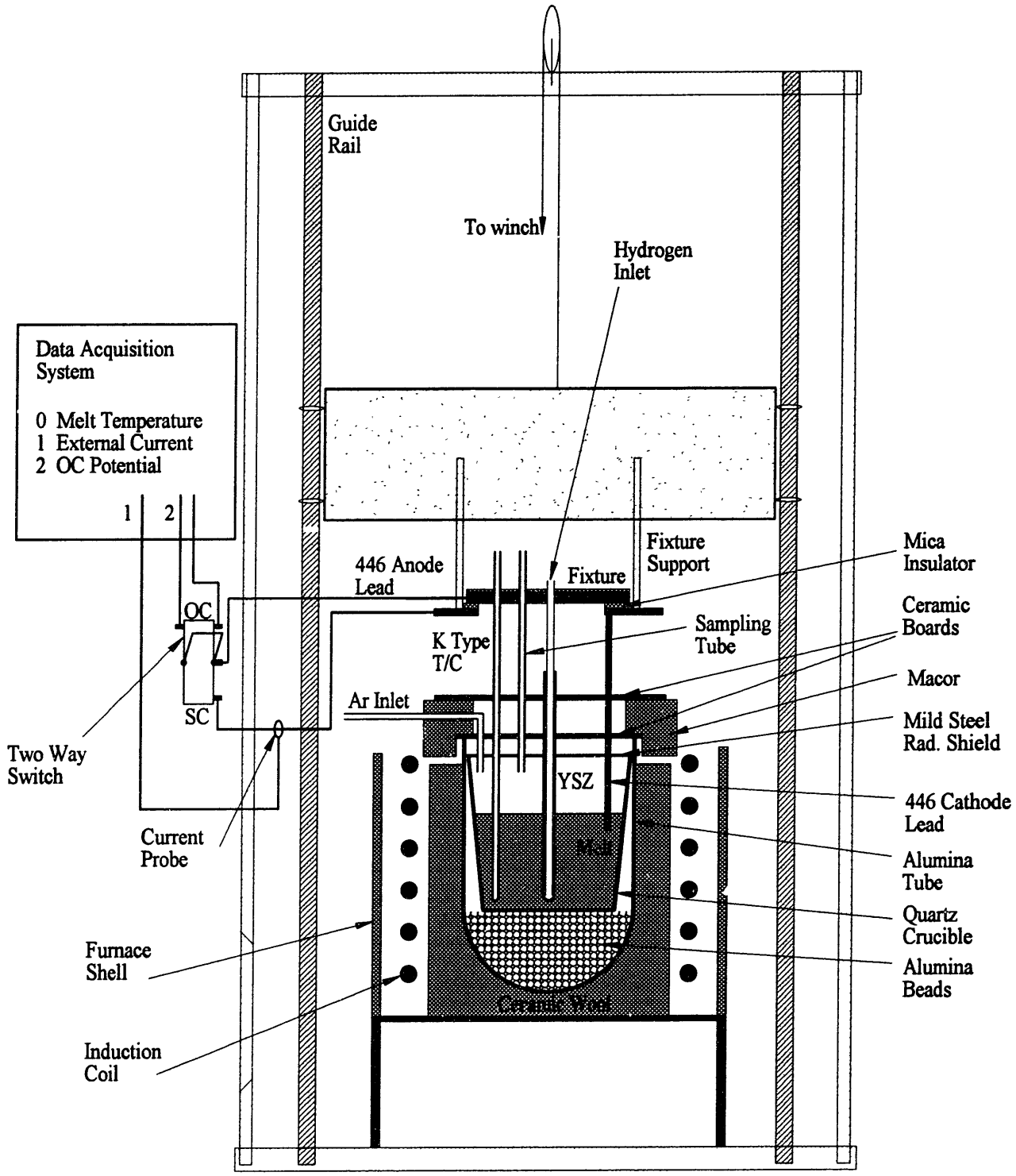


Figure 4-4: Experimental apparatus for laboratory deoxidation.

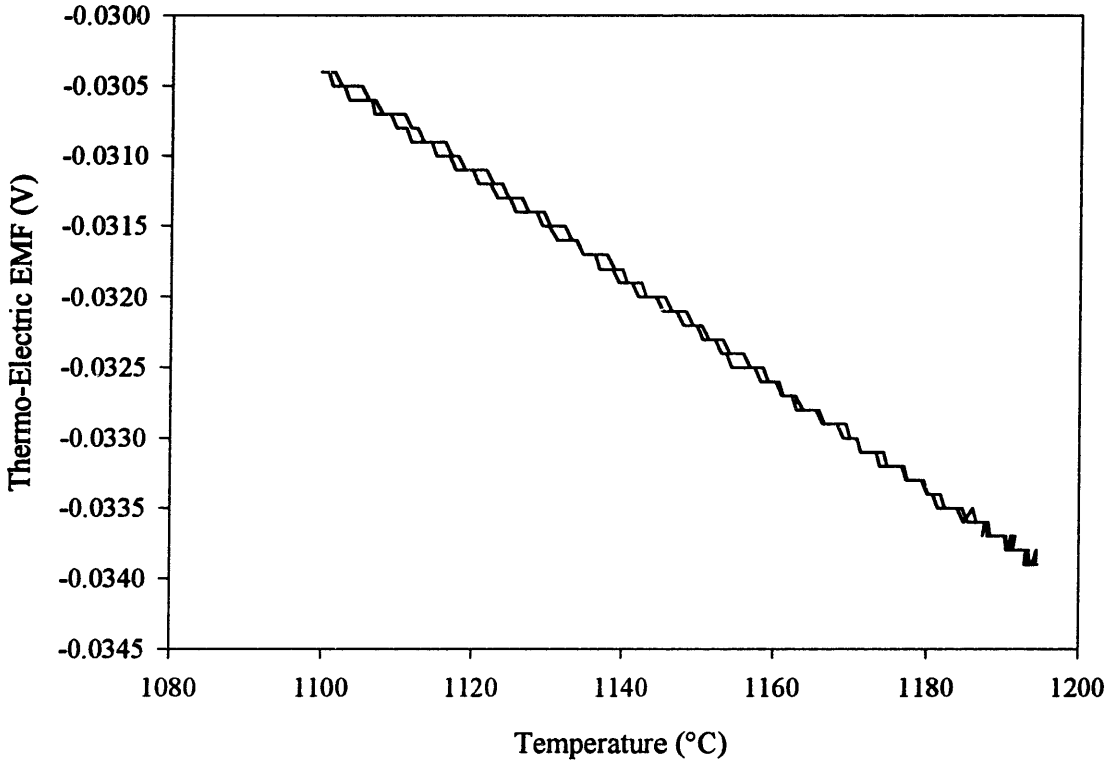


Figure 4-5: Thermoelectric characteristics of 446/Ni couple for the temperature range 1100-1200°C.

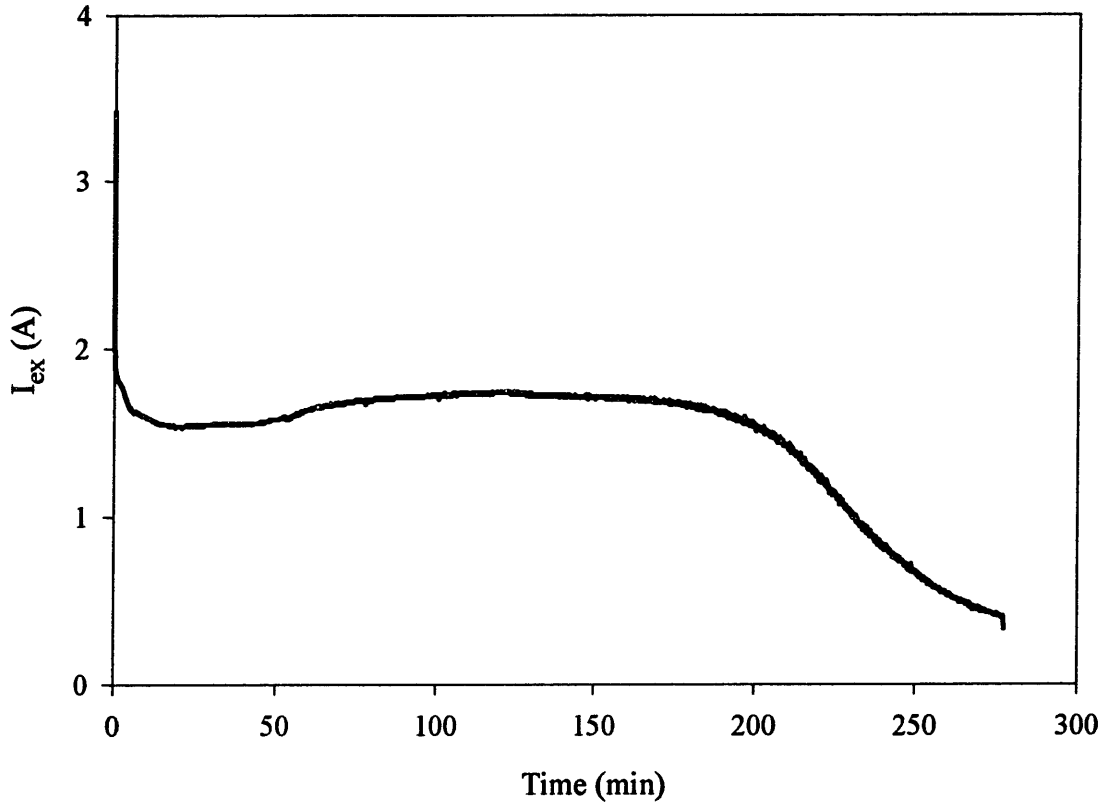


Figure 4-6: External current vs. time for a typical preliminary deoxidation experiment (expt. PRE).

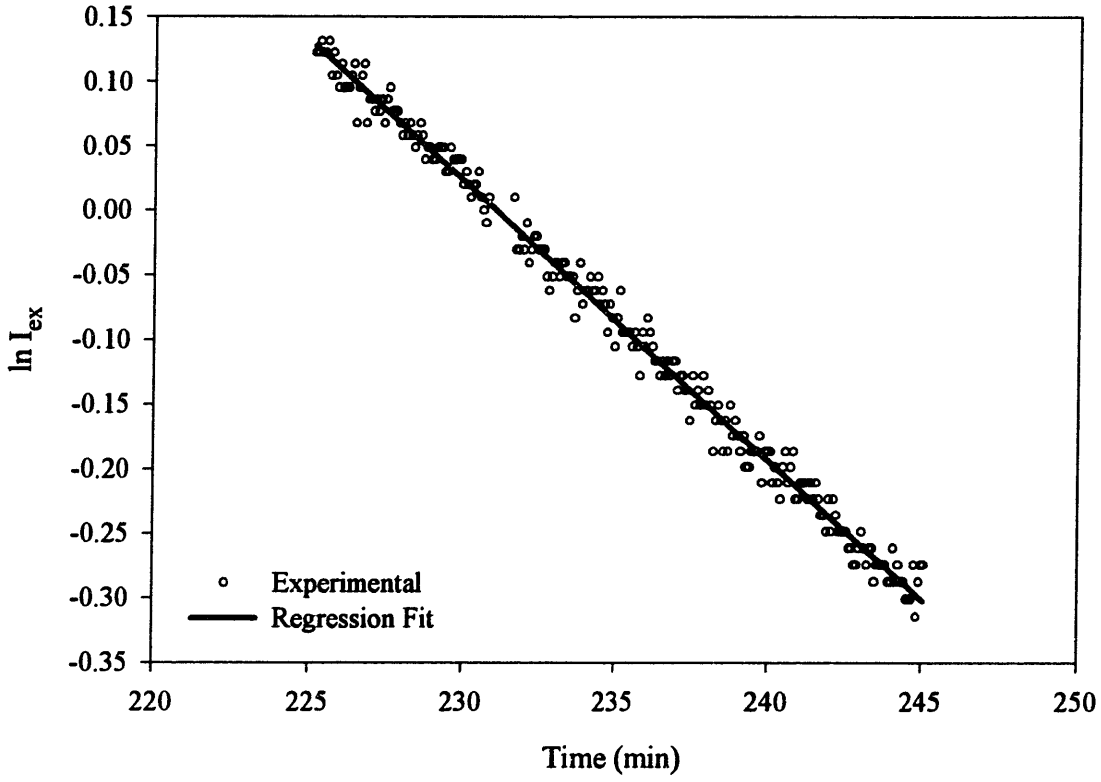


Figure 4-7: Calculation of the mass-transfer coefficient in Zone II (expt. PRE).

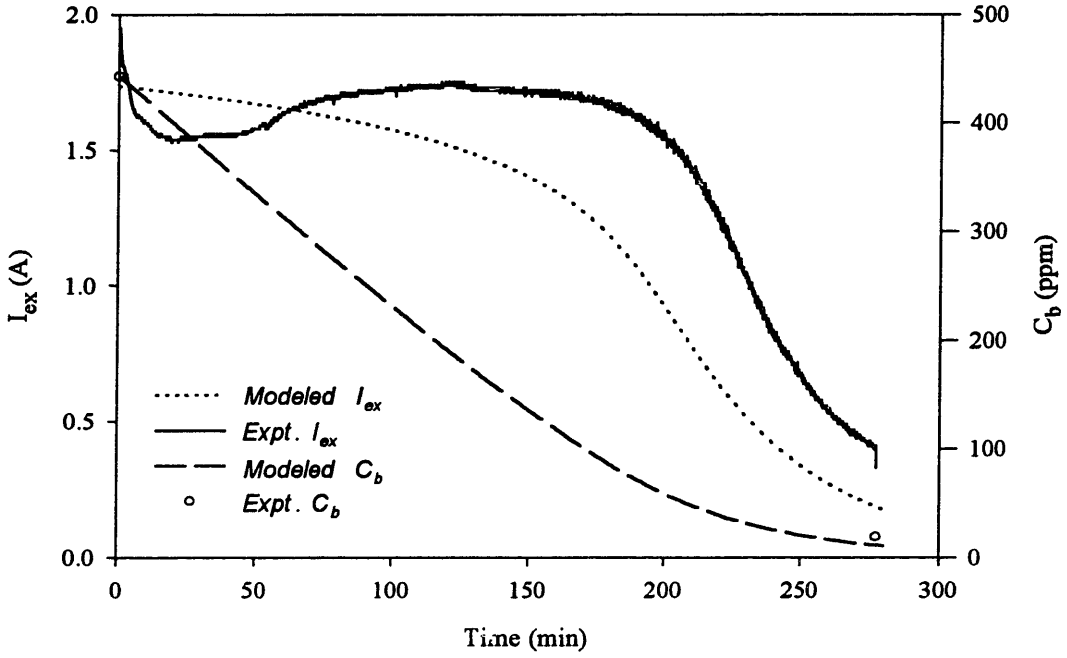


Figure 4-8: Experimental and modeled external current and bulk oxygen concentration vs. time (expt. PRE).

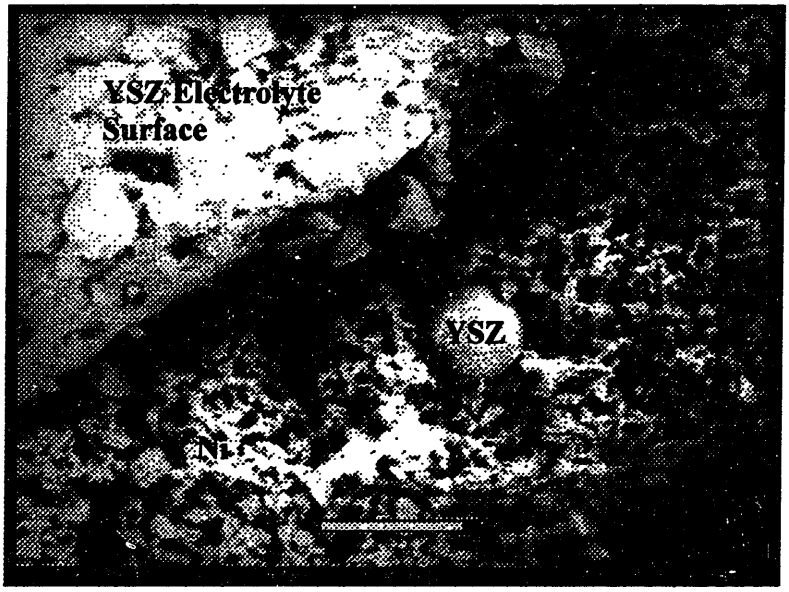


Figure 4-9: Scanning electron micrograph for a typical cermet prepared as in [12].

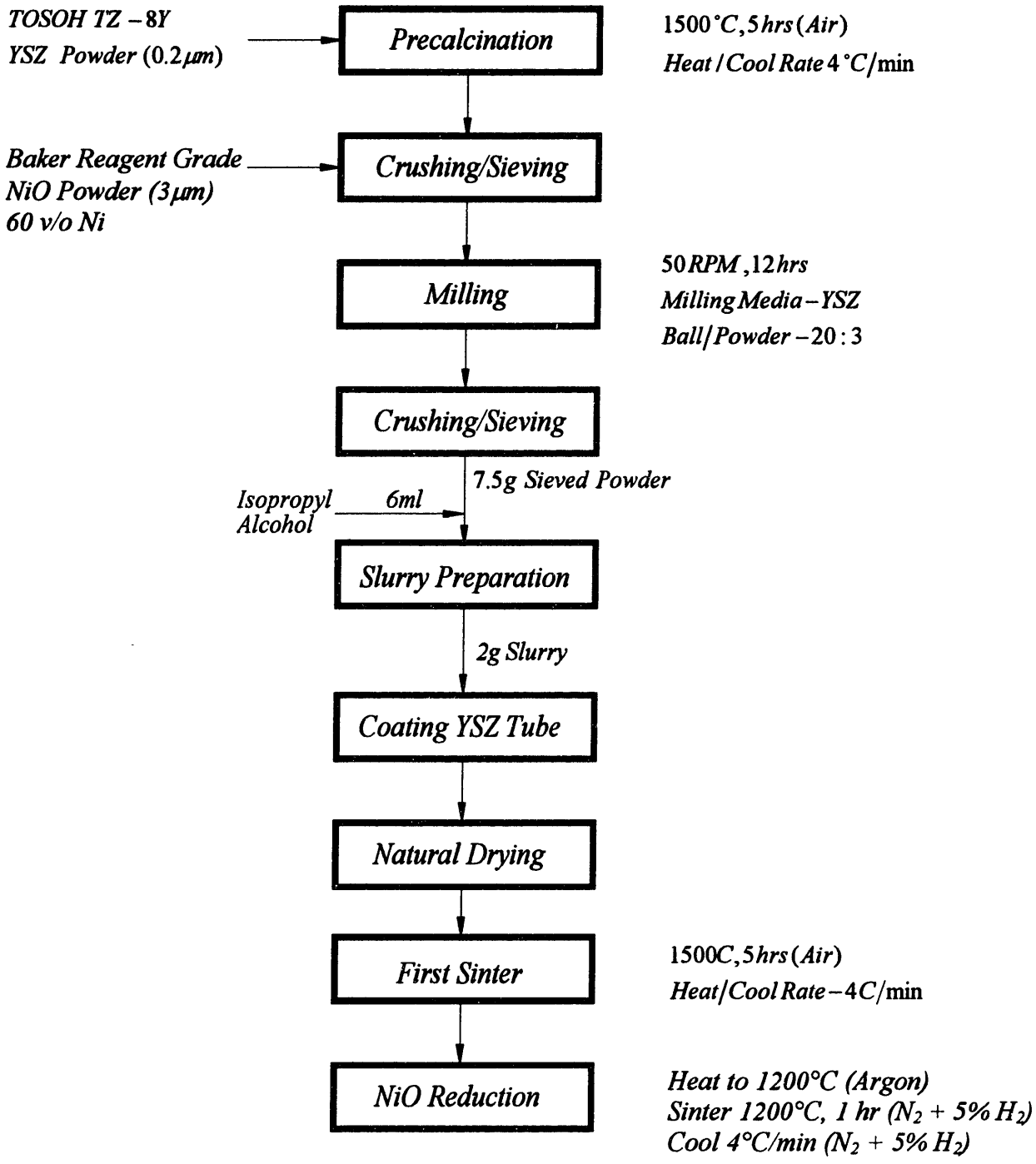


Figure 5-1: Flow chart for the modified cermet-fabrication process developed in the present study.

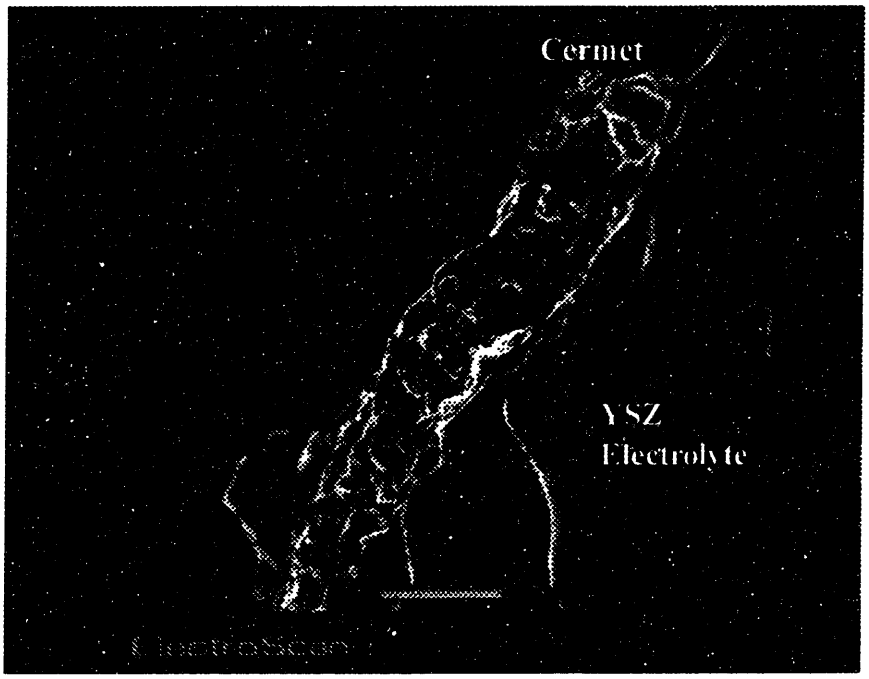


Figure 5-2: Scanning electron micrograph of the cermet/electrolyte interface showing uniform thickness.

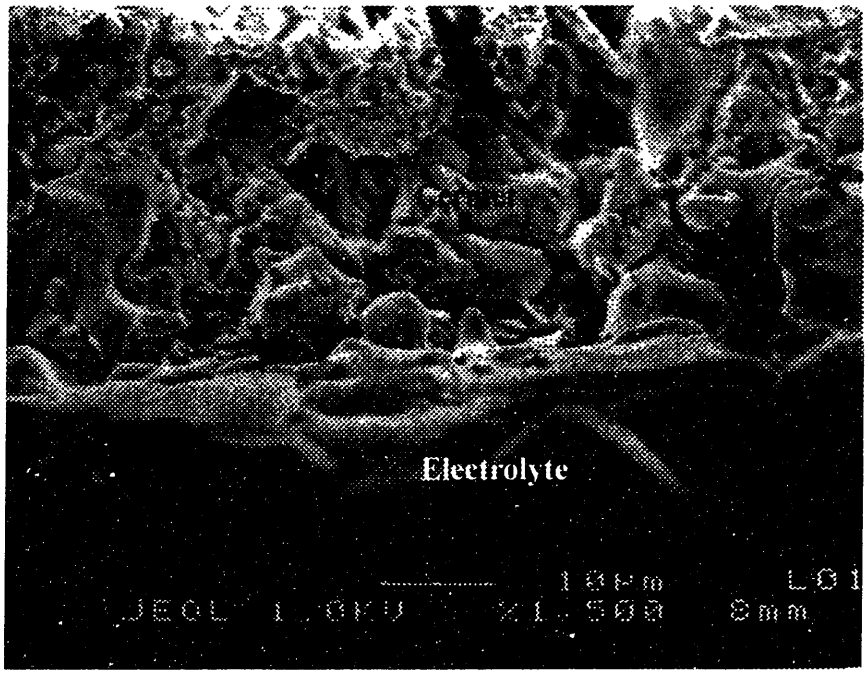


Figure 5-3: Scanning electron micrograph of the cermet/electrolyte interface showing electrolyte/electrode adhesion.

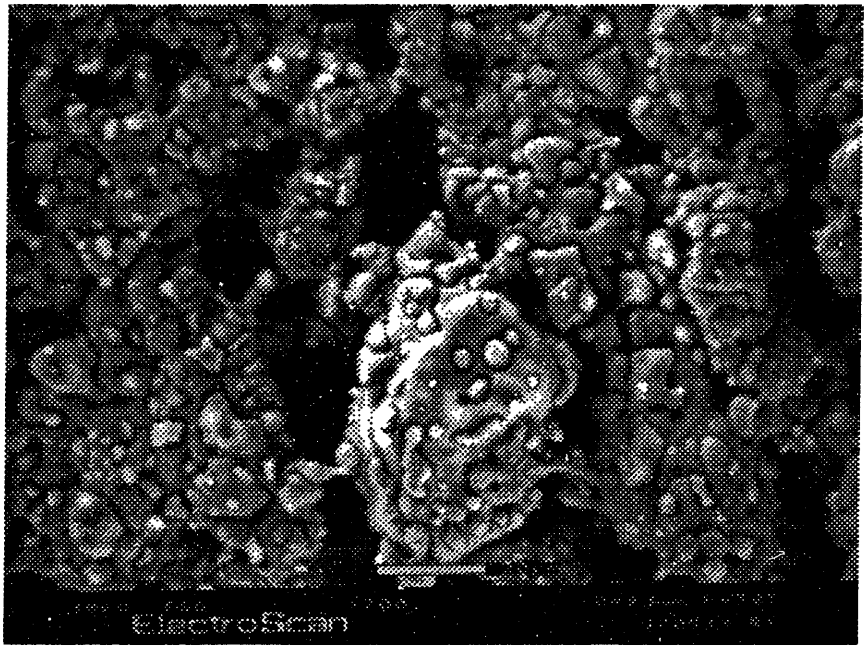

Figure 5-4: Scanning electron micrograph of the Ni/YSZ cermet surface.

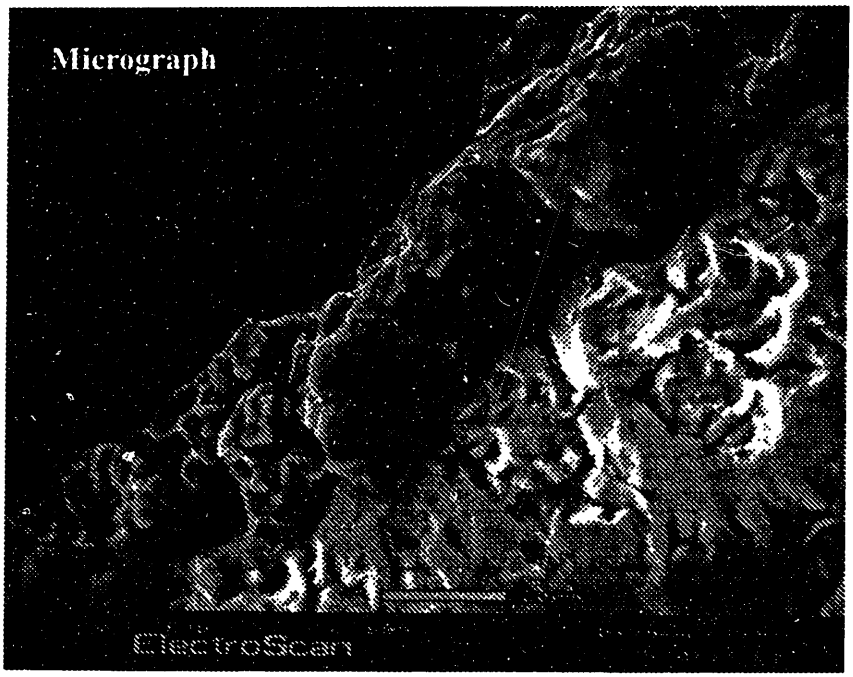


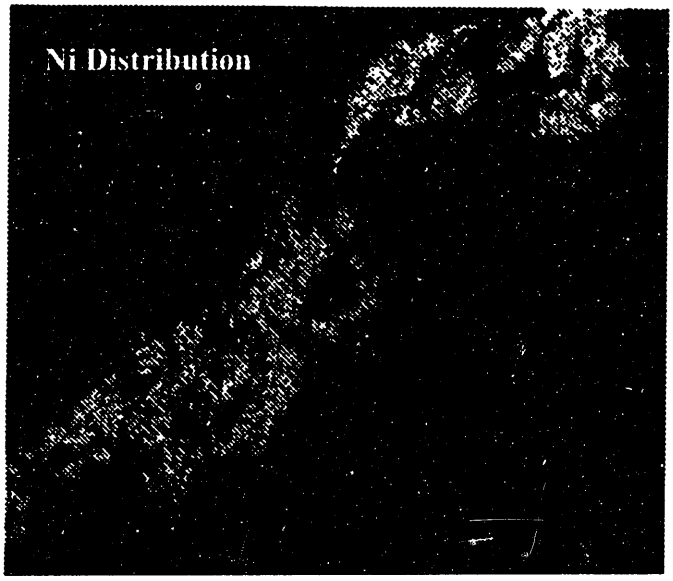


Figure 5-5: Ni distribution across the cermet thickness.

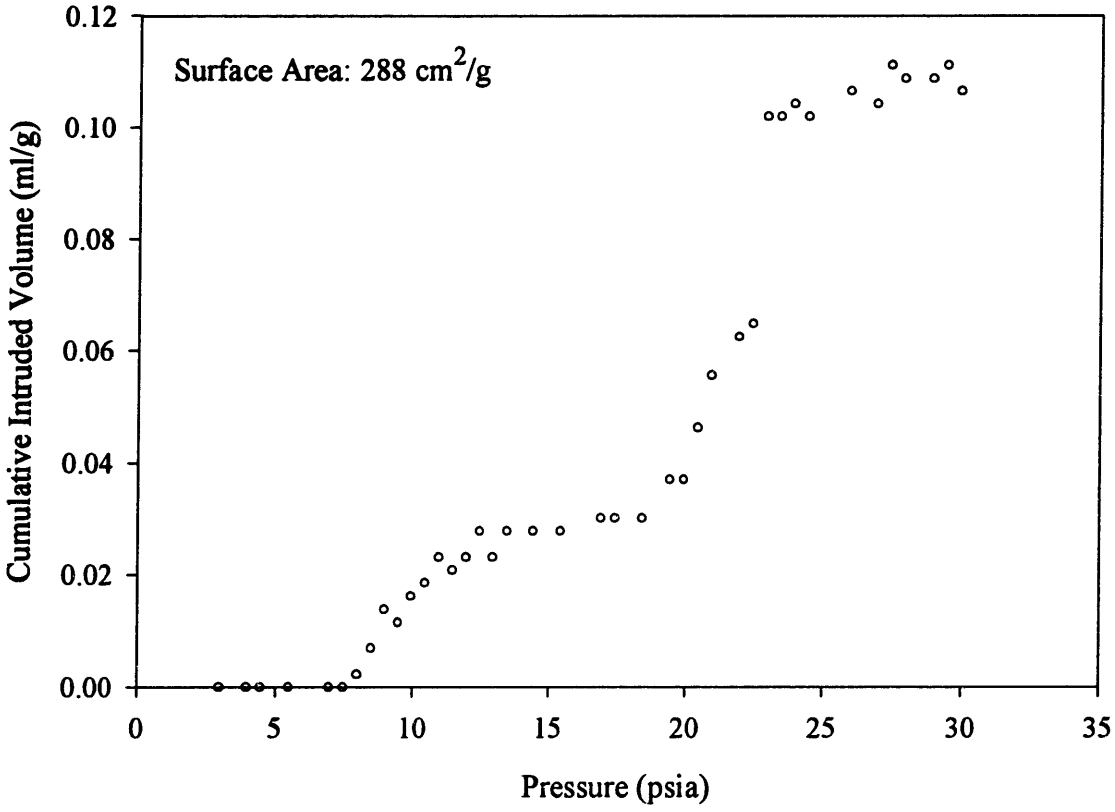


Figure 5-6: Cumulative pore-volume plot.

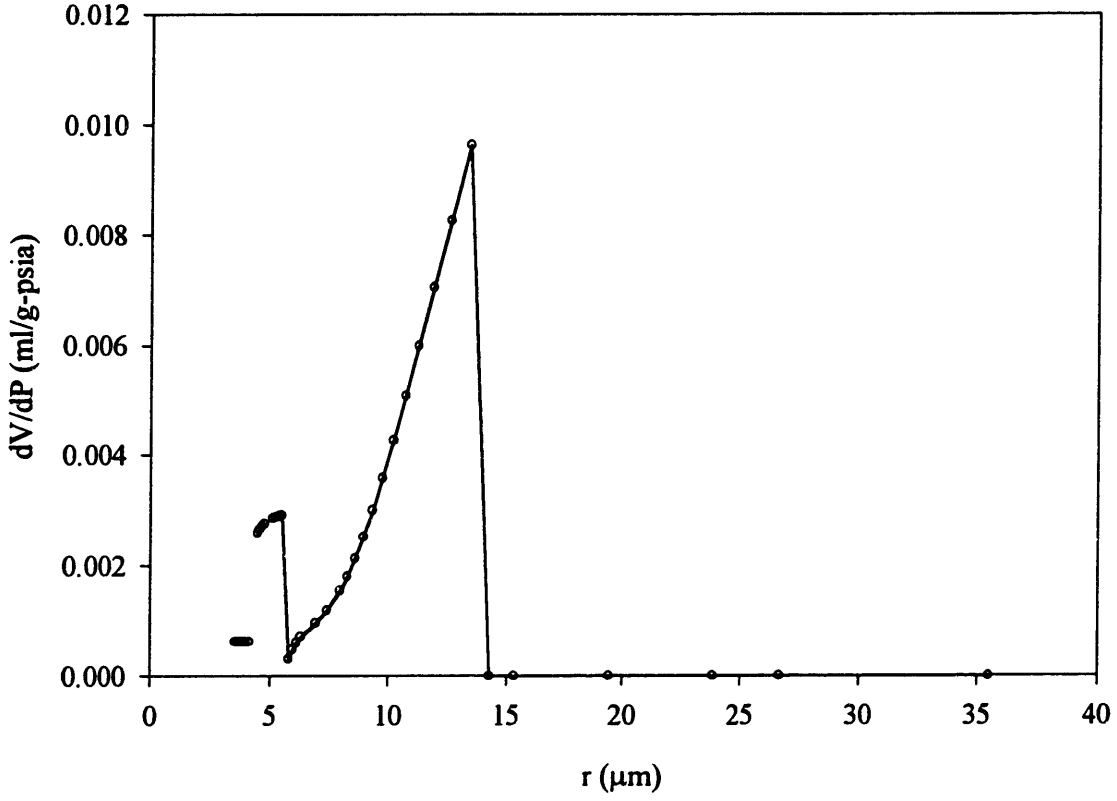


Figure 5-7: Derivative plot: $\frac{dV}{dP}$ vs. radius.

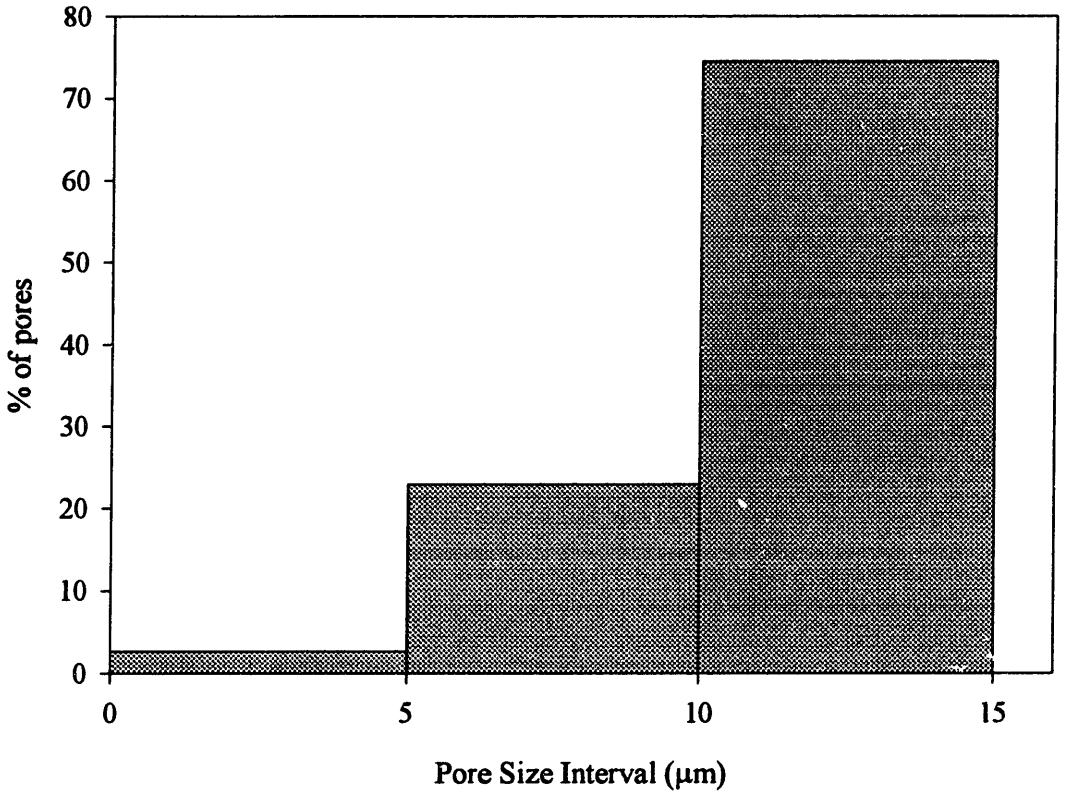


Figure 5-8: Pore-size distribution.

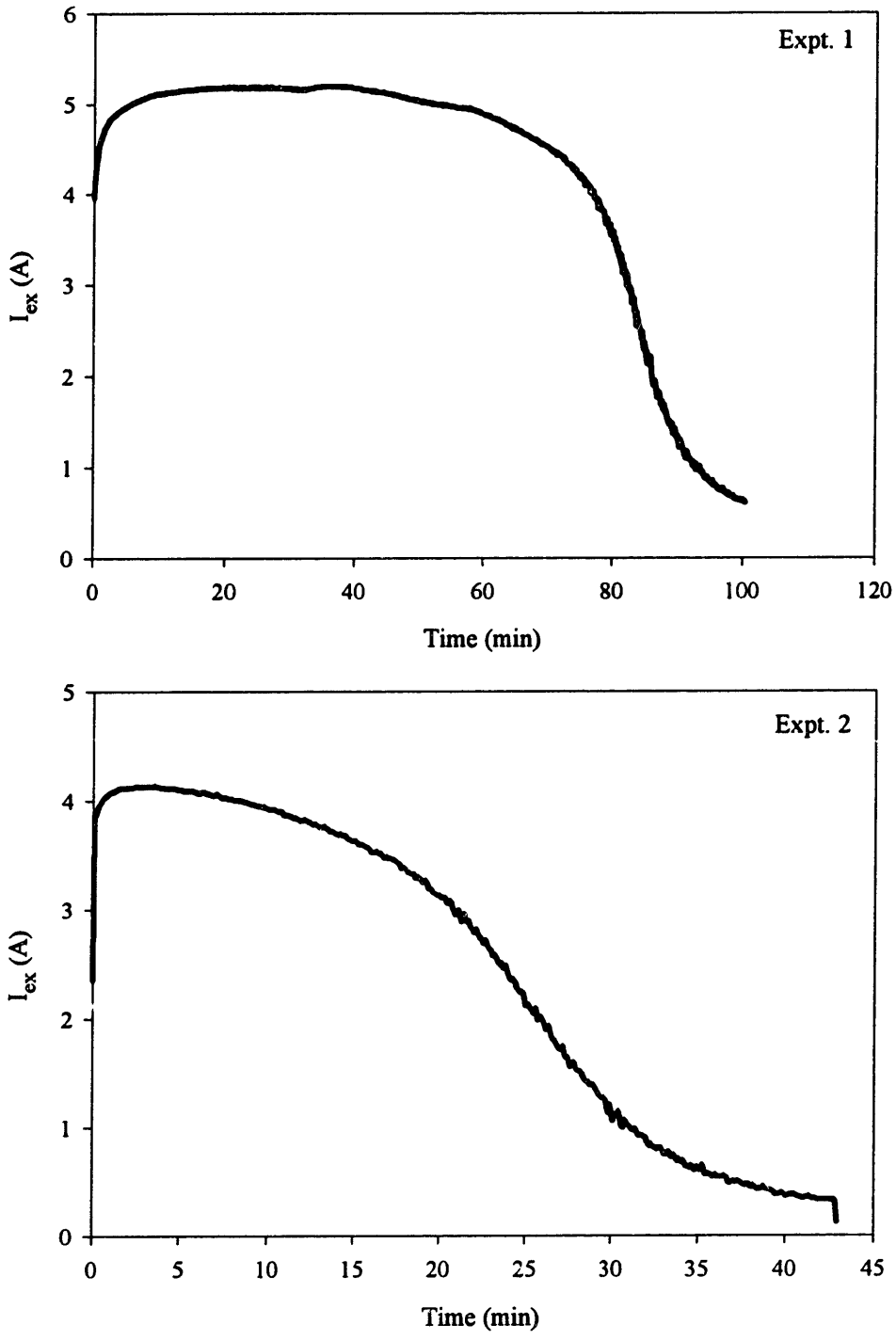


Figure 5-9: Experimental external current vs. time.

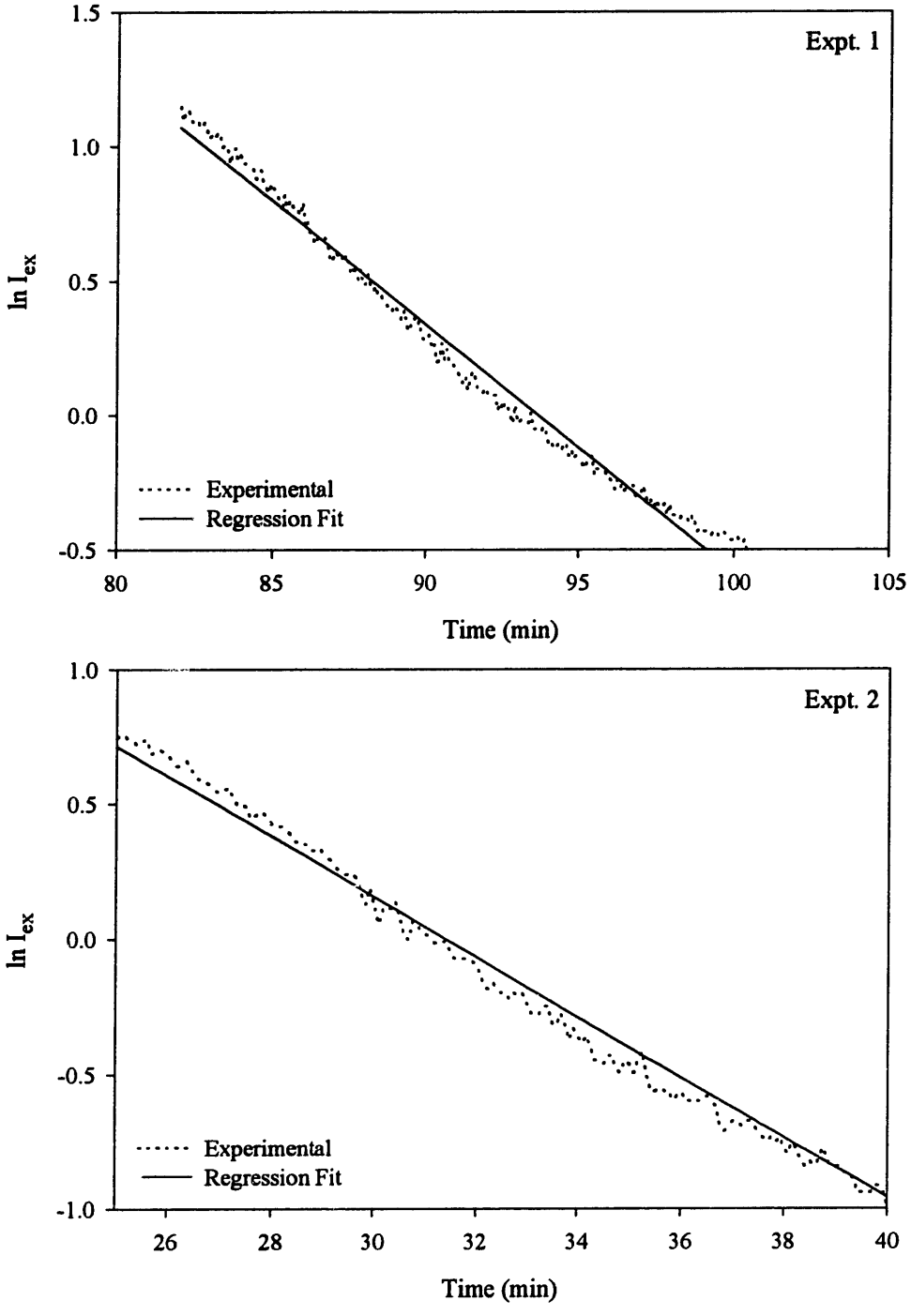


Figure 5-10: Linear regression between $\ln I_{ex}$ and time.

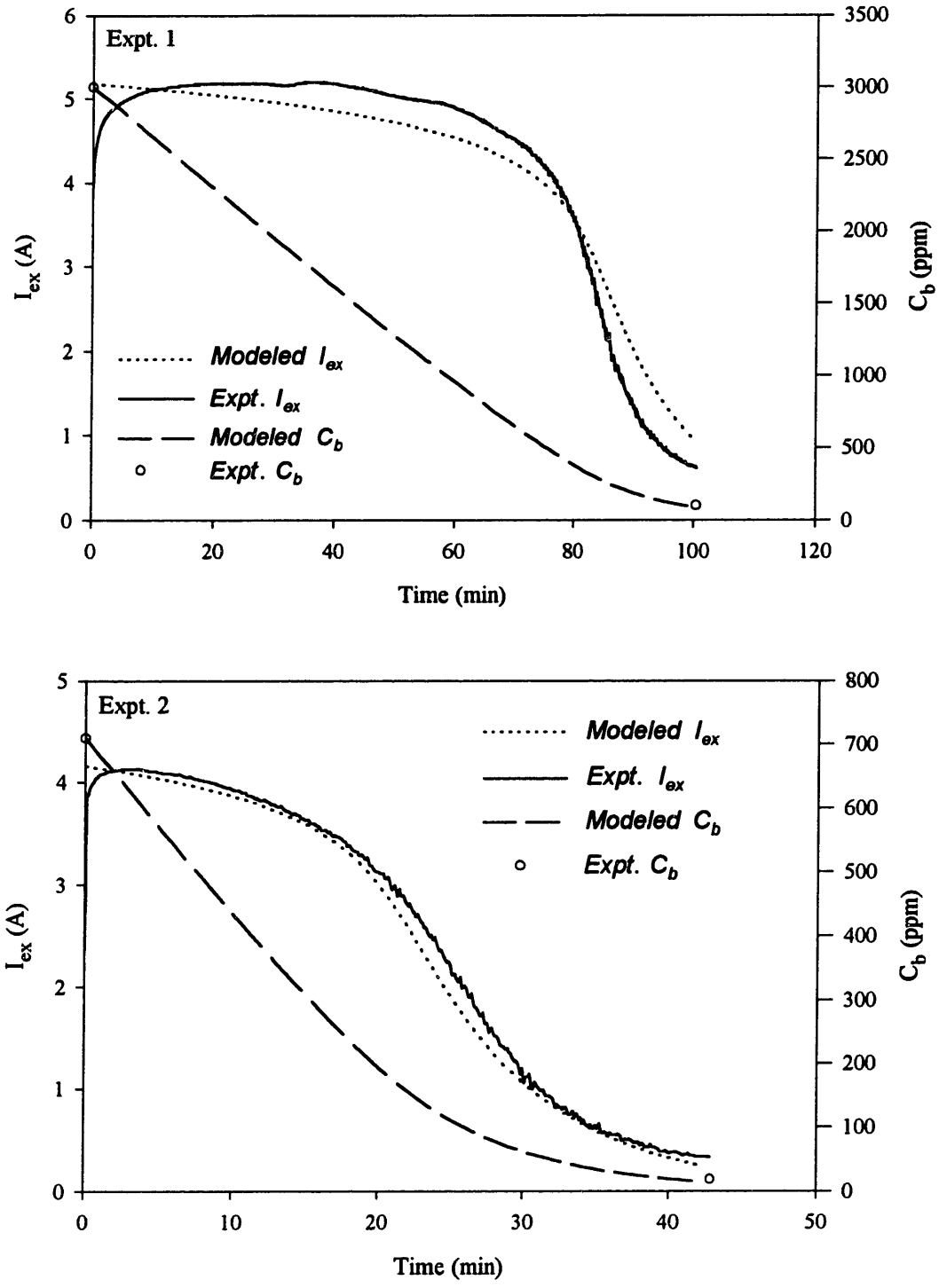


Figure 5-11: Modeled/experimental external current and concentration vs. time curves.

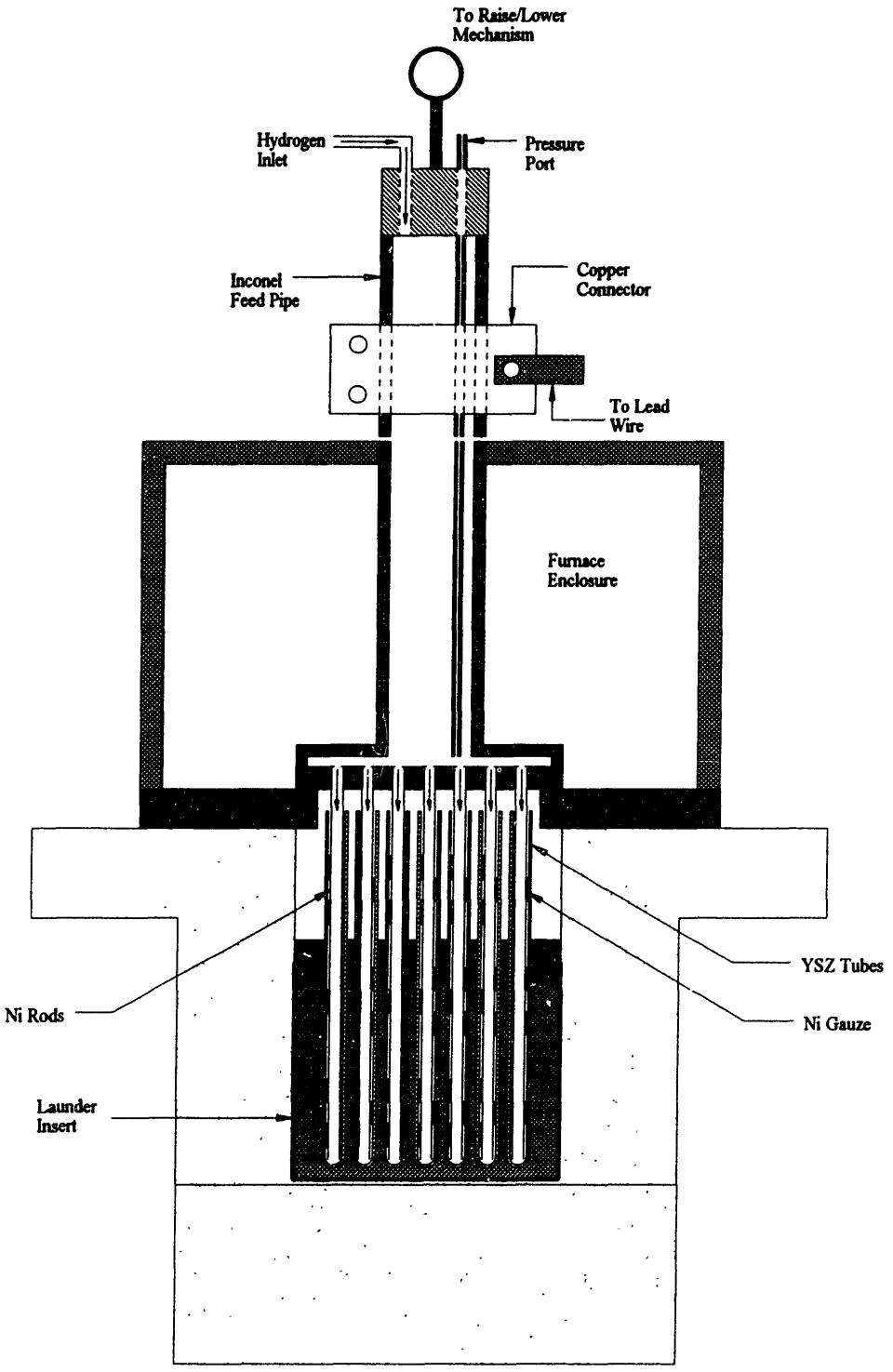


Figure 6-1: Launder insert (end view): deoxidation setup at Reading Tube Corporation.

Reverberatory Melting Furnace

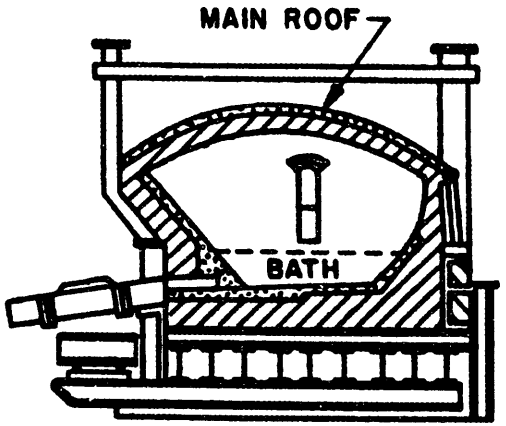


10 x 25 ft

| | | |
|---|---|---|
| Melting | 3 hrs | 200t |
| Wood Poling | 1.5 hrs | 200t |
| Tapping | 10 hrs | 20 tph |

Launder

60 ft

Transport of Copper
On-Line Deoxidation (Phos Cu Addition)
10 hrs/ 20 tph

Holding Furnace
(Adjusts Flow Rate)

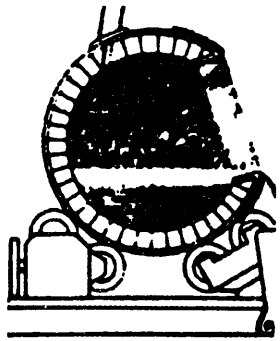

Metering and Casting

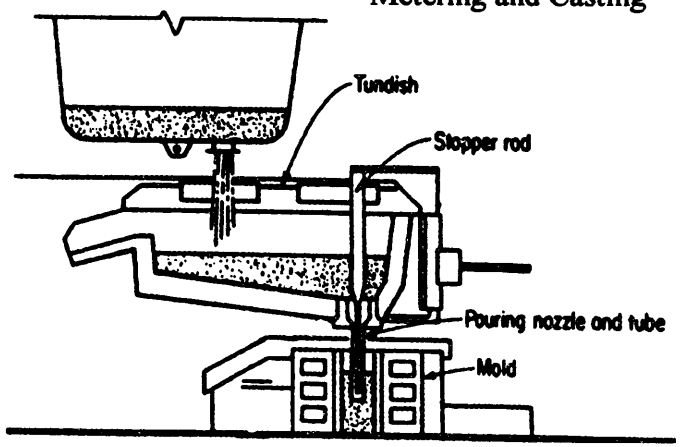


Figure 6-2: Flowsheet for copper production at RTC.

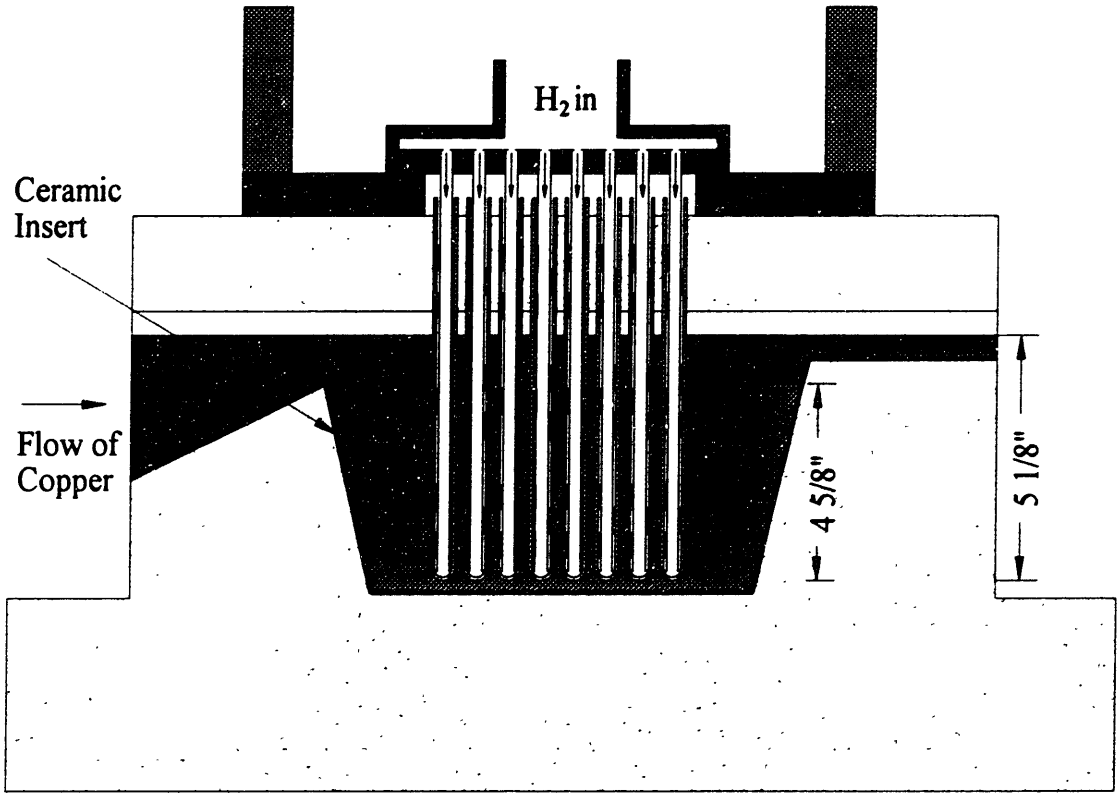


Figure 6-3: Launder insert (side view): deoxidation setup at Reading Tube Corporation.

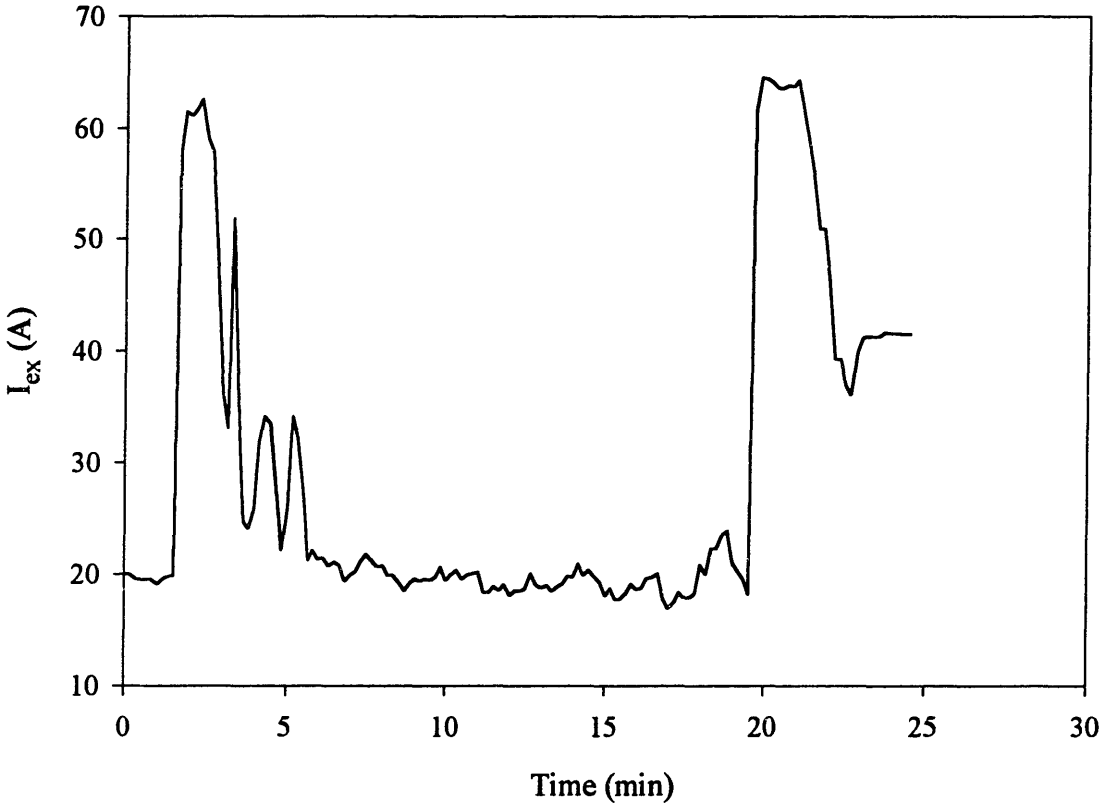


Figure 6-4: External current: plant trial at Reading Tube Corporation.

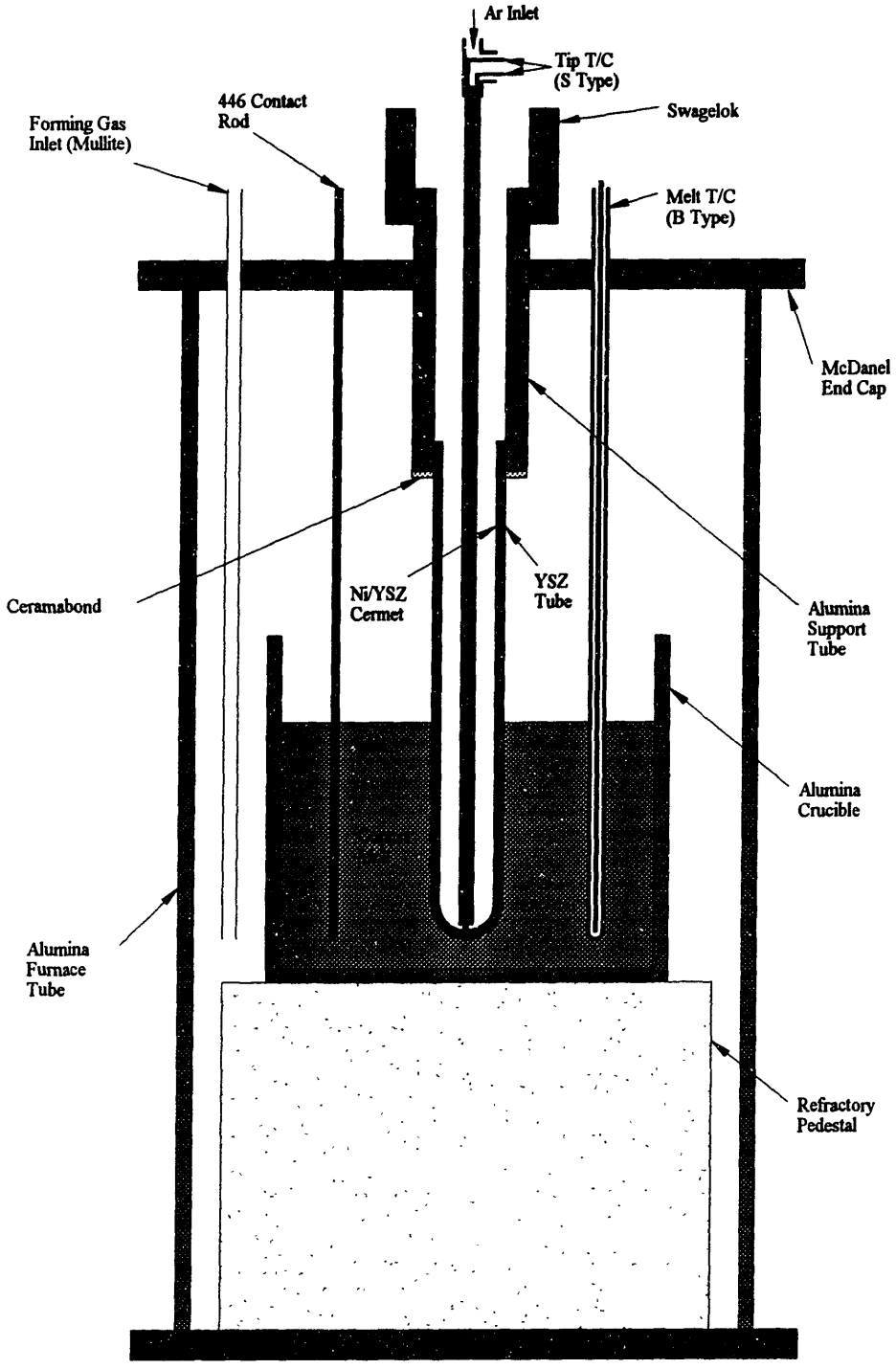


Figure 6-5: Experimental arrangement for thermal cycling.

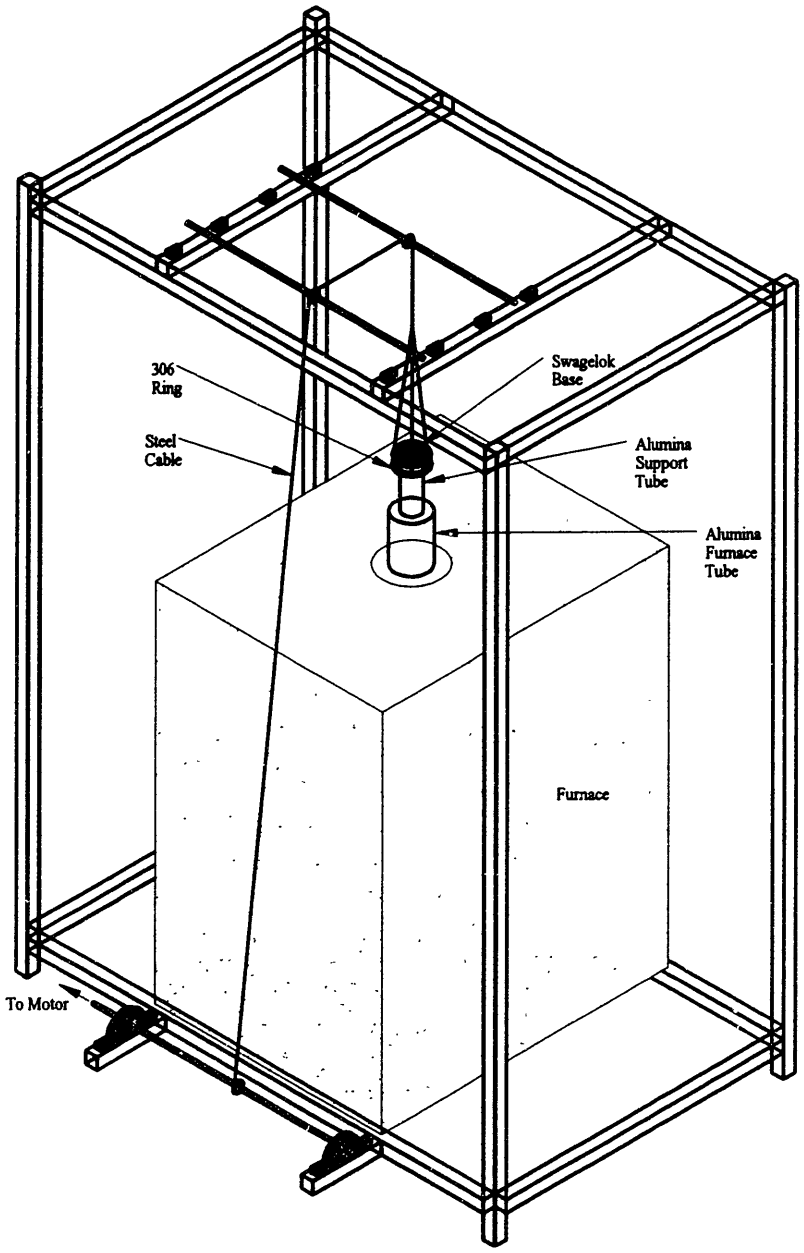


Figure 6-6: Longevity/cycling setup: isometric view.

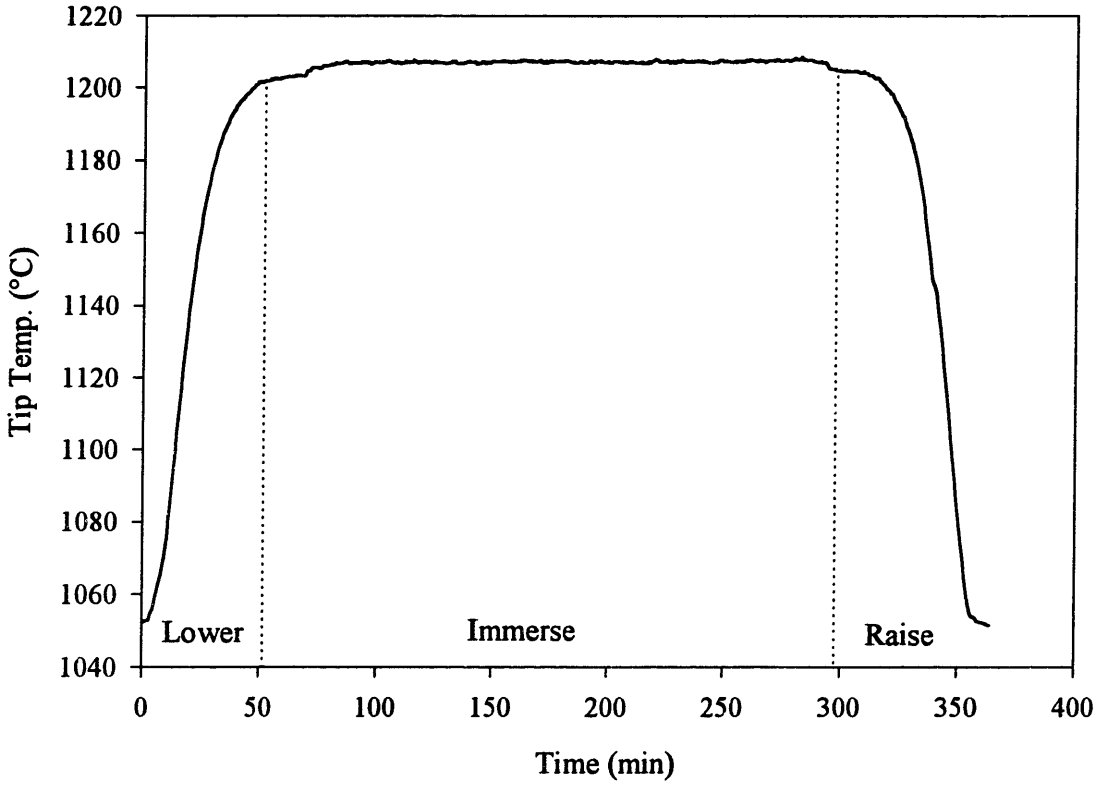


Figure 6-7: Typical temperature history during a thermal cycle.

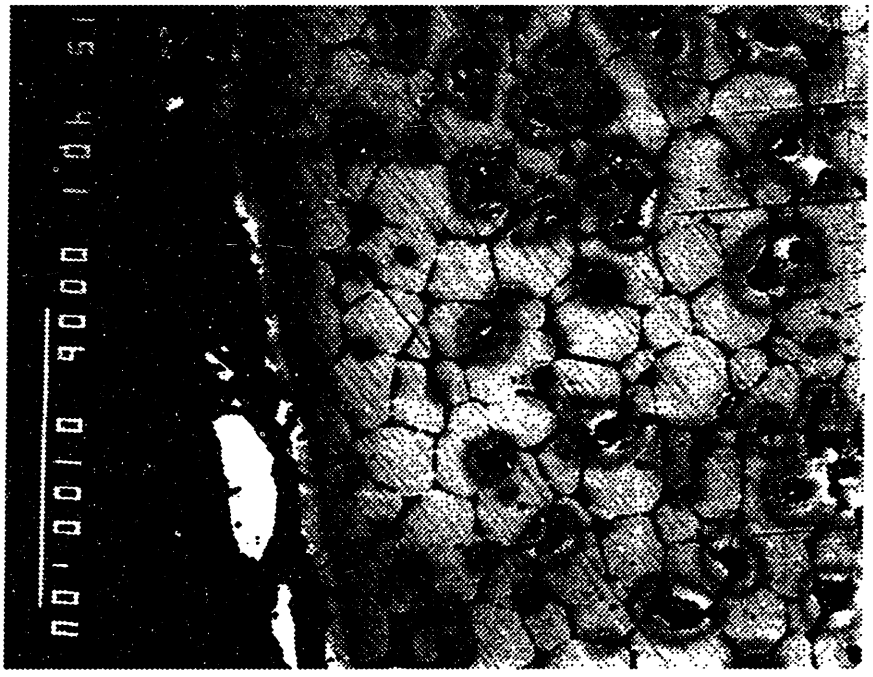

Figure 6-8: Scanning electron micrograph of the electrolyte surface after Expt. CE2.

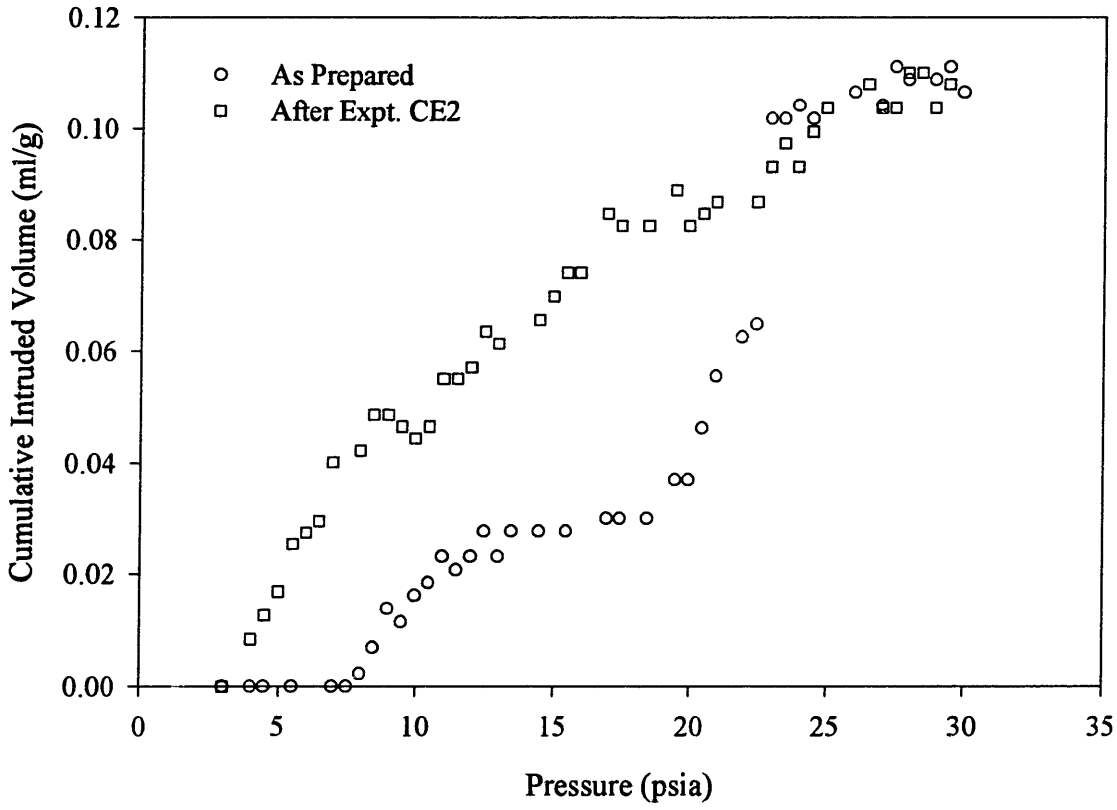


Figure 6-9: Intrusion curves for Ni-YSZ cermet anodes as a function of time at temperature.

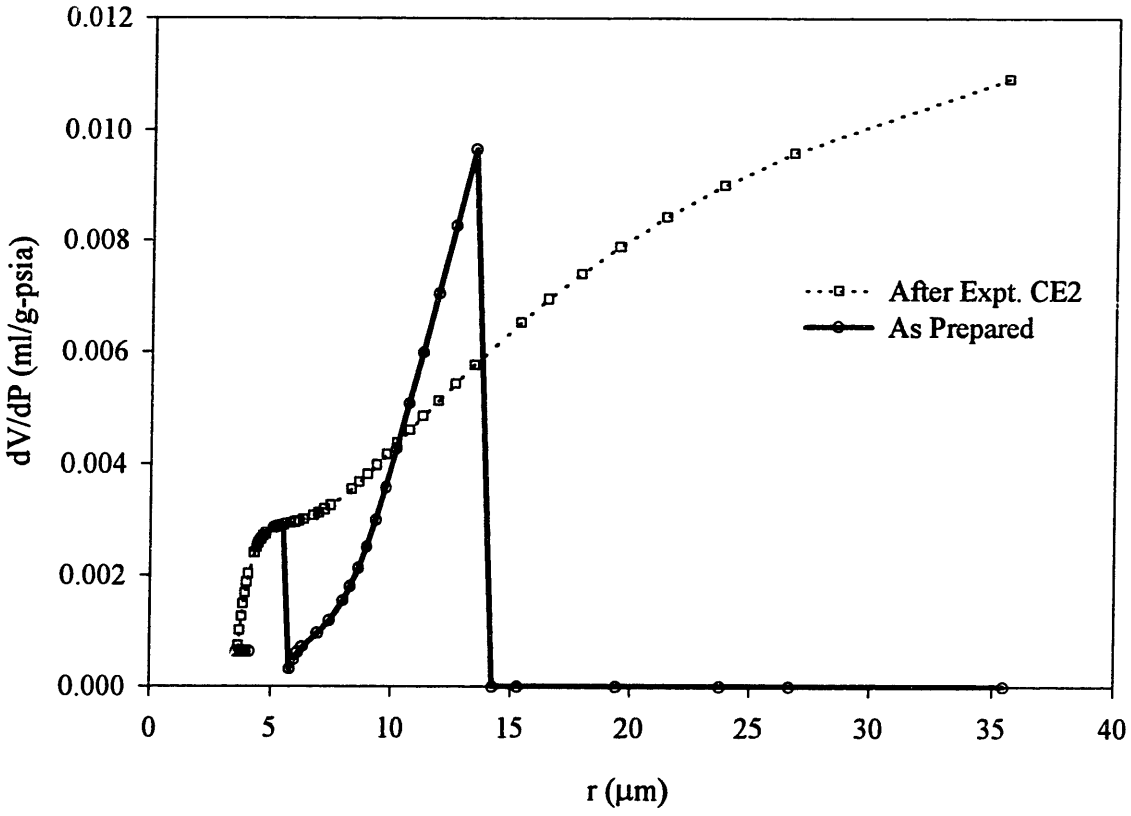


Figure 6-10: Pore-radius distributions for Ni-YSZ cermet anodes as a function of time at temperature.

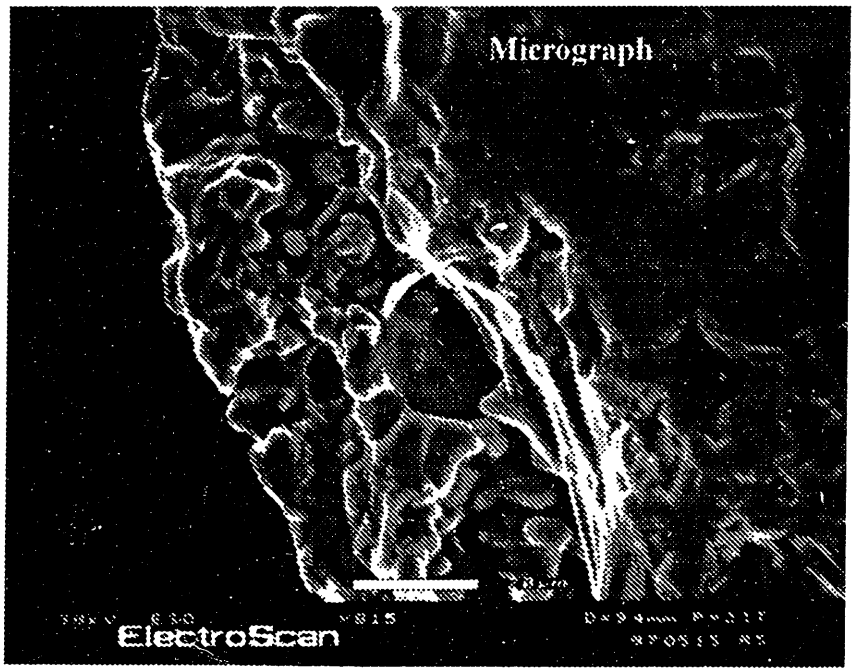


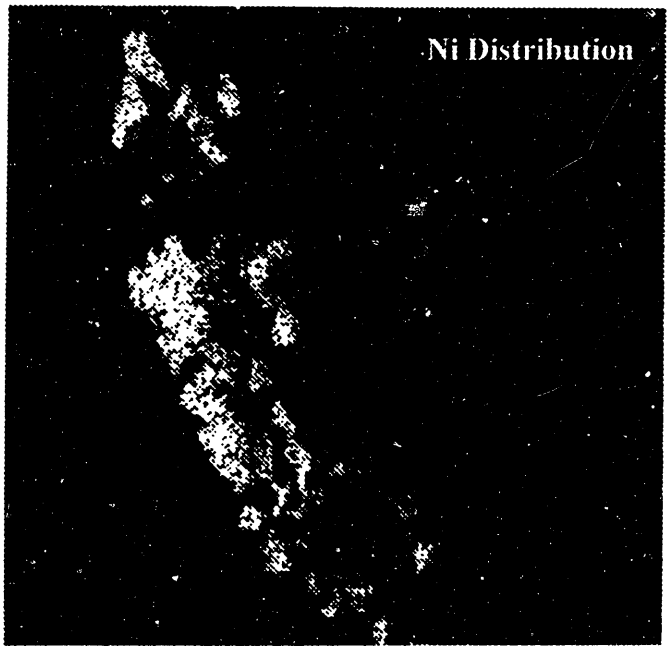


Figure 6-11: Scanning electron micrograph and Ni distribution across the cross-section of Ni-YSZ cermet electrodes after expt. CE2.

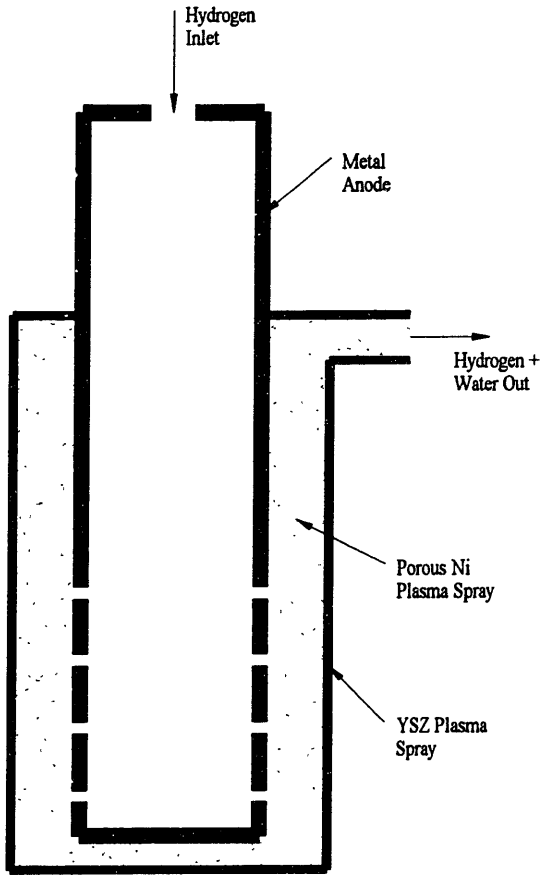


Figure 6-12: INEEL solid-electrolyte cell.

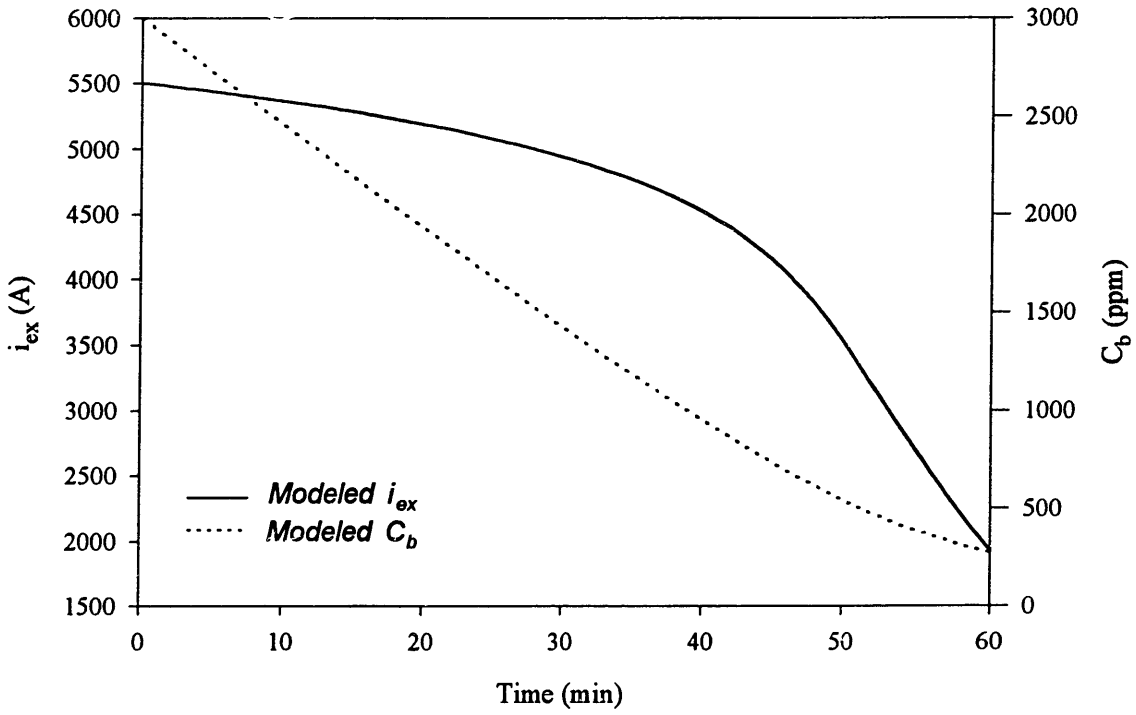


Figure 6-13: Modeled external current and oxygen concentration variation for an anode-supported deoxidation cell.

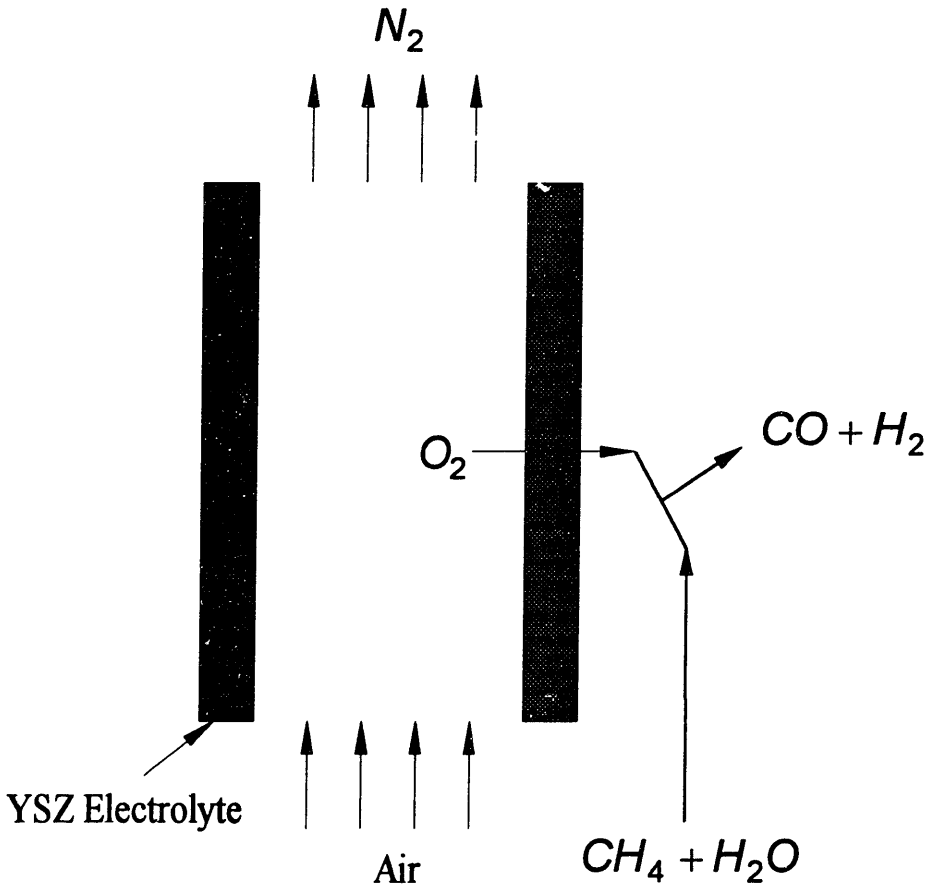


Figure 6-14: Synthesis gas production based on the use of YSZ electrolytes.

Table 2.1: Molten metal deoxidation employing solid oxide electrolytes: experimental parameters and results.

| *Ref.* | *Crucible Material/ Furnace* | *Electrolyte* | *Melt Temp. (°C) Atms.* | *Cathode* | *Anode* | *Method/ Maximum Applied EMF (V)* | *Current Density ($mA/cm^2$)* | *Deoxidation Kinetics (ppm)/ Stirring* | *Process Mechanism* |
|---|---|---|---|---|---|---|---|---|---|
| [13] | MgO Stabilized $ZrO_2$ | Crucible | Cu<br>1150<br>$N_2$ | Mo Rod in Cu Melt Outside Crucible | Mo Rod in Cu Melt Inside Crucible | Electrolytic/ 3.22 | NA | 70 to 10<br>25 mins./<br>NA | Not Described |
| [4] | Alumina/ C Resistance | Stabilized $ZrO_2$ Tube | Fe, Co, Ni, Cu<br>1600<br>Argon | Metal Wire In Bath Outside Tube | Pt-Rh/Gas or Cu (l)/Graphite Inside Tube | Electrolytic/ 7.5 | 150 | 500 to 20/30<br>100 mins./<br>Mechanical | > 160ppm ET<br>< 160ppm MT |
| [5] | Calcia Stabilized $ZrO_2$/ Balzers VSG Induction | Crucible | Cu<br>1150<br>Argon | Chromel Wire in Melt Inside Crucible | Pt/Air Outside Crucible | Electrolytic/ 3.0 | 93 | 300 to 10<br>8 mins./<br>Induction Stirring<br>($\alpha$ = 0.02) | > 90ppm ET<br>< 45ppm MT |
| [7] | 8 wt% Yttria Stabilized $ZrO_2$/ Balzers VSG Induction | Crucible | Cu<br>1110, 1215<br>Argon | 446 Stainless Rod in Melt Inside Crucible | Pt/Air Outside Crucible | Electrolytic/ ≈ 1 | 80 | 600 to < 10<br>30 mins./<br>Induction Stirring<br>($\alpha$ = 0.003, 0.005) | > 300ppm ET<br>< 100ppm MT |
| [3] | Alumina/ SiC Resistance | Calcia Stabilized $ZrO_2$ Tube | Fe<br>1550<br>Argon | Melt | $CO/CO_2$ Gas | Semi-Permeability/ NA | NA | 580 to 300<br>200 mins./<br>Ar Bubbling<br>($\alpha$ = 0.00015) | MT |
| [1] | Alumina/ Induction | 8 wt% YSZ Tube | Low C Steel<br>1600<br>Argon | Mo Wire in Melt Outside Crucible | Mo Wire – Mo/YSZ Cermet Inside Tube/ $H_2$ Atms. | Galvanic/ NA | 5 | 700 to 100<br>500 mins./<br>Stirring with Graphite Susceptor<br>($\alpha$ = 0.004 to 0.015) | > 300ppm ET<br>< 200ppm MT |
| [8] | Alumina or Quartz/ SiC Resistance and Induction | YSZ Tube | Cu<br>1200<br>Argon | Chromel Wire in Melt Outside Crucible | Chromel Wire – Ni/YSZ Cermet Inside Tube/ $H_2$ or $95N_2 - 5H_2$ Atms. | Galvanic/ NA | 11 | 85 to < 5<br>85 mins./<br>Ar Bubbling<br>($\alpha$ = 0.005 to 0.012)<br>Induction Stirring<br>($\alpha$ = 0.06 to 0.09) | > 30ppm ET<br>< 20ppm MT |

MT: Mass transfer in the melt
ET: Transfer of oxygen ions in the electrolyte
NA: Not Applicable

Table 3.1: EPMA analysis of the electrolyte.

| *Electrolyte Composition (ZDY-4)* | |
|---|---|
| **Oxide** | **Wt. %** |
| $Y_2O_3$ | 7.9011 |
| $ZrO_2$ | 89.6282 |
| $Al_2O_3$<br>MgO<br>$SiO_2$ | 2 |

Table 3.2: Values of activation energy $E_i$ and pre-exponential constant $C_i$.

| *Temperature Range (°C)* | *$E_i$ (eV)* | *$C_i$ (S/cm)* |
|---|---|---|
| 1200 – 1440°C | 1.066 | $1.268 \times 10^6$ |
| 1440 – 1650°C | 0.803 | $2.246 \times 10^5$ |

Table 4.1: Modeling parameters (expt. PRE).

| | | |
|---|---|---|
| *Experimental Parameters* | $m_{melt}$ (g) | 3925 |
| | $P_{H_2}$ (atm) | $\approx 1$ |
| | v (l/min) | 2.5 |
| | Melt Temperature (°C) | 1200 |
| | Submersion (inches) | 4.349 |
| | Melt/Electrolyte Interfacial Area ($cm^2$) | 45.11 |
| | YSZ Tube OD (cm) | 1.3 |
| | YSZ Tube ID (cm) | 1.04 |
| | $\rho_{melt}$ (g/cc) | 7.98 |
| | $R_{ex}$ (mΩ) | 8 |
| | $E_{OC}$ before Short Circuit (V) | 0.64 |
| | $C_0$ (ppm) | 443 |
| | $\sigma_\theta^0$ (S – $atm^{1/4}$/cm) | $2.87 \times 10^{-8}$ |
| | $\sigma_{ion}$ (S/cm) {$r_{ion}$ (mΩ)} | 0.196 {16} |
| *Literature Data* | $M_O$ (g/mol) | 16 |
| | F (coul/equiv.) | 96485 |
| | Gas Constant (atm-l/mol-K) | 0.082 |
| | Gas Constant (J/mol-K) | 8.314 |
| | $K_s$ (wt% - $atm^{-1/2}$) | 111.32 (at 1200°C) |
| | $K_p$ ($atm^{-1/2}$) | 791055.7 (at 1200°C) |
| *Calculated Parameters* | $P^r_{O_2}$ (OC) (atm) | $3 \times 10^{-16}$ |
| | $P^r_{H_2O}$ (OC) (atm) | 0.0137 |
| | α (cm/s) | 0.00388 |
| | $k_1$ (ppm) | 0.0193 |
| | $k_2$ (ppm/A) | 0.0041 |
| | $r_{con}$ (Ω) | 0.32 |

Table 5.1: Modeling/experimental parameters for experiment 1.

| | | |
|---|---|---|
| *Experimental Parameters* | $m_{melt}$ (g) | 720 |
| | $P_{H_2}$ (atm) | $\approx 1$ |
| | v (l/min) | 2.5 |
| | Melt Temperature (°C) | 1200 |
| | Submersion (inches) | 1.51 |
| | Melt/Electrolyte Interfacial Area ($cm^2$) | 16.02 |
| | YSZ Tube OD (cm) | 1.3 |
| | YSZ Tube ID (cm) | 1.04 |
| | $\rho_{melt}$ (g/cc) | 7.98 |
| | $R_{ex}$ (mΩ) | 13 |
| | $E_{OC}$ before Short Circuit (V) | 0.84 |
| | $C_0$ (ppm) | 3000 |
| | $\sigma_e^0$ (S – $atm^{1/4}$/cm) | $2.87 \times 10^{-8}$ |
| | $\sigma_{ion}$ (S/cm) {$r_{ion}$ (mΩ)} | 0.196 {47} |
| *Literature Data* | $M_O$ (g/mol) | 16 |
| | F (coul/equiv.) | 96485 |
| | Gas Constant (atm-l/mol-K) | 0.082 |
| | Gas Constant (J/mol-K) | 8.314 |
| | $K_s$ (wt% - $atm^{-1/2}$) | 111.32 (at 1200°C) |
| | $K_p$ ($atm^{-1/2}$) | 791055.7 (at 1200°C) |
| *Calculated Parameters* | $P^r_{O_2}$ (OC) (atm) | $2.3 \times 10^{-17}$ |
| | $P^r_{H_2O}$ (OC) (atm) | 0.0038 |
| | α (cm/s) | 0.007 |
| | $k_1$ (ppm) | 0.00535 |
| | $k_2$ (ppm/A) | 0.0041 |
| | $r_{con}$ (Ω) | 0.08 |

Table 5.2: Modeling/experimental parameters for experiment 2.

| | | |
|---|---|---|
| *Experimental Parameters* | $m_{melt}$ (g) | 731 |
| | $P_{H_2}$ (atm) | $\approx 1$ |
| | v (l/min) | 2.5 |
| | Melt Temperature (°C) | 1200 |
| | Submersion (inches) | 1.69 |
| | Melt/Electrolyte Interfacial Area ($cm^2$) | 17.9 |
| | YSZ Tube OD (inch) | 1.3 |
| | YSZ Tube ID (inch) | 1.04 |
| | $\rho_{melt}$ (g/cc) | 7.98 |
| | $R_{ex}$ (mΩ) | 13 |
| | $E_{OC}$ before Short Circuit (V) | 0.9 |
| | $C_0$ (ppm) | 709.5 |
| | $\sigma_\theta^0$ (S – $atm^{1/4}$/cm) | $2.87 \times 10^{-8}$ |
| | $\sigma_{ion}$ (S/cm) {$r_{ion}$ (mΩ)} | 0.196 {42} |
| *Literature Data* | $M_O$ (g/mol) | 16 |
| | F (coul/equiv.) | 96485 |
| | Gas Constant (atm-l/mol-K) | 0.082 |
| | Gas Constant (J/mol-K) | 8.314 |
| | $K_s$ (wt% - $atm^{-1/2}$) | 111.32 (at 1200°C) |
| | $K_p$ ($atm^{-1/2}$) | 791055.7 (at 1200°C) |
| *Calculated Parameters* | $P_{O_2}^r$ (OC) (atm) | $1.95 \times 10^{-19}$ |
| | $P_{H_2O}^r$ (OC) (atm) | 0.00035 |
| | α (cm/s) | 0.01 |
| | $k_1$ (ppm) | 0.00049 |
| | $k_2$ (ppm/A) | 0.0041 |
| | $r_{con}$ (Ω) | 0.1 |

Table 6.1: Experimental parameters for the longevity/cycling experiments.

| *Cycling Experiment* | *No. of Cycles* | *Time Immersed in Copper (hrs)* | *Time held in Top Zone (hrs)* | *Gas Flow Rates (ml/min)* |
|---|---|---|---|---|
| Expt. CE1 | 2 | 4 | 28.3 | Argon: 39<br>Forming Gas: 331 |
| Expt. CE2 | 10 | 20 | 80.5 | |

Table 6.2: Specific surface areas of Ni-YSZ cermets.

| *Ni-YSZ Cermet* | *Specific Surface Area ($cm^2/g$)* |
|---|---|
| As Prepared | 288 |
| After Expt. CE1 | 176 |
| After Expt. CE2 | 107 |

Table 6.3: Modeling parameters for batch deoxidation.

| | | |
|---|---|---|
| *Experimental Parameters* | $M_{melt}$ (t) | 50 (100 Tubes) |
| | $P_{H_2}$ (atm) | $\approx 1$ |
| | v (l/min) | 550 |
| | Melt Temperature (°C) | 1200 |
| | Submersion (inches) | 60 |
| | Melt/Electrolyte Interfacial Area ($cm^2$) | 7296 |
| | YSZ Tube OD (inch) | 3 |
| | YSZ Tube ID (inch) | 2.99 |
| | $\rho_{melt}$ (g/cc) | 7.98 |
| | $R_{ex}$ (mΩ) | $10^{-4}$ |
| | $E_{OC}$ before Short Circuit (V) | NA |
| | $C_0$ (ppm) | 3000 |
| | $\sigma_e^0$ (S – $atm^{1/4}$/cm) | $2.87 \times 10^{-8}$ |
| | $\sigma_{ion}$ (S/cm) {$r_{ion}$ (mΩ)} | 0.196 {0.018} |
| *Literature Data* | $M_O$ (g/mol) | 16 |
| | F (coul/equiv.) | 96485 |
| | Gas Constant (atm-l/mol-K) | 0.082 |
| | Gas Constant (J/mol-K) | 8.314 |
| | $K_s$ (wt% - $atm^{-1/2}$) | 111.32 (at 1200°C) |
| | $K_p$ ($atm^{-1/2}$) | 791055.7 (at 1200°C) |
| *Calculated Parameters* | $P^r_{O_2}$ (OC) (atm) | $1.95 \times 10^{-19}$ |
| | $P^r_{H_2O}$ (OC) (atm) | 0.00035 |
| | α (cm/s) | 0.01 |
| | $k_1$ (ppm) | 0.00049 |
| | $k_2$ (ppm/A) | $1.93 \times 10^{-5}$ |
| | $r_{con}$ (Ω) | $8.7 \times 10^{-5}$ |

# Bibliography


[1] Z. Hasham, U.B. Pal, and K.C. Chou. Deoxidation of molten steel using a short-circuited solid-oxide electrochemical cell. *Journal of the Electrochemical Society*, **142** (2):469–75, 1995.

[2] K. Kiukkola and C. Wagner. Measurements on galvanic cells involving solid electrolytes. *Journal of the Electrochemical Society*, **104** :379–86, 1957.

[3] M. Iwase, M. Tanida, A. Mclean, and T. Mori. Electronically driven transport of oxygen from liquid iron to $CO+CO_2$ gas mixtures. *Metallurgical Transactions*, **12** :517–24, 1981.

[4] W.A. Fischer and D. Janke. Electrolytic deoxidation of liquid metals at 1600°C. *Scripta Metallurgica*, **6** :923–28, 1972.

[5] K.E. Oberg, L.M. Friedman, W.M. Boorstein, and R.A. Rapp. Electrochemical deoxidation of induction-stirred copper melts. *Metallurgical Transactions*, **4** (1):75–82, 1973.

[6] R.R. Odle and R.A. Rapp. Electrochemical studies and processes involving oxygen in liquid metals. In Z.A. Foroulis and W.W. Smeltzer, editors, *Electrochemical Society Symposium Proceedings on Metal-Slag-Gas Reactions and Processes*, pages 851–74. The Electrochemical Society Inc., 1975.

[7] R.R. Odle and R.A. Rapp. Further study of the electrochemical deoxidation of induction-stirred copper melts. *Metallurgical Transactions B*, **8** (12):581–89, 1977.

[8] S. Yuan, U.B. Pal, and K.C. Chou. Modeling and scale-up of galvanic deoxidation of molten metals using solid electrolyte cells. *Journal of the American Ceramic Society*, **79** (3):641–50, 1996.

[9] S. Yuan. *Fabrication, Performance and Process Optimization of Solid Electrolyte Cells for Electrochemical Refining of Copper.* PhD dissertation, Massachusetts Institute of Technology, Department of Materials Science and Engineering, 1995.

[10] D.R. Gaskell. *Introduction to Metallurgical Thermodynamics.* Hemisphere Publishing Corporation, New York, $2^{nd}$ edition, 1981.

[11] N.Q. Minh. Ceramic fuel cells. *Journal of the American Ceramic Society*, **76** (3):563–88, 1993.

[12] K.C. Chou, S. Yuan, and U.B. Pal. Deposition, electrical property and direct porosity measurement of Ni-$ZrO_2$ cermet electrodes. In S.C. Singhal and H. Iwahara, editors, *Proceedings of the Third International Symposium on Solid Oxide Fuel Cells*, Electrochemical Society Proceedings, pages 431–43. The Electrochemical Society Inc., Pennington, N.J., 1993.

[13] B. Korousic and B. Marincek. Elektrolytische desoxydation von kupferschmelzen. *Helvetica Chimica Acta*, **51** :907–11, 1968.

[14] T.H. Etsell. Unpublished research.

[15] M. Iwase. Unpublished research.

[16] N.Q. Minh and T. Takahashi. *Science and Technology of Ceramic Fuel Cells.* Elsevier Science B.V., Amsterdam, 1995.

[17] S.P. Jiang. The role of water vapor on the kinetics of $H_2$ oxidation on porous Ni electrodes at 1000°C. In S.P.S. Badwal, M.J. Bannister, and R.H.J. Hannink, editors, *Science and Technology of Zirconia V*, pages 819–28. Technomic Pub. Co., Lancaster, PA, 1993.

[18] J. Mizusaki, H. Tagawa, T. Saito, K. Kamitani, T. Yamamura, K. Hirano, S. Ethara, T. Takagi, T. Hikita, M. Ippommatsu, S. Nakagawa, and K. Hashimoto. Preparation of nickel pattern electrodes on YSZ and their electrochemical properties in $H_2$-$H_2O$ atmospheres. *Journal of the Electrochemical Society*, **141** (8):2129–34, 1994.

[19] J. Mizusaki, H. Tagawa, T. Saito, T. Yamamura, K. Kamitani, K. Hirano, S. Ethara, T. Takagi, T. Hikita, M. Ippommatsu, S. Nakagawa, and K. Hashimoto. Kinetic studies of the reaction at the nickel pattern electrode on YSZ in $H_2$-$H_2O$ atmospheres. *Solid State Ionics*, **70/71** :52–58, 1994.

[20] N.J. Maskalick. Design and performance of tubular solid oxide fuel cells. In S.C. Singhal, editor, *Proceedings of the First International Symposium on Solid Oxide Fuel Cells*, Electrochemical Society Proceedings PV 89-11, pages 279–87. The Electrochemical Society Inc., Pennington, N.J., 1989.

[21] D.R. Poirier and G.H. Geiger. *Transport Phenomena in Materials Processing.* The Minerals, Metals and Materials Society, Warrendale, PA, 1994.

[22] K.E. Oberg, L.M. Friedman, W.M. Boorstein, and R.A. Rapp. The diffusivity and solubility of oxygen in liquid copper and liquid silver from electrochemical measurements. *Metallurgical Transactions*, **4** (1):61–67, 1973.

[23] O. Kubaschewski, C.B. Alcock, and P.J. Spencer. *Materials Thermochemistry.* Pergamon Press, New York, $6^{th}$ edition, 1993.

[24] E.C. Subbarao and H.S. Maiti. Solid electrolytes with oxygen-ion conduction. *Solid State Ionics*, **11** :317–38, 1984.

[25] S.P.S. Badwal. Zirconia-based solid electrolytes: Microstructure, stability and ionic conductivity. *Solid State Ionics*, **52** :23–32, 1992.

[26] D.J. Green, R.H.J. Hannink, and M.V. Swain. *Transformation Toughening of Ceramics*, chapter 1, pages 1–15. CRC Press Inc., Boca Raton, Florida, 1989.

[27] F. Sanchez-Bajo, F.L. Cumbrera, F. Guiberteau, and A. Dominguez-Rodriguez. Microstructural characterization of Y-PSZ (4 mol%) polycrystals by means of X-Ray diffraction experiments. *Materials Letters*, **15** :39–44, 1992.

[28] H.L. Tuller and A.S. Nowick. Doped ceria as a solid-oxide electrolyte. *Journal of the Electrochemical Society*, **122** (2):255–59, 1975.

[29] P.H. Scaife, D.A.J. Swinkels, and S.R. Richards. Characterization of zirconia electrolytes for oxygen probes used in steel making. *High Temperature Science*, **8** :31–47, 1976.

[30] D.W. Strickler and W.G. Carlson. Ionic conductivity of cubic solid solutions in the system CaO-$Y_2O_3$-$ZrO_2$. *Journal of the American Ceramic Society*, **47** (3):122–27, 1964.

[31] M. Kleitz, E. Fernandez, J. Fouletier, and P. Fabry. Determination of electronic conductivities and ionic domains of $ZrO_2$-$Y_2O_3$ by semipermeability measurements. In A.H. Heuer and L.W. Hobbs, editors, *Advances in Ceramics - Science and Technology of Zirconia 3*, pages 349–63. The American Ceramic Society Inc., Columbus, OH, 1981.

[32] H. Schmalzried. Ionen-und elektronenleitung in binären oxiden und ihre untersuchung mittels emk-messungen. *Zeitschrift für Physikalische Chemie Neue Folge*, **38** :87–102, 1963.

[33] D.A.J. Swinkels. Rapid determination of electronic conductivity limits of solid elctrolytes. *Journal of the Electrochemical Society*, **117** :1267–68, 1970.

[34] M. Iwase, E. Ichise, M. Takeuchi, and T. Yamasaki. Measurements of the parameter $P_\theta$, for the determinations of mixed ionic and n-type electronic conduction in commercial zirconia electrolytes. *Transactions of the Japan Institute of Metals*, **25** (1):43–52, 1984.

[35] K. Kinoshita, F.R. McLarnon, and E.J. Cairns. Fuel cells a handbook. Technical report, Lawrence Berkely Laboratory, Berkeley, California, May 1988.

[36] S.C. Britten. Solid state amperemetric sensor for in-situ monitoring of slag compositions for high temperature metallurgical processes. Technical report, Massachusetts Institute of Technology, December 1995. Ph.D. Thesis Proposal.

[37] M. Iwase and T. Mori. Problems in oxygen sensors for steelmaking. *Transactions of the Iron and Steel Institute of Japan*, **19** :126–32, 1979.

[38] J.W. Patterson. Conduction domains for solid electrolytes. *Journal of the Electrochemical Society*, **118** :1033, 1971.

[39] T.H. Etsell and S.N. Flengas. n-type conductivity in stabilized zirconia solid electrolytes. *Journal of the Electrochemical Society*, **119** :1–7, 1972.

[40] L.M. Friedman, K.E. Oberg, W.M. Boorstein, and R.A. Rapp. Electronic conductivities of commercial $ZrO_2$+ 3 to 4 wt pct CaO electrolytes. *Metallurgical Transactions*, **4** (1):69–74, 1973.

[41] T. Kawada, N. Sakai, H. Yokokawa, and M. Dokiya. Characteristics of slurry-coated nickel-zirconia cermet anodes for solid-oxide fuel cells. *Journal of the Electrochemical Society*, **137** (10):3042–47, 1990.

[42] S. Murakami, Y. Akiyama, N. Ishida, T. Yasuo, T. Saito, and N. Furukawa. Development of a solid-oxide fuel cell with composite anodes. In F. Grosz, P. Zegers, S.C. Singhal, and O. Yamamoto, editors, *Proceedings of the Second International Symposium on Solid Oxide Fuel Cells*, Electrochemical Society Proceedings, pages 561–68. The Electrochemical Society Inc., Pennington, N.J., 1991.

[43] D.W. Dees, T.D. Claar, T.E. Easler, D.C. Fee, and F.C. Mrazek. Conductivity of porous Ni/$ZrO_2$-$Y_2O_3$ cermets. *Journal of the Electrochemical Society*, **134** (9):2141–46, 1987.

[44] T. Setoguchi, K. Okamoto, K. Eguchi, and H. Arai. Effects of anode material and fuel on anodic reaction of solid-oxide fuel cells. *Journal of the Electrochemical Society*, **139** (10):2875–80, 1992.

[45] T. Iwata. Characterization of Ni-YSZ anode degradation for substrate-type solid-oxide fuel cells. *Journal of the Electrochemical Society*, **143** (5):1521–25, 1996.

[46] S. Lowell snd J.E. Shields. *Powder Surface Area and Porosity*. Powder Technology Series. Chapman and Hall Ltd., New York, $2^{nd}$ edition, 1984.

[47] H. Rajainmäki, A. Helenius, and M. Kolehmainen. The production and application of oxygen-free copper. *Journal of Metals*, **45** (3):68–70, 1993.

[48] A. Gubner, H. Landes, J. Metzger, H. Seeg, and R. Stübner. Investigations into the degradation of the cermet anode of a solid oxide fuel cell. In U. Stimming, S.C. Singhal, H. Tagawa, and W. Lehnert, editors, *Proceedings of the Fifth International Symposium on Solid Oxide Fuel Cells*, Electrochemical Society Proceedings PV 97-40, pages 844–50. The Electrochemical Society Inc., Pennington, N.J., 1997.

# Biographical Note

The author was born on February 11, 1974 in Jaipur, India. He graduated from the Indian Institute of Technology, Bombay in July 1995, with the degree of Bachelor of Technology in Metallurgical Engineering. He came to the Massachusetts Institute of Technology as a graduate student in the Department of Materials Science and Engineering in September 1995.

He has authored a publication entitled "Comparison of power densities and chemical-potential variation in solid oxide fuel cells with multilayer and single-layer solid-oxide electrolytes", *Journal of the Electrochemical Society*, **145** (1):99-106, 1998. The author is a member of The Minerals, Metals and Materials Society, ASM International, and The American Ceramic Society.